

**Nanoscale diffusion, compound
formation and phase transitions
in Mo/Si multilayer structures**

Véronique de Rooij-Lohmann

Ph.D. committee

Chairman:

prof. dr. G. van der Steenhoven University of Twente

Secretary:

prof. dr. G. van der Steenhoven University of Twente

Promoter:

prof. dr. F. Bijkerk MESA+ Institute for Nanotechnology,
University of Twente
FOM Institute for Plasma Physics
Rijnhuizen

Assistant promoter:

dr. A.E. Yakshin FOM Institute for Plasma Physics
Rijnhuizen

Referee:

prof. dr. H.H. Brongersma Eindhoven University of Technology
Imperial College (London)

Members:

prof. dr. K.J. Boller MESA+ Institute for Nanotechnology,
University of Twente
prof. dr. ir. B. Poelsema MESA+ Institute for Nanotechnology,
University of Twente
prof. dr. P.C. Zalm University of Salford
Philips Research
prof. dr. ir. M.C.M. van de Sanden Eindhoven University of Technology

Cover: the traditional Indonesian delicacy *lapis legit* (thousand layer cake) consists of many alternating layers. This creates an optical contrast similar to that of Mo/Si multilayer mirrors, albeit at a one million times larger length-scale.

Nanoscale diffusion, compound formation and phase transitions in Mo/Si multilayer structures

Véronique de Rooij-Lohmann

Thesis, University of Twente, Enschede – illustrated

With references – With summary in English and Dutch

ISBN: 978-90-5335-314-1

Printed by Ridderprint B.V. (2010)

NANOSCALE DIFFUSION, COMPOUND
FORMATION AND PHASE TRANSITIONS
IN Mo/Si MULTILAYER STRUCTURES

PROEFSCHRIFT

ter verkrijging van de graad van doctor
aan de Universiteit Twente, op gezag van
de rector magnificus, prof. dr. H. Brinksma,
volgens besluit van het College voor Promoties
in het openbaar te verdedigen op
vrijdag 1 oktober 2010 om 16:45 uur

door

Véronique Irene Theresia Agnes de Rooij-Lohmann

geboren op 28 juli 1982

te Beuningen

Dit proefschrift is goedgekeurd door de promotor

Prof. dr. F. Bijkerk

en de co-promotor

dr. A.E. Yakshin

*“Das schönste Erlebnis ist die Begegnung mit dem Geheimnisvollen.
Sie ist der Ursprung jeder wahren Kunst und Wissenschaft.”*
- Albert Einstein (1879-1955)

This thesis is based on the following publications:

Chapter 3: V.I.T.A. de Rooij-Lohmann, A.W. Kleyn, F. Bijkerk, H.H. Brongersma, and A.E. Yakshin, “*Diffusion and interaction studied nondestructively and in real-time with depth-resolved low energy ion spectroscopy*”, Applied Physics Letters **94**, p. 63107 (2009).

Chapter 4: V.I.T.A. de Rooij-Lohmann, A.E. Yakshin, R.W.E. van de Kruijs, E. Zoethout, A.W. Kleyn, E.G.Keim, M. Gorgoi, F. Schäfers, H.H. Brongersma, and F. Bijkerk, “*Enhanced diffusion across interlayer upon amorphous-to-nanocrystalline phase transition*”, Journal of Applied Physics **108**, p. 014314 (2010).

Chapter 5: V.I.T.A. de Rooij-Lohmann, L.W. Veldhuizen, E. Zoethout, A.E. Yakshin, R.W.E. van de Kruijs, B.J. Thijsse, M. Gorgoi, F. Schäfers, and F. Bijkerk, “*Chemical interaction of B₄C diffusion barrier layer with Mo/Si layered structures*”, submitted.

Chapter 6: V.I.T.A. de Rooij-Lohmann, A.E. Yakshin, E. Zoethout, J. Verhoeven, and F. Bijkerk, “*Reduction of interlayer thickness by low-temperature deposition of Mo/Si multilayer mirrors for X-ray reflection*”, submitted.

Chapter 7: V.I.T.A. de Rooij-Lohmann, I.V. Kozhevnikov, L. Peverini, E. Ziegler, R. Cuerno, F. Bijkerk, and A.E. Yakshin, “*Roughness evolution of Si surfaces upon Ar ion erosion*”, Applied Surface Science **256**, p. 5011 (2010).



This work is part of the FOM Industrial Partnership Programme I10 ('XMO') which is carried out under contract with Carl Zeiss SMT AG, Oberkochen and the 'Stichting voor Fundamenteel



Onderzoek der Materie (FOM)', the latter being financially supported by the 'Nederlandse Organisatie voor Wetenschappelijk Onderzoek (NWO)'.

Table of Contents

1. Introduction.....	11
1.1. Multilayer reflective optics	11
1.2. Applications of multilayer optics	13
1.3. Diffusion in Mo/Si multilayer structures	16
1.4. Roughness of multilayer mirrors.....	18
1.5. Manufacturing of multilayer optics.....	19
1.5.1. Deposition techniques.....	19
1.5.2. Ion bombardment.....	20
1.5.3. Substrate temperature	23
1.6. This thesis	25
2. Experimental.....	27
2.1. Sample fabrication	27
2.1.1. Layer thickness control.....	27
2.2. Analysis techniques.....	29
2.2.1. X-ray reflectance and scattering	29
2.2.2. (Hard) X-ray photoelectron spectroscopy.....	32
2.2.3. Low Energy Ion Scattering spectroscopy	34
2.2.4. Transmission Electron Microscopy	36
3. Diffusion and interaction studied non-destructively and in real-time with depth-resolved Low Energy Ion Scattering spectroscopy	37
3.1. Abstract	37
3.2. Introduction.....	37
3.3. Experimental details.....	39
3.4. Results.....	40
3.5. Conclusions.....	44
3.6. Acknowledgments.....	44
4. Enhanced diffusion upon amorphous-to-nanocrystalline phase transition in Mo/B₄C/Si layered systems	45
4.1. Abstract	45
4.2. Introduction.....	45
4.3. Diffusion rate	46
4.3.1. Experimental details	46
4.3.2. Results	47
4.4. Chemistry	49
4.4.1. Experimental details	49
4.4.2. Results	50
4.5. Morphology.....	53
4.5.1. Experimental details	53
4.5.2. Results	53

4.6.	Conclusions	55
4.7.	Acknowledgments	55
5.	Chemical interaction of B₄C with Mo/Si layered structures	56
5.1.	Abstract	56
5.2.	Introduction	56
5.3.	Experimental Details	57
5.4.	Results	59
5.4.1.	Mo/B/Si.....	59
5.4.2.	Mo/C/Si.....	62
5.4.3.	Mo/B ₄ C/Si.....	65
5.5.	Discussion	68
5.6.	Conclusions	69
5.7.	Acknowledgments	70
6.	Reduction of interlayer thickness by low-temperature deposition of Mo/Si multilayer mirrors for X-ray reflection.....	71
6.1.	Abstract	71
6.2.	Introduction	71
6.3.	Experimental details	72
6.4.	Results	73
6.4.1.	GIXR and annealing data.....	73
6.4.2.	XPS	76
6.4.3.	WAXRD	77
6.5.	Discussion	78
6.6.	Conclusion.....	80
6.7.	Acknowledgments	80
7.	Roughness evolution of Si surfaces upon Ar ion erosion	81
7.1.	Abstract	81
7.2.	Introduction	81
7.3.	Experimental details	83
7.4.	Results and discussion.....	85
7.5.	Conclusions and outlook	89
7.6.	Acknowledgments	90
8.	Valorisation and Outlook	91
8.1.	Progress in Lithography, Progress for Society	91
8.2.	LEIS	92
8.3.	Mo, Si and B ₄ C – Physics and Chemistry	93
8.4.	Cryogenic deposition.....	94
8.5.	Roughness evolution	95
	Summary	97
	Samenvatting.....	99
	Acknowledgments.....	101

Curriculum Vitae103
Bibliography104

1. Introduction

1.1. Multilayer reflective optics

The use of light, in all its fascinating facets, requires optical elements. Collecting light, focusing it to small spots, spectral analysis, and imaging objects in magnifying or demagnifying schemes, are all frequently exploited examples of the use of optics. For an optical system for light from the infrared to the ultraviolet, the designer has the freedom to choose between reflecting optics (mirrors) or refracting optics (lenses). Although high quality optics require careful design and manufacturing, both lenses and mirrors are in itself very simple devices. Below 100 nm, however, the designer finds himself in the so-called extreme ultraviolet (EUV) range, where all materials are highly absorbing and lenses are not an option. At the same time, the deviation δ of the real part of the refractive index from unity is very small. As a consequence, any optical contrast between different materials is very small. Hence, the reflectance of a single surface is never more than a few percent, unless the grazing angle of incidence θ is close to or below the critical angle θ_C . The critical angle is given by Equation (1.1):

$$\sin \theta_C \approx \sqrt{2\delta}. \quad (1.1)$$

Obviously, θ_C is very close to 0° , which is often impractical or even impossible to use. Moreover, such grazing angles of incidence lead to an extremely small numerical aperture (NA), which reduces the transmission of the optical system and worsens the resolution R ($R \propto 1/NA$). It is only below 0.3 nm, in the hard x-ray region, that the cross-section for interaction of photons with matter has decreased to such a small value that sufficiently transparent materials are available again. A high reflectance for hard x-rays can furthermore be attained using a crystal whose planes constitute a practically perfect Bragg reflector.

The solution for creating high-reflectance optics for non-grazing incidence in the EUV range was inspired by the Bragg reflection of crystals, and is illustrated in Figure 1.1: the optics can be given a fairly high reflectance by mimicking the periodic structure of crystals with an artificial, periodic

multilayer structure. In its most simple form, such a multilayer mirror consists of alternating layers of two materials with maximum optical contrast and minimum absorption to achieve maximum reflectance. The period thickness Λ of such a multilayer mirror should be chosen such that the Bragg condition, given by Formula (1.2)

$$m\lambda = 2\Lambda \sin \theta \sqrt{1 - \frac{8\bar{\delta}\Lambda^2}{m^2\lambda^2}}, \quad (1.2)$$

is fulfilled [1], with m the order of the Bragg maximum, λ the wavelength, θ the grazing angle of incidence, and $\bar{\delta}$ the weighted average of δ over one period[†].

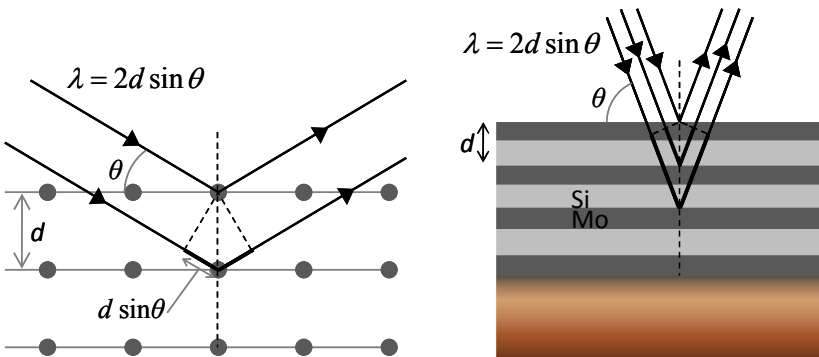


Figure 1.1. Bragg reflection in a crystal (left) and in a multilayer structure (right).

The choice of the materials depends on the wavelength of the radiation for which the mirror is designed. For a two-material system and $12.5 \text{ nm} < \lambda < 25 \text{ nm}$, Mo/Si is one of the best choices and the most widely used [2]. Si acts as a spacer since this wavelength range is just above the absorption edge of Si at 12.5 nm, and, consequently, δ and the absorption coefficient β are small ($5.4 \cdot 10^{-4}$ and $1.8 \cdot 10^{-3}$ at $\lambda = 13.5 \text{ nm}$, respectively). The reflector Mo also has a rather low value of β ($6.4 \cdot 10^{-3}$ at $\lambda = 13.5 \text{ nm}$), but combines this with a relatively high value of δ ($7.8 \cdot 10^{-2}$

[†] Equation (1.2) is an approximation that is valid only if $\delta \ll 1$ and the absorption coefficient $\beta \ll \delta$.

at $\lambda = 13.5$ nm), thus providing high contrast and minimum absorption. A transmission electron microscopy image of a Mo/Si multilayer mirror is shown in Figure 1.2. This dissertation focuses on Mo/Si-based systems because of their importance for EUV lithography. The word ‘based’ in ‘Mo/Si-based’ signifies that additional layers, e.g., B_4C , Mo_2C , or SiN_x , can be added to reduce interdiffusion and improve the thermal stability [3, 4]. Other frequently encountered material combinations for soft x-ray optics are for instance La/ B_4C ($6.7 \text{ nm} < \lambda < 13 \text{ nm}$), W/C or W/ B_4C ($0.1 \text{ nm} < \lambda < 1.5 \text{ nm}$), and Fe/C, Co/C, or Ni/C ($4.4 \text{ nm} < \lambda < 7.0 \text{ nm}$) [5-7].

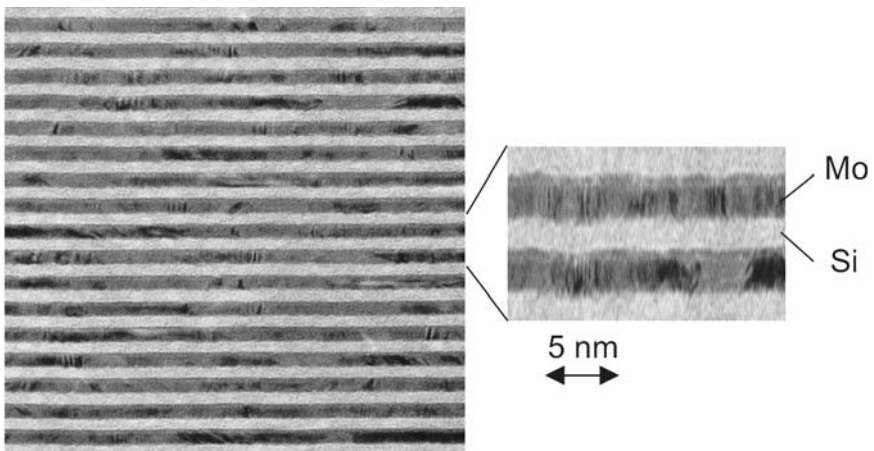


Figure 1.2. Cross-sectional transmission electron microscopy image of a Mo/Si multilayer mirror for EUV reflection.

1.2. Applications of multilayer optics

A prominent advantage of artificial multilayers is that they can be deposited onto curved substrates in order to obtain focusing or defocusing elements, making them of large interest for optical applications. Especially the development of coatings for EUV optics is an active and intensive research field, as EUV optics is regarded as one of the most important new fields in optics [8, 9]. The use of EUV allows new and smaller details to be observed in life sciences and materials science, smaller structures to be manufactured in the lithographic industry, and new details to be observed in astronomy. Hence, multilayer mirrors find application in many fields of science and

technology, e.g., in lithography tools, synchrotron beam-lines, in telescopes, spectroscopy, plasma diagnostics, and soft x-ray laser research. Since it is beyond the scope of this chapter to describe each of those applications in detail, only three selected applications will be briefly addressed here to illustrate the versatility and relevance of multilayer optics.

Another important application of multilayer mirrors is in EUV photoelectron microscopy. In such an instrument, multilayer mirrors are employed to form a Schwarzschild objective that focuses EUV light to a spot of 100 nm on the sample [7]. Analysis of the thus generated photoelectrons reveals information about the elemental composition and the chemical bonds in the sample surface. The EUV spot can be rastered over the sample to obtain a map of the surface composition with a high spatial as well as a high spectral resolution; information that is extremely useful for e.g., the characterization of semiconductor electronics and magnetic recording devices. Life sciences also benefit tremendously from EUV microscopy, as it includes the so-called water window ($\lambda = 2.3\text{-}4.3$ nm), where water has a relatively low absorption coefficient and is nearly an order of magnitude more transparent than organic structures. This results in a high contrast between water and organic structures, and allows studying samples of several μm thick [10]. The high resolution combined with the chemical sensitivity allows studying proteins, ribosomes and DNA.

Multilayer optics are also very useful to obtain high quality EUV pictures of celestial bodies. The period of the multilayer can be tuned to match a specific emission line, or a broadband mirror can be designed to select a wider spectral range. Mo/Si multilayer mirrors are, for instance, used in the Solar-B/EIS instrument, which contains a parabolic focusing mirror and a toroidal grating. Both elements are coated with a broad-band multilayer and divided into two halves, where one half is tuned for $\lambda = 18 - 21$ nm, and the other half for $\lambda = 25 - 29$ nm. These two bands include a number of bright lines from He II, O V, Si VII, Si X, Ca XVII, and Fe X through Fe XXIV. Figure 1.3 displays images of the sun at different spectral lines as an illustration. The spectrometer is designed to provide a spectral resolution of $\lambda/\Delta\lambda \approx 10^4$ – high enough to allow determination of velocities from Doppler shifts with an accuracy of 3 km/s [11].

A particularly demanding application is extreme ultraviolet lithography (EUVL) at $\lambda = 13.5$ nm. EUVL was chosen out of several alternatives [12, 13] as the successor of Deep Ultraviolet lithography at 193 nm, in order to

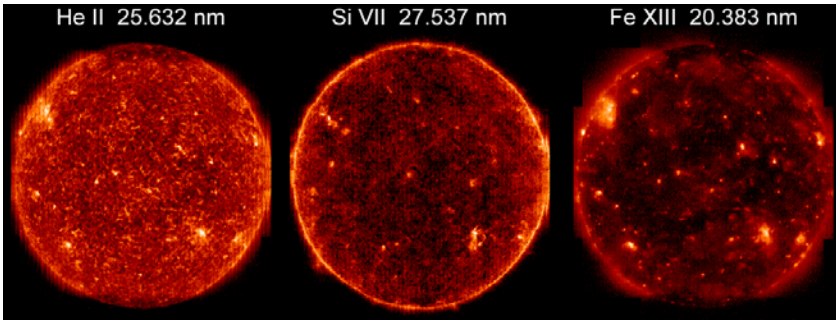


Figure 1.3. Solar-B/EIS image of the sun at different spectral lines, taken on June 27, 2009 [14].

continue shrinking the dimensions of semiconductor structures. One of the major challenges for this application is the lifetime of the mirrors. Debris from the light source and hydrocarbons from the photoresist contaminate the surface, which results in a decreased reflectance. The reflectance can be largely recovered by certain cleaning procedures, but the associated downtime of the lithography tool makes that a costly affair. Moreover, cleaning procedures can have negative side-effects, viz. sputter removal or oxidation of the top layer, or enhanced interdiffusion (see Section 1.3) if e.g. cleaning goes along with a large heat load.

Secondly, EUVL imposes high demands on the reflectance of the mirrors, because, as shown in Figure 1.4, typically as many as ten mirrors and one reflective mask are needed for aberration-free demagnification and projection of the pattern on a mask onto the chip in the making. The EUV radiation power that arrives at the substrate after eleven reflections (ten mirrors and one mask) determines to a large extent the throughput of a lithography tool. Knowing that, it is easily seen that every possible improvement of the multilayer reflectance is necessary. This is even more true as long as state-of-the-art EUV light sources are not (yet) powerful enough to facilitate a sufficiently high throughput for commercial exploitation of lithography tools. One process known to affect the reflectance of the multilayer mirror negatively is the formation of a molybdenumsilicide interlayer at each Mo/Si interface, discussed in more detail in Section 1.3. An enhanced knowledge concerning the physical and chemical processes that affect the formation of this interlayer can be utilized to reduce the interlayer thickness, thus enabling a higher throughput of the lithography tool. Such knowledge is acquired in

Chapters 4 and 5, while Chapter 6 shows how the interlayer thickness can be reduced by depositing the multilayer onto a deeply cooled substrate. Furthermore, Chapter 3 describes how Low Energy Ion Scattering spectroscopy allows studying the interdiffusion at an atomic scale. This makes it a useful technique to investigate interdiffusion dynamics, perform lifetime studies, and assess the extent of the interlayer formation, thus creating the basis for improving the quality of the multilayer mirrors.

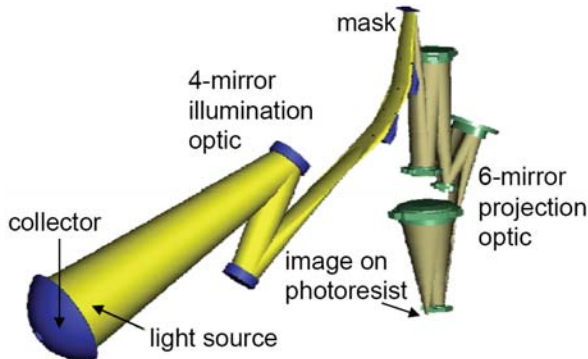


Figure 1.4. Schematic representation of the 10-mirror optics in an EUV lithography tool.

1.3. Diffusion in Mo/Si multilayer structures

About 30% of the light incident on a multilayer mirror is not reflected, but absorbed in the Mo/Si multilayer stack. As a result, at high incident intensity, the mirror heats up and interdiffusion of the layers is enhanced. Interdiffusion obviously reduces the optical contrast and hence the reflectance. Moreover, the formation of a compound generally changes the density, thus inducing either expansion or compaction of the structure. As a consequence, the Bragg condition is no longer perfectly fulfilled for the wavelength for which the mirror was designed. For instance, three compounds can be formed in Mo/Si systems: Mo_3Si , Mo_5Si_3 and MoSi_2 . Depending on which silicide forms, the compaction that is caused by the compound formation varies from 15 to 39 % of the thickness of the silicide interlayer (see Table 1.1).

The detrimental effect of interdiffusion on the reflectance and lifetime of Mo/Si multilayer optics has necessitated research on the interdiffusion. For instance, the compound that forms at the interfaces upon deposition has been

Table 1.1. The structure compaction induced by silicide formation depends on which type of silicide is formed.

	Density (g/cm^3)	Mo consumption ($V_{\text{Mo}} / V_{\text{compound}}$)	Si consumption ($V_{\text{Si}} / V_{\text{compound}}$)	Compaction ($(V_{\text{Mo}} + V_{\text{Si}}) / V_{\text{compound}}$)
Mo	10.2			
Si	2.3			
Mo ₃ Si	9.0	0.80	0.35	0.15
Mo ₅ Si ₃	8.2	0.68	0.53	0.21
MoSi ₂	6.2	0.39	1.00	0.39

identified as (amorphous) MoSi₂ [15, 16]. At annealing temperatures between 350 and 500 °C, all available Si is consumed to form MoSi₂, which crystallizes with a hexagonal lattice ([17, 18]; see also Chapters 3 and 6). Rosen *et al.* [19] reported the interesting discovery that the interlayers are asymmetric: the interlayer at the Mo-on-Si interface is thicker than that at the Si-on-Mo interface. This asymmetry is probably caused by the crystallinity of the Mo layers, as it is only observed for crystalline Mo layers [15, 19, 20]. The growth of a Mo layer is initially amorphous, but the layer crystallizes only upon reaching a certain critical thickness of 2-3 nm [15, 21]. Therefore, interdiffusion can occur at the Mo-on-Si interface while the Mo is still amorphous, whereas crystallization has stabilized the Mo before the Si-on-Mo interface is created by depositing the next Si layer on top of the Mo. The role of the crystallinity was further demonstrated in Ref. [22], where it was found that the interdiffusion rate upon annealing at 300-375 °C is considerably higher for amorphous than for polycrystalline Mo layers.

In order to reduce the interdiffusion and enhance the lifetime of the optics, diffusion barrier layers can be introduced in between the Mo and Si layers. Materials considered so far for diffusion barrier layers include C, Si₃N₄ and B₄C [4, 21, 22]. Especially B₄C interlayers have received much attention, because they do not only improve the stability, but also the reflectance [3, 23]. The influence of B₄C on the diffusion process is investigated in Chapter 4, while the chemical aspects are addressed in Chapter 5.

The period thickness of a multilayer structure can be measured with a very high precision using Grazing Incidence X-ray Reflection (GIXR) analysis

(see Section 2.2.1). As silicide formation reduces the period thickness, measurements of the period thickness provide accurate information about the growth of the interlayer. Therefore, the thermal stability of the mirrors can be assessed by measuring the compaction as a function of annealing time and/or temperature. Measurements of the thermal stability at relatively high temperatures of up to 600 °C are of relevance for the optics that reach the highest temperatures due to thermal load, as well as for accelerated lifetime testing of the optical elements that receive a comparatively small thermal load. Lifetime testing at the temperature at which the mirror is designed to operate is difficult in view of the required long lifetime of several years and the tiny amount of compaction allowed. Therefore, lifetime testing is conducted at a higher temperature to accelerate the interdiffusion, after which the actual lifetime is extrapolated using the Arrhenius law.

1.4. Roughness of multilayer mirrors

Multilayer mirrors thank their high reflectance to the constructive interference of radiation reflected at the many interfaces of the multilayer. As such, it is of paramount importance to avoid layer thickness errors, because they will cause out-of-phase reflection and reduce the reflectance of the mirror. Roughness, being in fact nothing but a local thickness variation, must be kept as low as possible for the same reason, and also because it causes off-specular reflection of light (flare), which compromises the contrast and the resolution. Equation (1.3) [1] illustrates the detrimental effect of roughness:

$$\frac{R(\sigma)}{R_0} = \exp\left(-\frac{4\pi^2\sigma^2}{\Lambda^2}\right) \quad (1.3)$$

$R(\sigma)$ is the reflectance of the first order Bragg peak when the interfaces possess a root-mean-square roughness σ . R_0 is the reflectance of a multilayer structure with perfectly smooth interfaces, and Λ the period of the structure. Equation (1.3) means that in order to limit the reflection losses to 5 %, σ needs to be below 0.036 Λ . In the case of optics for extreme ultraviolet lithography (EUVL) at 13.5 nm, $\Lambda = 6.9$ nm and, hence, the layers should be atomically flat as σ should not exceed 0.25 nm.

Ion bombardment is an indispensable tool to achieve such a challengingly low roughness, as thin films do not form smooth surfaces under all deposition

conditions. Variations in the particle flux (shot noise), geometric shadowing and Volmer-Weber growth (island-like growth) lead to the development of roughness. In multilayer growth, ion bombardment is usually applied during the deposition of every period, either during or after the growth of a layer. Provided that a suitable ion energy, ion element, angle of incidence and ion fluence are used, ion bombardment can very efficiently mediate roughness by sputtering away protruding atoms and by supplying energy to promote surface diffusion. However, an unfortunate choice of parameters leads to intermixing, large stress, and an increased rather than a decreased roughness.

Many products in modern technology, like optical coatings, integrated circuits and especially multilayer mirrors, depend on thin films with smooth surfaces. It is, therefore, little surprising that there is a large interest in models that describe the roughness evolution of a surface upon ion erosion. Numerous models have been proposed since the 1980's, but they are still under heavy debate today. A few of them will be briefly discussed in Chapter 7, which reports on a study of the roughness evolution of Si surfaces under Ar ion bombardment.

1.5. Manufacturing of multilayer optics

1.5.1. Deposition techniques

Multilayer optics are manufactured by alternated deposition of the materials of which the two or more constituent layers are made. Two physical vapor deposition techniques are generally considered in this framework: electron beam (e-beam) evaporation and magnetron sputter deposition. E-beam deposition utilizes, as the name suggests, a beam of electrons to heat the target material sufficiently to evaporate and generate a flux of particles. A layer is grown when the vapor condenses onto the substrate, or any other surface.

Magnetron sputter deposition is an alternative way to produce a flux of particles. A direct current or radio frequency field produces a plasma, usually of Ar, in the vicinity of the target. The target is put at a negative bias in order to attract and accelerate ions. When these fast ions hit the target, they generate a particle flux by sputtering atoms from the target. In contrast with e-beam deposition where the particles have thermal energy (kinetic energy E_K

$\approx 0.1 - 0.2$ eV), in magnetron deposition the particles hit the substrate with $E_K > 5$ eV. This results in less sharp interfaces for magnetron-deposited structures compared to e-beam deposited structures, because the energy supplied by the deposition flux can blur the interface by inducing interdiffusion. Magnetron deposition is, nevertheless, frequently used in industry because the deposition rates can be more stable and it is an easier process to automate. The deposition rate during e-beam evaporation, like any other thermal evaporation method, is sensitive to changes in vapor pressure due to temperature variations.

Thermalized Particle Magnetron (TPM) deposition is a variant of magnetron sputter deposition that allows tuning of E_K . This is achieved by varying the (inert gas) background pressure, so that the changing number of collisions determines to what extent the particles are thermalized. Using this method, a record reflectance of 70.15 % was achieved for a Mo/Si multilayer mirror for EUV reflection [24]. Similar values though have been obtained from the other techniques described in this section.

Ion Beam Assisted Deposition (IBAD), on the other hand, is a special case of e-beam deposition. Like TPM, it has the best of both worlds, namely independent control of deposition flux and energy supply. IBAD is in principle e-beam deposition, but extra energy is provided at request through inert gas ions from an ion gun. This configuration allows independent control of the deposition flux and the ion energy. The ion gun is usually switched off at the beginning of a new layer to avoid unnecessary intermixing. Once the layer thickness exceeds the penetration depth of the ions, the ion gun is switched on to enhance the surface diffusion, thus improving the quality of the layer by densification and smoothening. Alternatively, ion treatment can be implemented as a separate step after the deposition of a layer. Ion beam assistance has been applied either during or after the deposition of all samples used for the research presented in this dissertation.

1.5.2. Ion bombardment

The wide interest for high quality multilayer optics has stimulated extensive research on ion beam smoothening. The first report where ion beam polishing was applied successfully to improve the quality of multilayer optics dates from 1989 [25]. Within a few years, the technique led to impressive results for several multilayer systems, including Ni/C, W/Si and Mo/Si [26-28].

A large number of experiments with ion bombardment during the deposition of Mo/Si multilayer structures have been conducted to determine the set of parameters that gives the best results for this specific system. A vast parameter space of ion energy, type, fluence, and angle of incidence has been explored, as well as where in the deposition process the etching step is best included.

The importance of the choice of the ion type, for instance, was demonstrated by the authors of Ref. [29]. They showed that etching with Kr^+ produces better results than etching with Ar^+ , presumably because the heavier Kr^+ has a smaller penetration depth and, hence, less ion-induced intermixing takes place at the interface. Another way to reduce the penetration depth and avoid intermixing is reduction of the ion *energy*. The ion energy should be high enough, though, to supply sufficient energy for densification and smoothening. A third way to reduce the (effective) penetration depth is to choose a more grazing angle of incidence. This can go at the cost of roughness and reflectance though, as experiments have established that the mirror roughness increases and the reflectance decreases when the angle of incidence was decreased from 50° to 20° [30].

Furthermore, it is important to apply the ion bombardment at the right moment: it decreases the reflectance when it is applied during or after the deposition of the *Mo* layer, whereas it enhances the reflectance by as much as a factor of three when applied during or after the deposition of the *Si* layer [29, 31]. This result is presumably related to the different morphologies of the two layers: while Si thin films are amorphous under typical deposition conditions, Mo thin films become polycrystalline above a certain critical thickness of ~ 3 nm [15, 21]. Since the etch rate depends on the (varying) orientation of the crystallites, erosion of a polycrystalline film like Mo is a non-uniform and, thus, roughness-increasing process.

The influence of the ion energy and angle of incidence was investigated by, e.g., Voorma *et al.* [32], who deposited 16-period Mo/Si multilayer structures by e-beam evaporation. Kr^+ etching steps were included after the deposition of each Si layer. The ion angle of incidence was varied from 20° to 50° grazing, and the ion energy was varied from 300 to 2000 eV. As shown in Figure 1.5, it was found that the reflectance increases with increasing ion

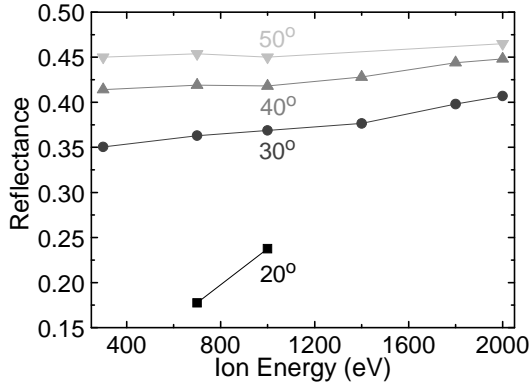


Figure 1.5. The angular and energy dependence of the near normal incidence reflectance in Mo/Si multilayers when each Si-layer is polished with Kr^+ ions [32].

energy. To a lesser extent, the reflectance also increases with less grazing angle of incidence.

The effect of the ion energy during magnetron sputter deposition was studied by variation of the bias voltage on the substrate during magnetron sputter deposition of Mo/Si multilayer mirrors [31]. The bias voltage V_{bias} evoked an ion bombardment through attraction of argon ions from the plasma. As shown in Figure 1.6, the best reflectance was obtained for multilayer optics deposited with a value of V_{bias} such that $100 \text{ V} < |V_{bias}| < 200 \text{ eV}$. A high roughness was identified as the cause of the poor reflectance without bias, while increased (ion induced) intermixing reduced the reflectance for $|V_{bias}| \geq 200 \text{ eV}$.

In view of the importance of the ion treatment of the Si layer and the effect of the parameters, a more fundamental understanding would have great surplus value to the above mentioned empirical results. As a first step to acquire a universal model of ion erosion of Si, the roughness evolution of a Si surface was studied in real-time as a function of ion energy. Chapter 7 reports the results.

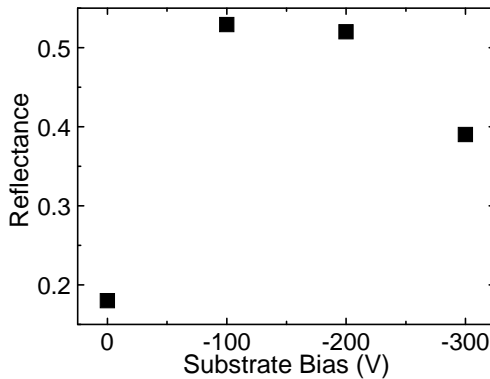


Figure 1.6. The reflectance of the Mo/Si multilayer mirrors as a function of the substrate bias [31].

1.5.3. Substrate temperature

Energy cannot only be supplied to the growing structure via ions or particles from the deposition flux, but also by heating the substrate. A major, fundamental difference between these two methods is that heating of the substrate adds energy to the whole structure, while ion bombardment only delivers energy where it is needed: in the layer to be smoothed. An illustrative experiment in this framework is the comparison between magnetron sputter deposition and e-beam evaporation at enhanced substrate temperatures [33]. It was found that increasing the energy by raising the substrate temperature T_{sub} to 200 °C (during e-beam evaporation) or by reducing the pressure to below $4 \cdot 10^{-3}$ mbar (during magnetron deposition) are equally effective to suppress columnar growth in Mo/Si multilayer structures. This growth mode is best avoided since it is characterized by a roughness that increases gradually from the bottom to the top of the multilayer stack. However, raising T_{sub} led to a larger interlayer thickness and thus a lower quality mirror than reducing the pressure during magnetron sputter deposition.

Various authors who studied the effect of T_{sub} on the quality of the multilayer, report that the best results are obtained at $T_{sub} = 200\text{-}250$ °C [26, 33, 34]. This optimum temperature coincides with a minimum in interface roughness, as comes forth from results from Voorma *et al.* (presented in Figure 1.7 [35]). Despite the low roughness of 0.33 nm, the normal incidence reflectance of a 32-period multilayer deposited at 215 °C was only 46 %, compared to 50 %

for a reference sample deposited at room temperature but in otherwise identical conditions [36]. Presumably, the reduction of the roughness by depositing at 215 °C did not lead to an increased reflectance, because the Si layers of that sample were contaminated with 5 at.% oxygen. Moreover, it is likely that temperature-induced interdiffusion of Mo and Si reduced the optical contrast, therewith decreasing the reflectance even further.

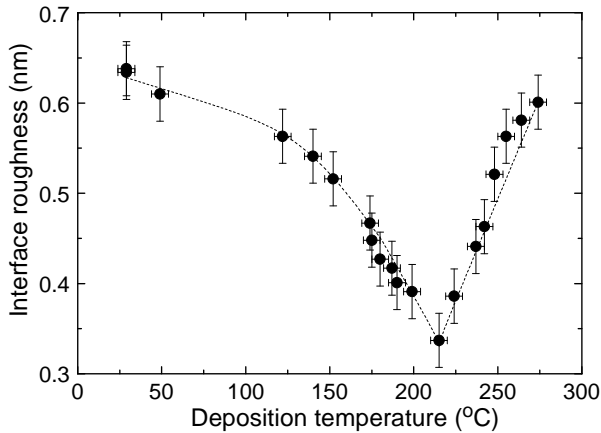


Figure 1.7. The interface roughness as a function of substrate temperature, as found by Voorma *et al.* [35].

While several authors (e.g., [26, 33-35, 37]) report investigations of depositing Mo/Si multilayer structures at elevated T_{sub} , only one group studied the effect of reducing T_{sub} below room temperature. Using cross-sectional TEM (section 2.2.4) and GIXR (section 2.2.1), the influence of T_{sub} on the roughness was investigated in the wide temperature range from -155 °C to +600 °C [38, 39]. The authors observed that the roughness-increasing columnar growth mode does not occur at $T_{sub} = -155$ °C, nor above 400 °C. Cooling of the substrate is, however, not solely of interest for roughness control. Reducing T_{sub} also lowers the probability that an (ad)atom overcomes the energy barrier for interdiffusion or surface segregation, which would lead to thinner interlayers. This interesting option has been overlooked so far, and, therefore, Chapter 6 presents a study of the thickness of the interlayer that forms during room temperature and cryogenic deposition.

1.6. This thesis

The research presented in this thesis answers several questions that remained in spite of - or sometimes arose due to - the extensive investigations of Mo/Si multilayer structures carried out since the 1980's. The majority of that work focused on lowering the roughness and increasing the reflectance. While, for instance, the dependence of the reflectance on the ion energy during deposition or ion erosion has been determined (see Section 1.5.2), much less attention was paid in this context to establishing a model that describes the roughness evolution during such processes. This issue is addressed in Chapter 7, although we were only able to determine the values of the scaling exponents that characterize ion erosion for a restricted part of the vast experimental parameter space. Due to the limited availability of experimental data, it was impossible to establish a complete model. Therefore, the main merit of Chapter 7 is that it provides a proof-of-principle for a method that is very suitable for conducting a thorough investigation of Si ion erosion, which can provide the experimental data that can lead to the construction of a universal model. Once such a model is established, it will be possible to select the ion erosion parameters such that the multilayer structure will satisfy the roughness requirements, with respect to amplitude as well as spatial frequency.

Similarly, the effect of thermal load on the multilayer structures has mainly been studied extensively through Cu-K α reflectometry, since it is a sensitive method that provides information on the key characteristics of the mirrors, viz. the d-spacing and the EUV reflectance. It provides virtually no information though on the chemical processes that affect interdiffusion and lead to changes in those characteristics. The reports that do take chemistry into account are limited to Mo/Si systems without diffusion barrier layers, and to determining which molybdenum silicide forms or when it crystallizes. Therefore, the influence of crystallization of Mo/Si systems with B $_4$ C diffusion barrier layers, which are highly relevant for practical applications, is investigated in Chapter 4. This Chapter furthermore briefly discusses the chemical processes in these structures. The chemistry of this system is elaborately addressed in Chapter 5. The obtained knowledge can be used to design more stable diffusion barriers, and optimize the diffusion barriers to maximize the reflectance of the mirror.

Perhaps due to the technical difficulties involved, so far only one group [38, 39] included cryogenic deposition in their research. They observed that

cryogenic (e-beam) deposition reduced the roughness increased the reflectance. Nevertheless, the work did not motivate further research because, probably due to ion smoothening, magnetron sputtering resulted in even better structures. Accordingly, the possibility to combine cryogenic deposition, which could lead to thinner interlayers, with ion smoothening to reduce the roughness, was overlooked. Therefore, the effect of cryogenic deposition on the interlayer thickness has been investigated in Chapter 7.

Chapter 3 does not directly add to the existing knowledge about Mo/Si multilayer structures, but instead shows how Low Energy Ion Scattering spectroscopy can be used to study interdiffusion with a sub-nanometer resolution. As such, Chapter 3 provides a very useful and sensitive technique for studying important characteristics of the mirrors, like the growth of a contamination layer, or the effect of a certain diffusion barrier layer on the diffusion rate.

2. Experimental

2.1. Sample fabrication

The samples on which results are presented in this dissertation have all been manufactured by means of e-beam evaporation and layer thicknesses were controlled by quartz crystal microbalances. Three deposition setups have been used to manufacture samples for the work presented in this dissertation: coater A [29] for the samples used in Chapters 3 and 4; coater B for the samples used in Chapter 6; and coater C for the samples investigated in Chapters 5 and 7. All three setups are ultra-high vacuum facilities and are equipped with e-beam evaporators and quartz crystal microbalances. Figure 2.1 shows schematic images of the setups.

Coater B has a special feature that is utilized to investigate cryogenic deposition of Mo/Si multilayer structures, namely its hollow substrate holder that can be filled with liquid nitrogen. As shown in Chapter 6, cooling down the substrate to cryogenic temperatures proved to be a successful way to reduce the interlayer thickness. Contrary to coater B, coater C is largely automated, which increases the reproducibility as well as the number of periods of a multilayer mirror that can be coated in one day. Coater C furthermore has a rotating sample holder that allows uniform ion beam smoothing, and is equipped with both e-beam evaporators and magnetron sputter sources. Being largely automated and having both an *in situ* X-ray reflectometer and a rotating sample holder, coater A is the deposition facility that is best optimized for the deposition of highly periodic multilayers.

2.1.1. Layer thickness control

In the case of magnetron deposition, the layer thickness can be controlled by time, once the deposition rate has been calibrated. More often though, the layer thickness is either controlled with one or more quartz crystal microbalances (QCM), or *in situ* x-ray reflectance monitoring. Layer thickness control via a QCM functions by continuously measuring the resonance frequency of a quartz crystal. The Sauerbrey equation [40] relates

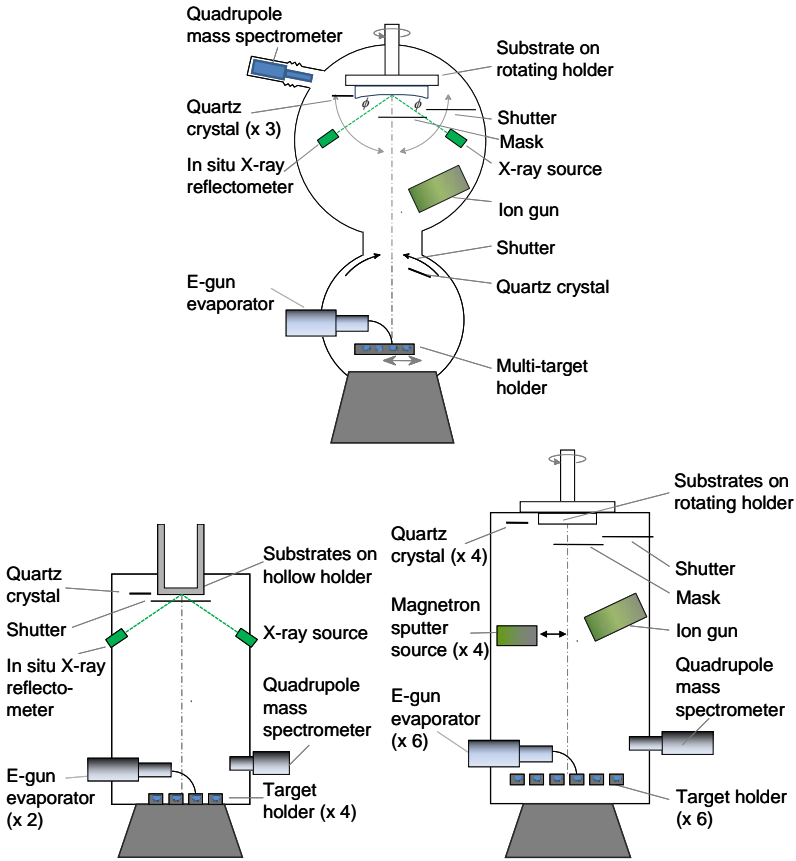


Figure 2.1. Schematic layout of coaters A (top), B (left) and C (right) deposition facilities.

Δf , the change of the resonance frequency, to the mass that has been deposited on the sensor. This equation can be adapted to yield a thickness change rather than a mass change, by dividing by the area of the crystal and the density of the layer ρ_l :

$$\Delta t = -\frac{\sqrt{\rho_q \mu_q}}{2\rho_l f_0^2} \Delta f; \quad \frac{\Delta f}{f_0} < 0.05 \quad (2.1)$$

where f_0 denotes the original resonance frequency of the uncoated crystal, ρ_q the density of quartz (2.648 g/cm^3), and μ_q its Shear modulus ($2.947 \cdot 10^{11} \text{ g/cm s}^2$). The QCM is mounted as close to the substrate as possible to obtain the maximum obtainable layer thickness accuracy of several Å.

In situ x-ray reflectance monitoring is less flexible, but very useful to prevent the accumulation of layer thickness errors [1]. An x-ray source and detector are mounted at such an angle that the thickness corresponding to one interference oscillation exactly matches the required multilayer period. Accurate layer thickness control throughout the stack is guaranteed by always stopping the deposition of the last layer of a period at the same position of the reflectance oscillation. In situ x-ray reflectance monitoring is available on coaters A and B.

2.2. Analysis techniques

To study at a (sub-)nanometer scale what physical and chemical processes occur at interfaces and in thin films is a very challenging task. Therefore, a central role in this thesis is played by analysis techniques. This paragraph gives an introduction to the used techniques.

2.2.1. X-ray reflectance and scattering

Their small wavelength of 0.01 to 10 nm makes x-rays very suitable to study changes and small details in nanometer-sized structures. Depending on the setup, x-ray scattering and reflectometry can be used for a large variety of measurements that reveal information about the layer thickness, uniformity, roughness and crystallinity of a sample.

Diffuse x-ray scattering

Chapter 7 is based on off-specular or diffuse x-ray scattering. It was first suggested in the early 1970's by Kretschmann and Kröger to use this scattering as a tool to measure and analyze the roughness of a surface [41, 42]. If a surface were perfectly smooth, all incident radiation would be either refracted into the sample or reflected specularly. In reality however, surfaces are never perfectly smooth. The macroscopic sample surface is thus modulated with a microscopic roughness. Incident light is reflected specularly with respect to the *local* surface orientation, and, therefore, roughness causes diffuse scattering around the main direction given by the *global* surface orientation. This is illustrated in Figure 2.2. The roughness can be reconstructed from the diffuse scattering by regarding the surface as a superposition of diffraction gratings, each with its own lateral and vertical

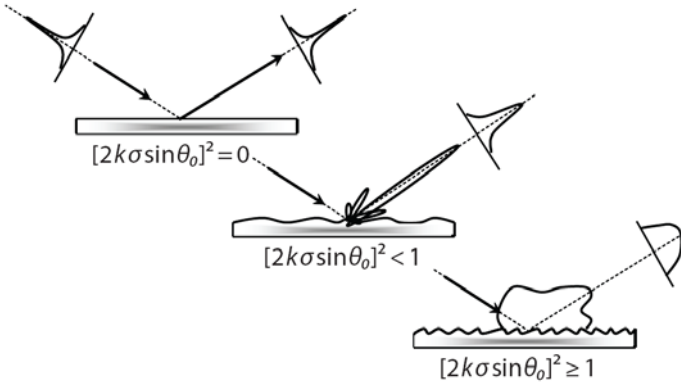


Figure 2.2. The shape of the reflected beam changes as the surface changes from perfectly smooth (top) via slightly rough (middle) to very rough (bottom).

scale. The scatter angle provides the lateral scale of the roughness; the intensity provides the vertical scale (i.e., the amplitude of the roughness σ).

In order to find the roughness of a surface from the diffuse scattering, it is necessary to describe it by the so-called Power Spectral Density (PSD). The PSD is defined as the amplitude of the thickness variation as a function of spatial frequency ν . Equation (2.2) relates the PSD(ν) to the scattered intensity at a scatter angle θ_S (with respect to the sample surface):

$$PSD_{1D}(\nu) = \frac{16\pi \sin \theta_0 \sqrt{\cos \theta_0 \cos \theta_S}}{k^3 \cdot Q(\varepsilon, \theta_0, \theta_S)} \cdot \frac{1}{I_0} \frac{dI_{1D}}{d\theta}, \quad (2.2)$$

$$\text{where } Q(\varepsilon, \theta_0, \theta_S) = |1 - \varepsilon|^2 |t(\theta_0)t(\theta_S)|^2, \quad (2.3)$$

$$I_{1D} = \int I(\theta_S, \phi_S) d\phi_S, \quad (2.4)$$

$$\text{and } \nu = \frac{1}{\lambda} |\cos \theta_S - \cos \theta_0|. \quad (2.5)$$

The subscript $1D$ denotes that the system is assumed to be isotropic and can, thus, be described one-dimensionally. ν denotes the spatial frequency, θ_0 the grazing angle of incidence, $k = 2\pi / \lambda$ the wave number, I_0 the intensity of the incoming beam, ε the dielectric constant, and $t(\theta_0)$ and $t(\theta_S)$ the transmission at θ_0 and θ_S , respectively. Equation (2.4) serves to convert the scattered intensity $I(\theta_S, \phi_S)$ into a one-dimensional signal by integrating over the azimuthal angle ϕ_S .

Equation (2.2) is a result of first-order scalar perturbation theory. Hence, it is only valid in the smooth surface limit, i.e., when the contribution of higher order terms is negligible because $[2k\sigma \sin \theta_0]^2 \ll 1$. This condition can be fulfilled by choosing θ_0 small and/or k large. Hard x-ray scattering is used in Chapter 7 to study the roughness evolution of a Si layer during ion erosion in real-time.

Grazing Incidence X-ray Reflection

The specular reflectance as a function of the angle of incidence θ is measured during Grazing Incidence X-ray Reflection (GIXR) scans. This type of measurements is also referred to as θ - 2θ scans and is particularly useful for periodic multilayer structures. Maxima occur whenever the Bragg condition as given by Equation (1.2) is fulfilled. The period of the structure can, thus, be determined from the position of the maxima with an accuracy of up to 0.01 nm, depending on the quality of the multilayer. Furthermore, information about the roughness, layer thickness variations and layer densities can be extracted from the intensities of the various maxima by using simulation software like IMD by David Windt [43].

Wide Angle X-ray Diffraction

The crystallinity of the structure is a third property that can be probed with x-ray radiation. During Wide Angle X-ray Diffraction (WAXRD) scans (also referred to as detector scans), the angle of incidence is fixed while the detector scans over a certain angular range. When the sample is (poly)crystalline, diffraction peaks will be observed at each angle where the Bragg condition (Equation (1.2)) is fulfilled, where Λ now denotes the distance between two crystal planes.

In the case of monocrystalline samples, diffraction peaks appear only at certain points in angular space. Hence, the diffraction pattern has to be recorded as a function of both the azimuth φ and the polar angle θ . The samples that are encountered in this thesis though are either amorphous or polycrystalline. In the latter case, the azimuthal orientation of the crystallites is random, and therefore it suffices to measure a WAXRD spectrum as a function of the polar angle at one, arbitrary azimuth only. The azimuth is then chosen such that the (monocrystalline) Si substrate does not contribute to the spectrum.

Chapter 6 is largely based on GIXR and WAXRD analysis. The spectra have been acquired using the Philips X'Pert double crystal x-ray diffractometer with Cu K_α radiation ($\lambda = 0.154$ nm).

2.2.2. (Hard) X-ray photoelectron spectroscopy

X-ray photoelectron spectroscopy (XPS) is a common analysis technique to determine the composition of the surface layer of a sample. During a measurement, the sample is exposed to an x-ray beam with a specific photon energy $h\nu$. When an atom in the sample absorbs a photon, the atom may emit one of its core electrons. Conservation of energy dictates that the kinetic energy E_K of this so-called photoelectron equals $h\nu$ minus the electron binding energy E_B and the spectrometer workfunction W :

$$E_K = h\nu - E_B - W. \quad (2.6)$$

Because $h\nu$ and W are accurately known constants, a measurement of the photoelectric current as a function of E_K is easily converted into a spectrum as a function of E_B . Since each element has a characteristic value of E_B , the peaks in an XPS spectrum can be used to identify the elements in the sample. As E_B can be determined with a typical precision of 0.1 eV, the measurement is even sensitive enough to extract information about the chemical environment of the atom. The concentration of the various elements in the sample can be deduced from the peak areas.

XPS is a surface sensitive technique because the photoelectrons only have a limited average distance before they interact inelastically with atoms in the samples. The attenuation length λ_A is defined as the distance where the probability P that a photoelectron has not interacted inelastically has dropped to $1/e$: $P = \exp(-x/\lambda_A)$, where x is the travel distance. The value of λ_A depends on the material and the energy of the photoelectrons. For a standard Al K_α source, $h\nu = 1486.6$ eV and λ_A is typically 2-3 nm. The analysis depth is usually quoted as $3 \cdot \lambda_A = 6-9$ nm, although the analysis is heavily biased towards the surface: two-thirds of the signal stems from the outer $1 \cdot \lambda_A$.

A standard XPS measurement does not disclose depth-resolved information. However, depth-profiles can be obtained by alternating measurements and

erosion of the sample surface by noble gas ion bombardment. Depth-profiling is a very useful technique, especially when used on a relative basis. It suffers though from its destructive character; the depth-profiles are distorted by ion-induced intermixing and preferential sputtering of light elements. Angular-Resolved XPS (AR-XPS) and variable energy Hard X-ray Photoelectron Spectroscopy (HAXPES) on the contrary are two non-destructive ways to obtain depth-resolved information. In AR-XPS, the detector angle is varied, which adds an angular dependency to the path-length and, hence, to the escape probability of the photoelectrons:

$$P = \exp(-d / \lambda_A \cos \chi). \quad (2.7)$$

In this Equation, d is the distance from the surface where the photoelectron is generated, and χ the angle at which the detector is placed, measured with respect to the surface normal. Equation (2.7) indicates that a grazing detector angle results in a more surface sensitive measurements than a (near-) normal configuration. By measuring an XPS spectrum at two or more detector angles, it can be established which elements are located near the surface and which elements are further away from the surface.

Another way to vary the escape depth is to fix χ and vary the attenuation length. This can be achieved by variation of the energy of the incident x-rays, because λ_A scales roughly with $E_K^{0.7}$. Similar to the variation of the detector angle in AR-XPS, variation of the x-ray energy changes the analysis depth and, hence, yields depth-resolved information. Moreover, the larger analysis depth (λ_A is typically 6 nm at $h\nu = 4$ keV) allows non-destructive investigation of deeper layers than standard XPS. Nevertheless, variable energy HAXPES is used less frequently than AR-XPS because it requires access to a hard x-ray source of variable energy (usually at a synchrotron beamline).

The results of a variable energy HAXPES study of thermally enhanced diffusion in Mo/diffusion barrier/Si and Si/diffusion barrier/Mo trilayered structures are presented in Chapters 4 and 5. The measurements have been conducted at the HIKE experimental station at the KMC-1 beamline of the BESSY II storage ring facility. In Chapters 5 and 6, XPS depth profiling is used to investigate the influence of cryogenic deposition on the interfaces of multilayer structures. The measurements have been performed with a Thermo Theta Probe.

2.2.3. Low Energy Ion Scattering spectroscopy

Low Energy Ion Scattering spectroscopy (LEIS) is a technique that is selectively sensitive to the surface of a sample. The expertise to overcome the problematically low sensitivity of the earlier instruments was developed during the last few decades, resulting in the introduction of a commercial, high sensitivity LEIS apparatus in 2008.

In LEIS, the sample is bombarded with ions, usually of a noble gas, with a well-defined energy of 1-10 keV. When a projectile with mass m_1 and energy E_0 collides elastically with a target atom with mass m_2 at rest, the energy E_f of the projectile *after* the collision is given by:

$$E_f = \left(\frac{\cos \theta \pm \sqrt{\left(\frac{m_2}{m_1}\right)^2 - \sin^2 \theta}}{1 + \frac{m_2}{m_1}} \right)^2 \cdot E_0, \quad (2.8)$$

where θ denotes the scatter angle [44, 45]. For fixed E_0 , m_1 , and θ (provided $\theta > 90^\circ$), E_f only depends on m_2 and, hence, a measurement of E_f can be used to determine the composition of a sample surface.

Elastic collisions at the outermost atomic layer give rise to the so-called binary collision peaks in the LEIS spectrum, where each peak corresponds to a certain mass, and thus to a certain element. LEIS thanks its extreme surface selectivity to the fact that all projectiles that penetrate the sample beyond the first monolayer are effectively neutralized [46-48]. Such neutralized particles do not contribute to the spectrum because the detector is only sensitive to ions. Depending on the composition of the surface though, there is a certain probability that the neutralized and scattered ions are reionized upon leaving the surface. These reionized particles carry less energy than projectiles undergoing a single two-body collision, due to the stopping of atoms by the matter. The average energy loss $\langle \Delta E \rangle$ is given by

$$\langle \Delta E \rangle = - \int_x S(E, x) dx, \quad (2.9)$$

where S is the (material- and energy-dependent) stopping power, and x the travel distance of the projectile. The probability for reionization is lower than the probability for ion survival after a binary collision at the surface. Therefore, a LEIS spectrum is characterized by distinct, surface-related, binary collision peaks superposed on a lower-intensity continuum that is related to the subsurface. Chapter 3 describes how the depth-resolved information can be extracted from the continuum. This procedure is used in Chapters 3 and 4 to study diffusion in Mo/Si and Mo/B₄C/Si layered systems.

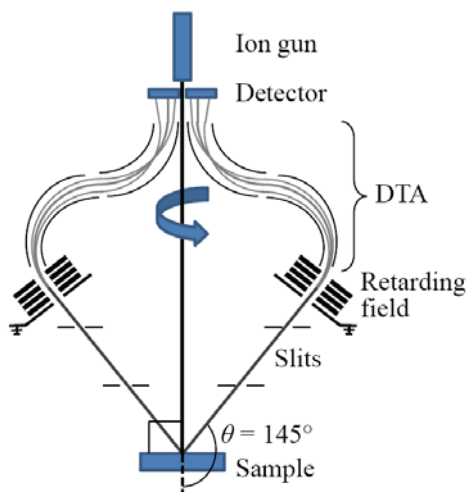


Figure 2.3. Schematic, cross-sectional image of the LEIS instrument used for measurements reported in this thesis. The double toroidal analyzer (DTA) and the position sensitive detector give the instrument a high sensitivity.

LEIS is, in principle, a destructive technique, because the energetic ions induce sputtering and intermixing. However, smart detector design and rastering of the ion beam over a relatively large surface area can reduce the required ion fluence per measurement to 10^{13} ions/cm². This number is small compared to the surface atomic density of 10^{15} cm⁻² and, therefore, high sensitivity LEIS is a virtually non-destructive technique. The LEIS instrument used for the measurements in this thesis thanks its high sensitivity to a double toroidal analyzer (DTA) and a position sensitive detector. The DTA, depicted in Figure 2.3, is rotationally symmetric around the ion beam in order to maximize the solid angle of ion acceptance. The DTA deflects the accepted ions twice, such that it acts energy-dispersively and maps the ions onto a

position sensitive detector. Using this configuration, a range of typically 100 eV is measured simultaneously, which greatly reduces the measurement time needed to record a full spectrum.

2.2.4. Transmission Electron Microscopy

The structure of a sample can be visualized with Transmission Electron Microscopy (TEM). A focused electron beam with an energy of typically 40-400 keV is passed through a thin sample (~100-300 nm thick). Differences in composition or structure affect the electron absorption by the sample, and, hence, an image of the sample is created when the electron beam hits a fluorescent screen or CCD camera, after it has been magnified by a factor of 10^4 - 10^6 . As the absorption coefficient is largely determined by the electron density, sample regions with high-Z elements appear dark on TEM images, while regions with mostly low-Z elements are light.

Planar TEM samples are usually fabricated by deposition of the structure of interest onto a special TEM grid that is sufficiently thin to allow the electron beam to pass through. In the case of multilayer or interface analysis, its counterpart cross-sectional TEM is of particular interest, because the layers and interfaces are directly visible. A sample for cross-sectional TEM is prepared by cutting a cross-sectional slice from the sample, followed by an elaborate thinning procedure of mechanical polishing and grazing-angle ion etching.

The (cross-sectional) TEM images in this thesis have been acquired with a Philips CM300ST-FEG (S)TEM instrument. In Chapter 4, TEM analysis is used in combination with LEIS to investigate the role of crystallinity on the diffusion rate in a Mo/B₄C/Si layered system.

3. Diffusion and interaction studied non-destructively and in real-time with depth-resolved Low Energy Ion Scattering spectroscopy

3.1. Abstract

An analysis procedure was developed that enables studying diffusion in ultra-thin films by utilizing the depth-resolved information that is contained in Low Energy Ion Scattering spectroscopy (LEIS) spectra. Using a high-sensitivity analyzer/detector combination allows for such a low ion fluence that the ion-induced perturbation caused by this technique is negligible and not measurable with LEIS. The developed analysis procedure provides a unique opportunity to quantitatively study diffusion processes in nano-scaled systems. It was applied to the Mo/Si system, a system that is relevant for Extreme Ultraviolet optics.

3.2. Introduction

In this chapter we propose an application of Low Energy Ion Scattering spectroscopy (LEIS) that opens the possibility to study diffusion in solids non-destructively with a depth resolution of 0.2-1 nm (depending on probed depth and sample structure and composition) and a maximum probed depth of 5-10 nm. This range is of interest for many ultra-thin film applications where, besides the absolute surface, the subsurface is important. Although (angular resolved) X-ray photoelectron spectroscopy (XPS) can measure in this range as well, LEIS can be an alternative for elements for which XPS has a poor sensitivity, or for a combination of elements with overlapping XPS peaks. A further advantage of LEIS over XPS is its higher depth resolution, which results in a better picture of the diffusion profile. No quantitative LEIS diffusion studies have been reported thus far, except for a couple of studies where the diffusion was monitored via the change in the characteristic LEIS surface peak [49-52], which represents the composition of the outermost atomic layer [44]. Since the symmetry of the matrix of surrounding atoms is obviously broken at the surface, the migration from the second to the first, outermost monolayer may be governed by different energetics than the

diffusion through ‘bulk’ material. As such, the use of the surface concentration as a measure for bulk diffusion is questionable. Van Leerdaam *et al.* [53, 54], on the contrary, studied diffusion qualitatively by obtaining information from the part of the spectrum that is not related to the outermost atomic layer, but to the subsurface. Using the depth-resolved information contained in that part of the spectrum, this chapter demonstrates that it is possible to conduct *quantitative* diffusion studies with LEIS. With respect to the previous LEIS diffusion studies involving the surface peak, this approach has the additional advantage that (hydrocarbon) contamination is not problematic, since the relevant part of the spectrum corresponds to the material underneath. The waived demand on surface cleanliness simplifies transport to the LEIS facility and extends its applicability to materials that form a closed oxide when exposed to the ambient.

The proposed approach is applied to the Mo/Si system, because of its relevance for multilayer reflective X-ray optics, like used for e.g. Extreme Ultraviolet lithography. As the multilayers are nano-scaled devices where (prevention of) interdiffusion is crucial, this system presents an adequate test case for the developed analysis method. Moreover, this new approach facilitates studying interdiffusion processes in Mo/Si thin film systems with sub-nanometer resolution. This allows studying structures with only a few layers and not only multilayer stacks, making it possible to selectively study one interface (e.g., the Si-on-Mo interface) without interference from the other interface (the Mo-on-Si interface).

As described in Section 2.2.3, LEIS reveals information about the composition of a surface by bombarding the sample with noble gas ions of a well-defined, relatively low energy (typically 2-3 keV He⁺) [44]. The energy of backscattered ions at a specific scatter angle is measured and used to identify the atomic species at the sample surface via Equation (2.8). Projectiles that penetrate the sample beyond the first monolayer are neutralized and are, consequently, not detected [44, 55]. However, on their way out of the sample, there is a certain probability that the projectiles are reionized at the surface. This reionization probability depends on the atomic species at the sample surface and is especially large for oxygen. The reionized projectiles have a lower energy than projectiles undergoing a pure two-body collision, because of an average additional energy loss $\langle \Delta E \rangle$ due to the stopping of atoms by the matter. The relationship that Equation (2.9) provides between depth and energy-loss means that the energy-scale of LEIS spectra

can be converted into a depth-scale, allowing us to extract concentration profiles.

3.3. Experimental details

LEIS measurements are performed with the Calipso LEIS instrument, which is described in detail in Ref. [44]. The geometry of the instrument is such that $\theta_{in} = 0^\circ$ (normal incidence) and the backscatter angle $\theta_{out} = 145^\circ$. Assuming that the stopping power S is energy independent, Equation (2.9) reduces to

$$\langle \Delta E \rangle = S \left[\left| d / \cos(\theta_{in}) \right| + \left| d / \cos(\theta_{out}) \right| \right] = 2.2 d S, \quad (3.1)$$

where d is the depth at which the projectile is backscattered. A 3.0 keV He⁺ beam with a beam current of 2.9 nA and a diameter 0.15 mm is used. In order to minimize the damage to the samples, the beam is scanned over an area of 3 mm². Each measurement lasts 45 s. The fraction of backscattered He-ions is measured as a function of their kinetic energy $E_{scatter}$ with a so-called Double Toroidal Analyzer (DTA), which images the ions, according to their energy, onto a position sensitive detector. It is essential to use this analyzer-detector combination, because its large solid angle of detection combined with the parallel detection increases the sensitivity by orders of magnitude and allows reducing the ion fluence Q . As such, Q is very low compared to the surface atomic density n ($Q=10^{13}$ cm⁻²/measurement; $n=10^{15}$ cm⁻²), and therefore, ion-induced sputtering and intermixing are negligible (sputter yield is 8% [56]). In order to study the interdiffusion, Mo/Si samples have been prepared using deposition by means of electron beam evaporation on silicon wafers at room temperature. The base pressure in the coating facility is better than $2 \cdot 10^{-8}$ mbar. The deposition rate is 0.02 nm/s for Mo and 0.03 nm/s for Si. The samples consist of 10.0 nm c-Mo followed by 4.0-7.0 nm of amorphous Si. The thickness of the layers is controlled by a set of three quartz crystal microbalances, which have been calibrated by X-ray reflectometry. The deposition setup is described in detail by Schlattmann *et al.* [29]. To investigate the diffusion in the Mo/Si system, LEIS experiments are conducted before thermal treatment of the samples as well as during heating up to 500 °C (systematic error <30 °C, reproducibility <2 °C). This temperature is reached 40-50 seconds after switching on the heating filament and monitored with an Impac 140 pyrometer.

3.4. Results

Figure 3.1 (dashed curve) shows the LEIS spectrum of a MoSi_2 reference sample. The Mo, Si and O surface peaks are indicated. In the absence of other heavy elements, the range in between the Si and Mo peaks (at 1720 and 2510 eV) can be uniquely attributed to (subsurface) Mo. At lower energies on the other hand, various lighter elements (Si and surface contaminants like C, N and O) contribute to the signal, making it impossible to attribute it to a specific element. As such, only the high energy part of the spectrum, which is related to Mo alone, is analyzed in this chapter. In the spectrum of the MoSi_2 reference sample, the signal in the analyzed window (1800 - 2400 eV), which reflects the Mo concentration profile as a function of depth, is flat, as one would expect for a homogeneous compound[†].

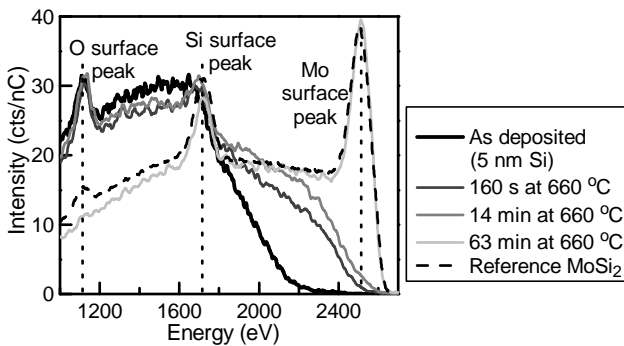


Figure 3.1. The evolution of the LEIS spectrum during annealing at 660 °C.

The stopping power is obtained from Figure 3.2, which shows the 3 keV He^+ LEIS spectra of Mo samples covered with 4.0, 5.0 and 7.0 nm Si. The thicker the Si film, the lower is the energy of the onset of the Mo-related high-energy tail. As the Si thickness is known accurately, Figure 3.2 can be used to determine the stopping power in silicon: $S_{\text{Si}} = (36 \pm 3)$ eV/nm, which is close to reported values [57] (from 33 eV/nm at 1.85 keV to 35 eV/nm at 2.5 keV). S_{Si} varies only slightly with energy in this regime, which justifies treating it as a constant in Equation (3.1).

[†] Provided that the stopping power and the reionization probability are constant over the energy range.

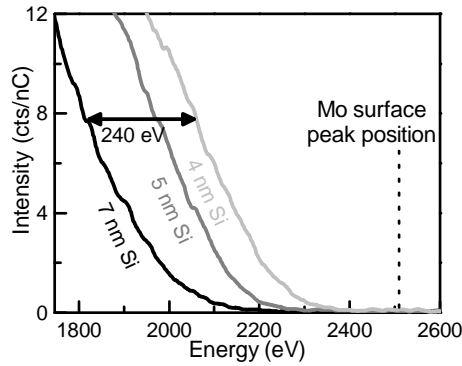


Figure 3.2. Partial 3 keV He^+ LEIS spectra of samples with 4.0, 5.0 and 7.0 nm Si.

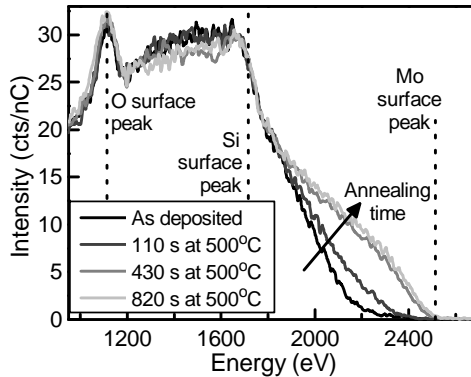


Figure 3.3. The evolution of the LEIS spectrum of the sample (10.0 nm Mo / 5.0 nm Si) during annealing at 500 °C.

Figure 3.3 shows a typical example of the evolution of the LEIS spectrum during annealing at 500 °C. Quantification of the data in the 1800 - 2400 eV range is carried out in four steps:

1. The measured intensity $I(E)$ in a certain detection channel is proportional to the relative Mo concentration C_{Mo} (in atomic fraction), the Mo scattering cross-section σ , the width of the detection channel (ΔE_{dc} , in eV), and, in the absence of other strongly reionizing elements at the surface, the oxygen surface coverage $C_{O,surf}$. $I(E)$ is inversely proportional to the stopping power S of helium by the compound (viz. a large S means that a small difference in the depth at which the scattering occurs causes a big difference

in the kinetic energy of the ion). Hence $I(E) = AC_{Mo}(x)C_{O,surf} / S$, where x is the distance from the interface, A is a factor that contains the incident ion current, the differential scattering cross-section for Mo, the probability for reionization of He by O, and an instrumental factor. Normalization on the spectrum of a Mo reference sample allows dividing out A and extracting $C_{Mo}(E)$:

$$\frac{I_{sample}(E)}{I_{Mo\ reference}(E)} = \frac{A \cdot C_{Mo,sample}(E)}{A \cdot 1} \frac{C_{O,surf,sample}}{C_{O,surf,Mo\ reference}} \frac{S_{Mo}}{S_{Si}} \quad (3.2)$$

The dependence on $C_{O,surf}$ is taken care of by normalizing both the sample spectrum and the Mo reference spectrum on the oxygen peak height. The stopping power in the Mo reference is $S_{Mo} = 50$ eV/nm [58], while the stopping power in the sample spectrum is approximated by $S_{sample} = S_{Si} = 36$ eV/nm, as established above.

2. As a function of the annealing time t , the scattering energy $E_k(t)$ is determined where C_{Mo} reaches a specific value k . k cannot exceed the solubility limit $C_{Mo,max}$ and is chosen low (10%) in order to minimize the error that is made by using S_{Si} , i.e. ignoring the change in the stopping power due to composition changes during the diffusion.

3. The distance from the original interface $x(t)$ is obtained via $x(t) = [E_k(t) - E_k(0)] / [2.2S_{Si}]$.

4. Clearly, $C_{Mo}(x,t)$ is the complement of $C_{Si}(x,t)$. Using the solution to the diffusion equation for linear diffusion into a semi-infinite medium, $x(t)$ is related to \sqrt{Dt} , where D denotes the diffusion coefficient. This solution [59] holds for the main diffusing species, in this case Si, and reads [60]:

$$C_{Si}(x,t) = 1 - C_{Mo}(x,t) = C_{Si,max} \left[1 - \text{erf} \left(\frac{x}{2\sqrt{Dt}} \right) \right]. \quad (3.3)$$

erf denotes the errorfunction. $C_{Si,max}$ is the solubility limit of the diffusant Si in the host matrix and is $\frac{2}{3}$, because MoSi_2 is the main compound that is formed at this temperature [61, 62]. The Si overlayer is consumed as Si diffuses into the Mo, thus bringing the position of the interface closer to the surface. So, when evaluating the diffusion profile, the shift in the position of the interface has to be taken into account. This shift, being the decrease in Si overlayer thickness ΔSi , equals the total amount of Si diffused into the Mo. As such, ΔSi is found by integration of Equation (3.3):

$$\begin{aligned}
\Delta Si(t) &= \int_0^{\infty} C_{Si}(x,t) dx \\
&= \int_0^{\infty} \left[\frac{2}{3} - \frac{2}{3} \operatorname{erf} \left(\frac{x}{2\sqrt{Dt}} \right) \right] dx \\
&= \Delta Si(\sqrt{Dt}).
\end{aligned} \tag{3.4}$$

For each recorded spectrum, the value of \sqrt{Dt} is determined according to the above described analysis procedure. Figure 3.4 shows the result as a function of \sqrt{t} . The diffusion obeys Fick's second law, with $\sqrt{D} = (0.29 \pm 0.02)$ nm/s^{1/2}, i.e., $D = (8.4 \pm 1.2) \cdot 10^{-20}$ m²/s. This value is comparable to values found for the Mo/Si system by Holloway *et al.* [63]. After 430 seconds, the diffusion saturates as a result of Si exhaustion. However, as Figure 3.3 shows, the intensity profile is not flat, indicating a concentration gradient. Furthermore, the absence of a Mo-related surface peak means that no Mo is present at the surface and leads to the hypothesis that native SiO₂ slows down or even blocks further diffusion. This finding is in accordance with the results of Dan'ko *et al.*, who report that the diffusion coefficient of Si in a SiO₂ matrix is as much as ten orders of magnitude lower than in a MoSi₂ matrix [64]. Only when a duplicate of the sample is annealed for one hour at 660 °C, a surface peak forms and the profile becomes flat and identical to the profile of a MoSi₂ reference sample (see Figure 3.1). At this temperature, SiO₂ decomposes into SiO(g) and 1/2O₂(g) [65].

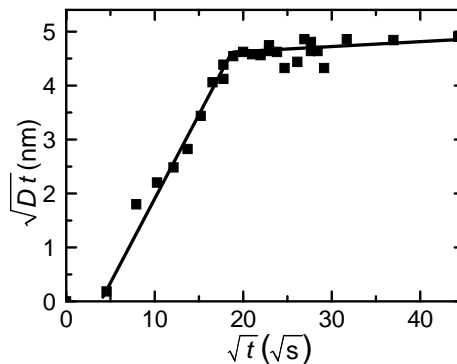


Figure 3.4. The quantity \sqrt{Dt} plotted as a function of \sqrt{t} . The lines represent the best linear fit for the corresponding part of the graph and the slope represents \sqrt{D} .

3.5. Conclusions

In conclusion, we have demonstrated that LEIS can be used in modern thin-film science when depth-resolved information about the composition of the topmost 5-10 nm and a time resolution of 1 minute are required, albeit with the restriction that the difference in mass of the studied elements needs to be sufficiently large in order to separate their respective contributions. This quality has been used to study a diffusion process, and a quantification procedure is proposed.

3.6. Acknowledgments

This work is part of the FOM Industrial Partnership Programme I10 ('XMO') which is carried out under contract with Carl Zeiss SMT AG, Oberkochen and the 'Stichting voor Fundamenteel Onderzoek der Materie (FOM)', the latter being financially supported by the 'Nederlandse Organisatie voor Wetenschappelijk Onderzoek (NWO)'.

4. Enhanced diffusion upon amorphous-to-nanocrystalline phase transition in Mo/B₄C/Si layered systems

4.1. Abstract

The effect of the amorphous-to-nanocrystalline transition of a thin layer on the diffusion across that layer has been investigated for the first time. A real-time study with LEIS showed that the initially linear diffusion in nanoscale layered Mo/B₄C/Si thin film structures is subject to an instantaneous, ten-fold enhancement of the diffusion rate. Chemical characterization disclosed no direct link between chemical changes in the interface and the enhanced diffusion rate. However, transmission electron microscopy revealed that the diffusion acceleration was caused by the amorphous-to-nanocrystalline transition of the MoSi₂ interface, which facilitates grain boundary diffusion.

4.2. Introduction

Diffusion at the nanometer-scale is a vast research field in micro-electronics, optics, and thin-film physics in general. The influence of the materials' morphology (amorphous, nanocrystalline, microcrystalline) on the diffusion rate is widely recognized and the comparison between diffusion through amorphous and crystalline layers has been the subject of several investigations [66, 67]. Amorphous-to-polycrystalline transitions are regularly observed in thin film systems once the film reaches a certain temperature or thickness. This transition can be expected to increase the diffusion rate by enabling an additional diffusion mechanism to interstitial or substitutional diffusion, namely grain boundary diffusion (see, e.g., Ref. [68]). This chapter reports on the interplay between morphology and diffusion processes at the sub-nanometer scale using several state-of-the-art analysis techniques, and includes evidence of a crystalline transition directly causing accelerated diffusion across an interlayer.

A Mo/B₄C/Si layered system is selected for this study as a typical example of current thin film research. It is applied in modern multilayer reflective optics where diffusion damages the layered structure and limits the performance

[69]. While Mo and Si are selected for their favorable optical constants, the role of B_4C is to reduce interdiffusion of Mo and Si. The system shows an amorphous-to-nanocrystalline transition when the $MoSi_2$ interface that forms upon diffusion reaches a certain critical thickness [17]. We will show in this chapter that this crystallization of the interface brings about an instantaneous increase of the diffusion rate by up to one order of magnitude.

4.3. Diffusion rate

4.3.1. Experimental details

The Mo/ B_4C /Si trilayered structures have been prepared using physical vapor (electron-beam) deposition. The UHV deposition facility was described in detail in Section 2.1 and Ref. [22]. The base pressure was lower than $2 \cdot 10^{-8}$ mbar. A set of three quartz crystal microbalances was used to control the film thickness, and the deposition rate was 0.02 nm/s for Mo and 0.03 nm/s for B_4C and Si. The samples consisted of 10.0 nm *c*-Mo / d_{B_4C} B_4C / 5.0 nm *a*-Si trilayers, deposited onto superpolished silicon wafer substrates at room temperature. Deposition flux masking was implemented during B_4C deposition, yielding samples with varying B_4C thickness $d_{B_4C} = 0 - 1.6$ nm in a single coating run, ensuring identical conditions for all samples. The annealing temperature of 500 °C (systematic error <30 °C, reproducibility <2 °C). was reached 40-50 seconds after switching on the heating filament and was monitored with an Impac 140 pyrometer.

To investigate the diffusion process with the high time-resolution of one minute, we performed high-sensitivity Low Energy Ion Scattering spectroscopy (LEIS) measurements both before and during the annealing treatment. Using the procedure proposed in Chapter 3, these measurements provided us with the Mo concentration profile. Combining this concentration profile with Fick's second law yielded the diffusion-related quantity \sqrt{Dt} , where D denotes the diffusion coefficient and t the annealing time. The procedure in Chapter 3 requires that the main diffusing species and the stoichiometry of the formed compound are known. Following a study of the Mo/Si system reported in Ref. [60], the main diffusing species was assumed to be Si, while the predominantly formed compound was $MoSi_2$ [18, 70, 71]. The extraction of \sqrt{Dt} further requires knowledge of the He stopping powers in B_4C (S_{B_4C}) and in Si ($S_{Si} = 36 \pm 3$) eV/nm [70]). $S_{B_4C} = (54 \pm 3)$ eV/nm

was established following the procedure used in Ref. [70]. The LEIS measurements were performed using a 3 keV He^+ beam and the Calipso LEIS instrument, which was described in detail in Refs. [44, 72]. The high sensitivity of this instrument allows reduction of the ion fluence to a level below the detection limit of ion-induced sputtering or intermixing.

4.3.2. Results

As an example, Figure 4.1 displays the evolution of the LEIS spectrum of a sample with $d_{B_4C} = 1.3$ nm upon annealing at 500 °C. The changes in the 1850-2580 eV range are evident: the onset shifts to a higher energy, and the intensity increases. In the absence of other heavy elements, that range could be uniquely attributed to Mo. The changes thus reflect the buried Mo effectively moving towards the sample surface as a result of the downward diffusion of Si. At energies below 1850 eV however, various lighter elements (Si, O, C, B) contribute to the signal and make it impossible to attribute it to a specific element. As such, only the Mo-related, high energy part of the spectrum (>1850 eV) is considered in detail.

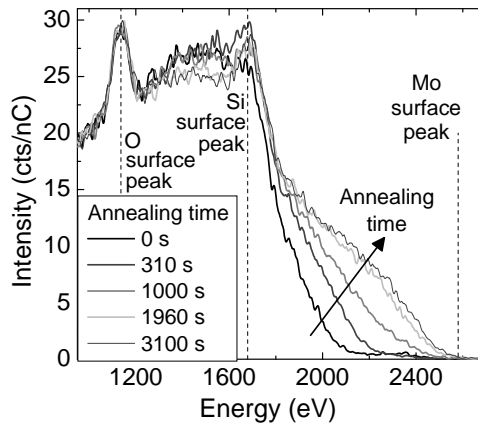


Figure 4.1. The evolution of the LEIS spectrum of the Mo/B₄C/Si sample with $d_{B_4C} = 1.3$ nm, during annealing at 500 °C.

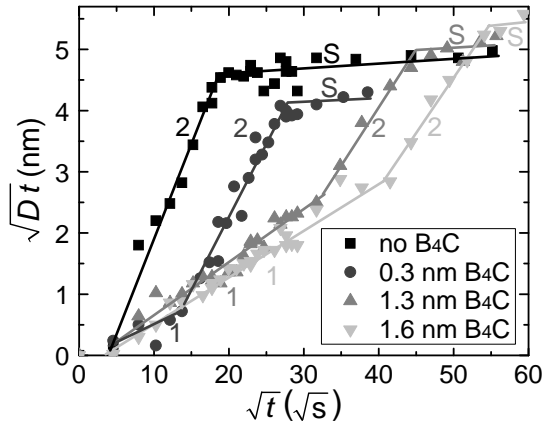


Figure 4.2. \sqrt{Dt} , the quantity obtained from applying Fick's law to the quantified LEIS spectra of four samples with different d_{B_4C} , plotted as a function of \sqrt{t} . The lines represent the best linear fit for the corresponding part of the graph and their slope represents \sqrt{D} . The numbers 1 and 2 indicate the diffusion stage; an S indicates steady state.

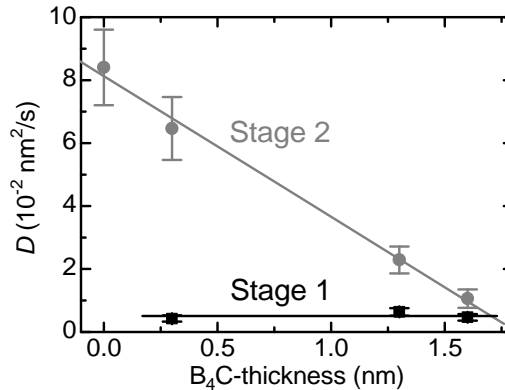


Figure 4.3. The diffusion coefficient D in Stages 1 and 2, as a function of B_4C interlayer thickness d_{B_4C} .

Figure 4.2 shows the evolution of \sqrt{Dt} for four samples with different d_{B_4C} , as obtained from quantification of the LEIS spectra. Without B_4C interlayer, the diffusion obeyed Fick's second law with $D = (8.4 \pm 1.2) \cdot 10^{-20} \text{ m}^2/\text{s}$. This value is comparable to literature values for the Mo/Si system [60, 63]. Adding a B_4C -layer, which is known to reduce interdiffusion [23], initially reduced the diffusion constant to $D = (5.1 \pm 1.2) \cdot 10^{-21} \text{ m}^2/\text{s}$, regardless of d_{B_4C} . We

call this Stage 1. At a certain moment however, a remarkable transition to a regime with an up to fifteen times higher D (Stage 2) was observed. Finally, an apparent steady state (i.e. no changes observed at a timescale of an hour) is reached due to silicon depletion. Figure 4.3 displays D in Stage 1 and 2 as a function of d_{B_4C} . It shows that D_{stage1} is independent of d_{B_4C} (the duration of Stage 1 increases though for thicker d_{B_4C}), while D_{stage2} reduces linearly with increasing d_{B_4C} .

4.4. Chemistry

In explaining the peculiar enhancement of the diffusion in Stage 2, the morphology of the structure will be investigated. Beforehand, however, we will study the chemical processes upon annealing and exclude that the system's chemistry plays a decisive role before investigating the morphology of the structure: in view of reported B_4C decomposition and MoB_x formation [73], it is conceivable that a chemical reaction between Mo, Si and B_4C brings about the two-stage process: upon entering the B_4C layer, the diffusant is trapped in a chemical bond, e.g. MoB_x or SiC_x . During Stage 1, the chemical trapping would slow down the diffusion, until Stage 1 ends when the complete B_4C layer is consumed. In Stage 2, the faster process of unhindered physical diffusion would take over.

4.4.1. Experimental details

The chemical reactivity of the interface and particularly its role in relationship with the two-stage process was investigated with HAXPES. Compared to conventional X-ray Photoelectron Spectroscopy (XPS), HAXPES takes advantage of a higher X-ray energy, which increases the inelastic mean free path (IMFP) of the photoelectrons from typically 2.5 nm (XPS at 1486.6 eV) to 3.5-6 nm (HAXPES at 2010 and 4020 eV, respectively). This allowed us to investigate an interface buried at a depth of 5 nm non-destructively. The HAXPES measurements have been performed at the HIKE experimental station [74] at the KMC-1 beamline [75] of the storage ring facility BESSY II. Samples with 1.3 nm B_4C , prepared using various annealing times at 500 °C, were first characterized with LEIS and subsequently investigated with HAXPES. The Si 2s, Mo 3d, O 1s, B 1s and C 1s peaks were measured using a Si (111) double crystal monochromator and an incident photon energy of 2010 and 4020 eV.

4.4.2. Results

Figure 4.4 shows the Si 2s, Mo 3d, B 1s and C 1s peaks taken from the *as deposited* sample ($t_{B4C} = 1.3$ nm; $\sqrt{t} = 0$ s^{1/2}) and a sample that had been annealed till steady state ($t_{B4C} = 1.3$ nm; $\sqrt{t} = 53$ s^{1/2}), as measured with a photon energy of 2010 eV. The Si 2s peak at 154 eV corresponds to oxidized Si from the native oxide at the sample surface. Because SiO₂ is stable at our annealing temperature [70][†], only the non-oxide silicon peak at 150.5 eV is discussed below. The increase in Mo 3d : Si 2s ratio upon annealing confirms the increased near-surface presence of Mo that resulted from Si diffusing downwards into Mo. Additionally, clear shifts of the Mo 3d_{5/2} (-0.26 eV, in accordance with a MoSi₂-induced shift [76]) and Si 2s peaks (+0.35 eV)

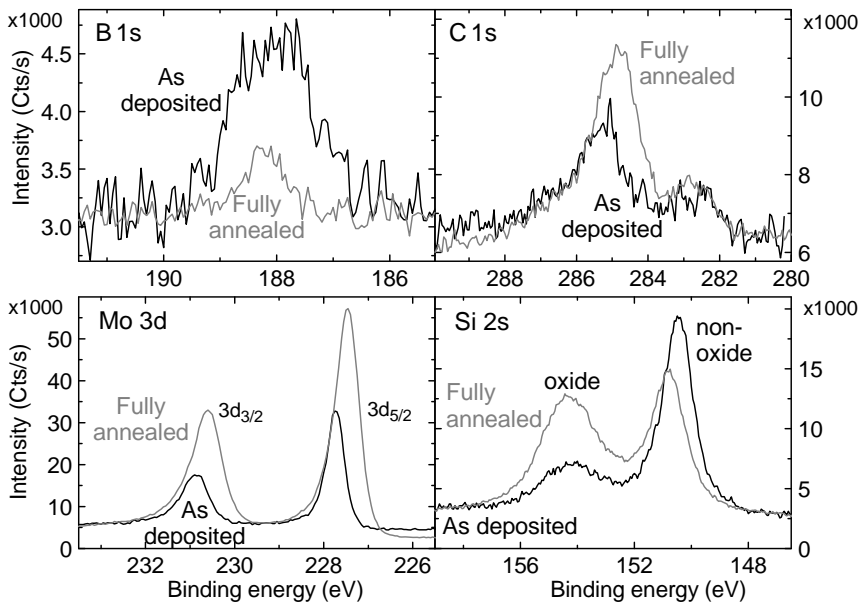


Figure 4.4. The Mo 3d, Si 2s, B 1s and C 1s HAXPES spectra of both the as deposited and the fully annealed ($\sqrt{t} = 53$ s^{1/2}; steady state) sample with 1.3 nm B₄C. All spectra were acquired with a photon energy of 2010 eV.

[†] The Si-oxide peak in Figure 4.4 has actually increased due to the annealing treatment. This is attributed to post-annealing exposure to the ambient. A rougher (see Figure 4.7) and possibly more open structure are probable causes of the increased degree of oxidation.

indicate compound formation. Figure 4.5a presents the evolution of the widths of several peaks, but only marginal changes are observed for the Si 2s and the Mo 3d_{5/2} peak widths. The evolution of the peaks shifts, shown in Figure 4.5b, on the contrary, show that the chemical process of MoSi₂ formation speeds up at the onset of the faster Stage 2.

The C 1s spectrum in Figure 4.4 comprises two peaks: one at 285 eV and the other one at 282.5 eV. Since the C signal at 285 eV is generally associated with (hydrocarbon) contamination at the sample surface, we will only consider the peak at 282.5 eV, which is associated with carbides. As the amount of deposited carbon is very small, changes in the peak width or position of this C 1s peak were below the measurement error. The C

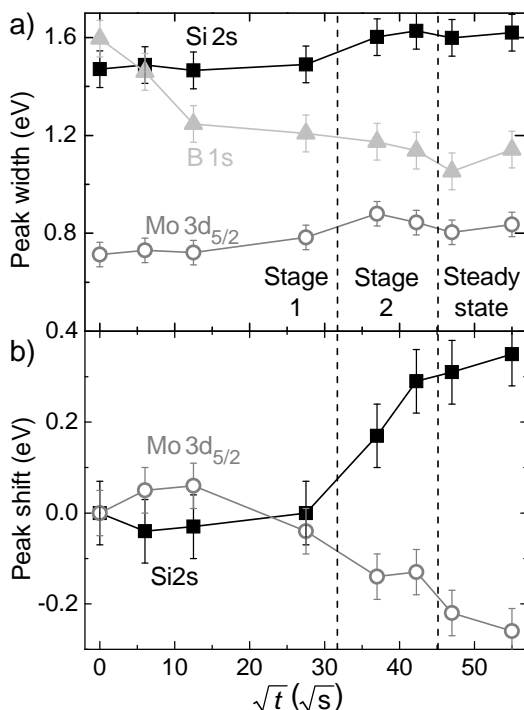


Figure 4.5. (a) The width of the Si 2s, B 1s and Mo 3d_{5/2} peaks of the Mo/1.3 nm B₄C/Si sample as a function of the annealing time. The X-ray energy was 4020 eV. (b) The peak shifts of the Mo 3d_{5/2} and the Si 2s peaks as a function of the annealing time, as measured for the same sample at an X-ray energy of 2010 eV. The dashed lines indicate the times for which changes in diffusion rate were observed with LEIS.

concentration as a function of annealing time though are displayed in Figure 4.6. Since the C concentration does not change within the measurement accuracy, the question remains whether the carbon stayed at the interface or has diffused in both directions: into Si as well as into Mo.

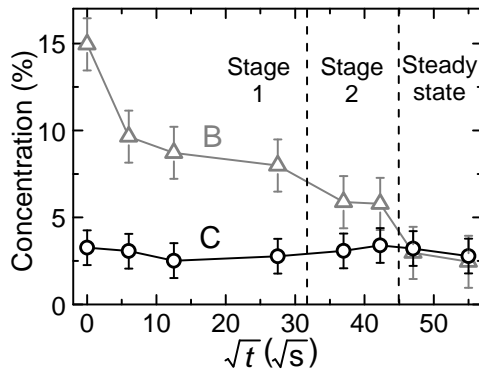


Figure 4.6. The B (triangles) and C (circles) concentrations of the Mo/1.3 nm B₄C/Si sample as a function of the annealing time, as determined from the B 1s and the C 1s (at 282.5 eV) HAXPES peaks, respectively. The measurements are performed at 2010 eV.

Figure 4.4 and Figure 4.6 further show that the B 1s concentration diminished by as much as a factor of 6, thus clearly suggesting that B has diffused downwards, viz. away from Si, towards Mo, evidently forming predominantly MoB_x. After a sharp drop in the beginning of the annealing, the B concentration (Figure 4.6) continued to decrease gradually, therewith strongly suggesting that B first diffused into the Mo layer to form MoB_x, then continued to diffuse downwards. Figure 4.4 and Figure 4.5a show that the B 1s peak has also become narrower, which provides further proof that B is chemically active and that the B₄C decomposes upon annealing. More importantly, the B 1s peak width has reduced to its final width already after $\sqrt{t} = 12 \text{ s}^{1/2}$, indicating that all B₄C has decomposed already by then. In contrast, at the transition point to Stage 2 no significant chemical changes were observed that can explain the acceleration of the diffusion. Hence, a chemical process is excluded as the cause for the acceleration of the diffusion, leaving it to be explained by a change in the morphology.

4.5. Morphology

4.5.1. Experimental details

After ruling out the chemical changes involving B or C at the interface as the cause for the change in diffusion rate, we investigated the evolution of the morphology of the samples and its role in the enhancement of the diffusion rate. A Philips CM300ST-FEG (S)TEM instrument was utilized to analyze several cross-sectional TEM specimens before and after the transition point from Stage 1 to Stage 2 (Figure 4.2). The TEM specimens were prepared according to the procedure described in Ref. [77]. The images were recorded with a magnification of $2.7 \cdot 10^5$ and an acceleration voltage of 300 kV.

4.5.2. Results

Figure 4.7 displays TEM images of samples with $d_{B_4C} = 1.3$ nm in various diffusion states ($\sqrt{t} = 0, 27, 37$ and 53 s^{1/2}, respectively). Amorphous Si and polycrystalline Mo layers were observed in all the structures regardless of their annealing state. Note that the contrast of the B₄C layer is too small to be visible in the TEM images. Before annealing, the layers were smooth and uniform. After annealing ($\sqrt{t} = 53$ s^{1/2}), however, a polycrystalline MoSi₂ layer has developed, as well as layer thickness variations of as much as 4 nm.

The transition from diffusion Stage 1 to the faster Stage 2 occurs at $\sqrt{t} = 32$ s^{1/2}, i.e. in between Figure 4.7(b) and (c). A clear change in the morphology of the interface is observed exactly at that point: the interface was amorphous before the transition, while crystallites of 10-15 by 3 nm are seen afterwards. The concurrence of the crystallization and the transition to Stage 2 confirms that crystallization at the interfaces is the cause of the abrupt increase in diffusion speed: when the amorphous structure turned polycrystalline, grain boundaries were created and these imperfections are known to act as preferential pathways and accelerators for diffusion [78]. Moreover, grain boundary diffusion is presumably also the cause of the development of layer thickness variations, as it is an inhomogeneous process by nature.

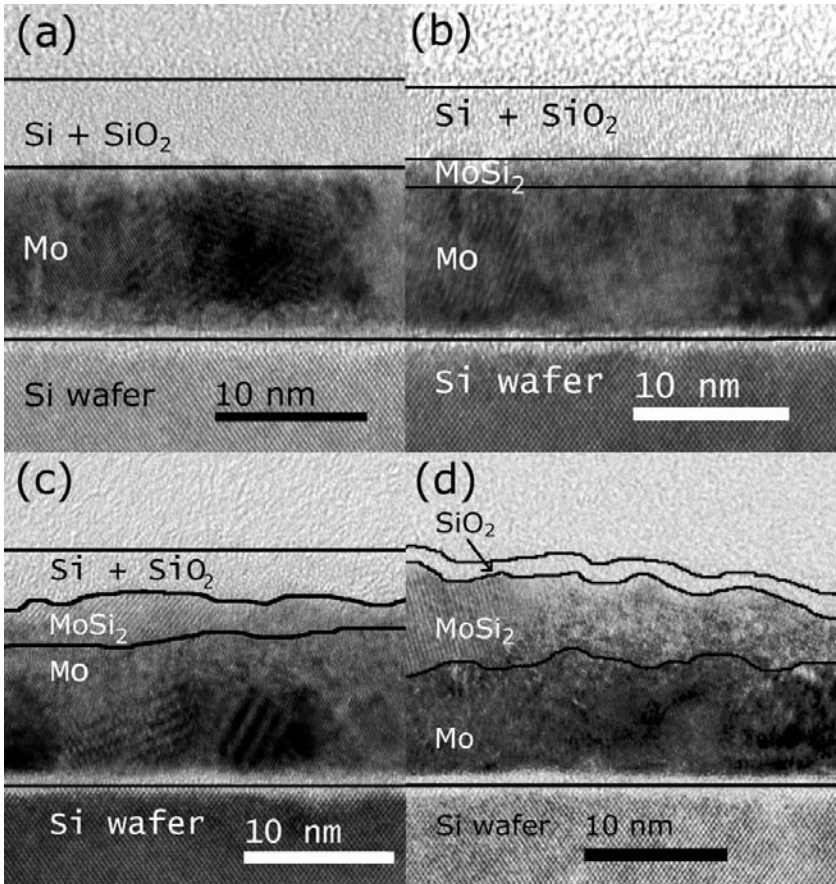


Figure 4.7. TEM images of Mo/1.3 nm B₄C/Si samples in different annealing states. (a) $\sqrt{t} = 0 \text{ s}^{1/2}$; (b) $\sqrt{t} = 27 \text{ s}^{1/2}$; (c) $\sqrt{t} = 37 \text{ s}^{1/2}$ and (d) $\sqrt{t} = 53 \text{ s}^{1/2}$. The contrast of the B₄C layer with the Si is too small to be visible in the TEM images. The SiO₂ is not distinguishable from the Si layer and is therefore only indicated separately in d), where the Si layer has been completely consumed by MoSi₂ formation.

Recalling the decomposition of B₄C at an early stage and the dependence of the transition point on d_{B_4C} , we conclude that, at 500 °C, the barrier function of B₄C mainly lies in B and/or C retarding the crystallization of MoSi₂. A similar action has been reported in Ref. [79]. The linear decrease of D_{Stage2} with increasing d_{B_4C} in Figure 2 further indicates that, *after* the crystallization, the diffusion rate is decreased by B and/or C. No such dependence is

observed *before* the crystallization, which suggests that the crystallite size, and consequently D , is affected by the B or C concentration.

4.6. Conclusions

In conclusion, we have studied diffusion in Mo/B₄C/Si trilayer thin film systems with sub-nanometer resolution to investigate the effect of the amorphous-to-nanocrystalline transition on the diffusion rate. We found that the diffusion occurred in two distinct stages before reaching a steady state. Stage 1 is characterized by relatively slow, linear diffusion, while Stage 2 is marked by an increased diffusion rate. The appearance of nanocrystalline regions at the interfaces proves that the increased diffusion rate is directly caused by the amorphous-to-nanocrystalline transition followed by enhanced diffusion along the grain boundaries of the crystallites. It was excluded that decomposition of the B₄C barrier and formation of molybdenum boride caused the enhanced diffusion. The B₄C interlayer increases the duration of Stage 1, due to B and/or C acting as crystallization-retarding agents. Stage 2 ends when all available Si has been transformed into the silicide, and a steady state is reached.

4.7. Acknowledgments

This work is part of the FOM Industrial Partnership Programme I10 ('XMO') which is carried out under contract with Carl Zeiss SMT AG, Oberkochen and the 'Stichting voor Fundamenteel Onderzoek der Materie (FOM)', the latter being financially supported by the 'Nederlandse Organisatie voor Wetenschappelijk Onderzoek (NWO)'. The HAXPES measurements were supported by the European Community - Research Infrastructure Action under the FP6 "Structuring the European Research Area" Programme (through the Integrated Infrastructure Initiative" Integrating Activity on Synchrotron and Free Electron Laser Science - Contract R II 3-CT-2004-506008).

5. Chemical interaction of B₄C with Mo/Si layered structures

5.1. Abstract

To enhance the thermal stability, B₄C diffusion barrier layers are often added to Mo/Si multilayer structures for extreme ultraviolet optics. Knowledge about the chemical interaction between B₄C and Mo or Si however is largely lacking. Therefore, the chemical processes during annealing up to 600°C of a Mo/B₄C/Si layered structure have been investigated *in situ* with Hard X-ray Photoelectron Spectroscopy and *ex situ* with depth profiling X-ray Photoelectron Spectroscopy. Mo/B/Si and Mo/C/Si structures have also been analyzed as reference systems. The chemical processes in these systems have been identified, with two stages being distinguished. In the first stage, B and C diffuse and react predominantly with Mo. MoSi_x forms in the second stage. If the diffusion barrier consists of C or B₄C, a compound forms that is stable up to the maximum probed temperature and annealing time. We suggest that the diffusion barrier function of B₄C interlayers as reported in literature can be caused by the stability of the formed compound, rather than by the stability of B₄C itself.

5.2. Introduction

As a result of the ongoing quest to produce smaller features, the area of application of extreme ultraviolet (EUV, $\lambda = 13.5$ nm) photolithography has expanded in recent years. The viability of EUV technology relies on Mo/Si multilayer reflective optics whose degradation over the desired life-time of the device is sufficiently low to not impede its operation. Especially under the thermal load induced by the 92 eV EUV radiation, Mo and Si interdiffuse and form molybdenum silicide compounds. This process alters the period of the multilayer mirror, thus causing a mismatch of the incident radiation and the period thickness. The compound formation furthermore reduces the optical contrast between the layers, therewith decreasing the reflectivity. Especially for many-component optical systems, such as used in EUV lithography, small

losses in reflectivity have a major and detrimental impact on the throughput of the equipment.

The degradation of the multilayer optics can be mitigated by the introduction of diffusion barrier layers, such as Si₃N₄, B₄C, and Mo₂C (see, e.g., [3, 4, 80]). Literature mostly considers B₄C, describing its effectiveness to increase the stability of the structure without compromising the reflectivity. The previous Chapter concludes that B₄C is chemically reactive with the adjacent Mo and Si layers, without identifying the exact process. Hence, as a logical follow-up, this Chapter focuses on the so far largely unknown chemical processes that occur in B₄C-barriered Mo/Si layered structures. This work also addresses another question arising in this framework, namely how the chemical behavior of the compound B₄C compares to its constituents B and C in elemental form.

5.3. Experimental Details

Samples consisting of 10.0 nm Mo / 2.0 nm *db* / 5.5 nm Si were deposited onto natively oxidized, super-polished Si substrates, where Si is the terminating layer and *db* denotes B, C, or B₄C. Electron beam evaporation was the deposition method of our choice because of the low energy of the particles (~0.1-0.2 eV), thus avoiding particle induced intermixing. Krypton ion beam assistance (beam voltage 80 V, flux $7 \cdot 10^{13} \text{ cm}^{-2} \text{ s}^{-1}$, angle of incidence 45 degrees) prevented the build-up of roughness and porosity. The ion beam was switched off during the deposition of the first 1.0 nm of each layer in order to prevent ion induced intermixing at the interfaces. The deposition rate was controlled using a set of 4 quartz crystal microbalances and fixed at 20 pm/s for Mo, B, C and B₄C, and 30 pm/s for Si. The base pressure was lower than $1.5 \cdot 10^{-8}$ mbar.

The chemical interaction in the samples during annealing was investigated with Hard X-ray Photoelectron Spectroscopy (HAXPES). The higher kinetic energy of photoelectrons in HAXPES with respect to conventional X-ray Photoelectron Spectroscopy (XPS) increases the mean free path of the photoelectrons. The thus enhanced sampling depth makes HAXPES an especially suitable technique for the investigation of buried interfaces. Moreover, the non-invasive character of HAXPES allows monitoring chemical and compositional changes in real-time.

The energy of the incident X-ray radiation used, 2010 eV, results in an attenuation length of 3.7 nm in Si (compare to 2.8 nm for Al K_α radiation) [81], which is sufficient to probe the interface region in the samples. The HAXPES measurements were conducted in real-time during the annealing treatment at the KMC-1 beamline at BESSY II, equipped with the HIKE experimental station. Extensive descriptions of the beamline and the experimental station are given in [75] and [74], respectively.

The annealing temperature T was in the 400-600 °C range, and was adjusted for each sample individually in order to resolve the different processes. Compound formation is judged by changes in binding energy E_{bin} and relative intensity of the photoelectron peaks corresponding to the various elements. Its small cross-section for photoelectric absorption causes a relatively low signal-to-noise ratio for carbon. Consequently, carbon binding energy shifts were below the measurement accuracy, and are, therefore, not reported here. The components of the various photoelectron peaks are listed in Table 5.1, along with the compounds with which they are generally associated. The oxygen signal is not discussed in this Chapter because, in accordance with the reported stability of SiO₂ in the probed temperature range [70], no changes in the O 1s signal or the oxide-related Si 2s peak (at 154.3 eV) were observed. Moreover, no signs of oxidation of Mo, B or C were found.

Table 5.1. Overview of the components and associations of the various photoelectron peaks.

Element	Transition	E_{bin} (eV)	Association	Referred to as
Si	2s	150.6	non-oxide, non-carbide	Si _{elem}
		152.4	carbide, sub-oxide	Si _{carb} /Si _{sub-ox}
		154.3	oxide	Si _{oxide}
Mo	3d _{5/2}	227.8	non-oxide	Mo 3d _{5/2}
		230.9	non-oxide	Mo 3d _{3/2}
B	1s	188.2	non-oxide	B
C	1s	282.6	carbide	C _{carbide}
		284.2	α -C	C _{amorphous}

The (time-resolved) HAXPES measurements were complemented with depth-resolved information that was obtained by conventional XPS sputter depth profiling. A Theta Probe instrument and Al K_α radiation ($h\nu = 1486.6$ eV) were used for these measurements. Sputter erosion was conducted with 0.5 keV Ar⁺ at an angle of 45° with respect to the sample surface. Binding energy shifts and the splitting of peaks in various components were disregarded since compound formation may be caused by the sputter erosion treatment. All samples were analyzed with XPS sputter depth profiling before and after the annealing treatment.

5.4. Results

The results will be discussed per interlayer material. Starting with the comparatively simple, ternary systems Mo/B/Si and Mo/C/Si, we will conclude with the more complex Mo/B₄C/Si sample. The differences and similarities between the three systems are discussed in the Discussion section.

5.4.1. Mo/B/Si

The HAXPES results of annealing the 10.0 nm Mo / 2.0 nm B / 5.5 nm Si structure are displayed as a function of the annealing time t in Figure 5.1. In view of the absence of C in the structure, the Si_{carb}/Si_{sub-ox} component is obviously to be fully attributed to silicon sub-oxide and is only shown for completeness and as a reference for the Mo/C/Si and Mo/B₄C/Si samples. In line with the expected stability of silicon oxide, the Si_{carb}/Si_{sub-ox} concentration does not change significantly and will, therefore, not be further discussed for this sample. Figure 5.1 shows that the interaction occurs in two stages: the first stage lasting from approximately $t = 0:40 - 2:20$ and the second stage from $t = 2:20 - 3:00$. In the first stage, the B concentration decreases (Figure 5.1a), while both the B 1s E_{bin} and the Mo 3d_{5/2} E_{bin} increase (Figure 5.1b). Clearly, the B diffuses predominantly away from the surface, towards the Mo layer, and forms molybdenum boride. In addition, the graph shows a simultaneous decrease of the Si_{elem} 2s E_{bin} , indicating chemical changes of Si as well. Since the decreasing B concentration indicates that the B diffuses predominantly into the Mo layer, only minor amounts of SiB_x could be formed. Alternatively, the shift of the Si E_{bin} could be caused by decomposition of a SiB_x interfacial layer that had possibly already formed before the start of the annealing treatment.

The second stage sets in when the temperature is increased from 500 to 550 °C at $t = 2:20$. The further decrease of the B concentration indicates diffusion of B further into the Mo layer. Most probably due to a changing stoichiometry of the MoB_x, the B E_{bin} continues to shift positively. Furthermore, the Si concentration drops sharply while the Mo concentration rises. At the same time, the Si_{elem} E_{bin} rises by 0.45 eV while the Mo E_{bin} decreases by 0.25 eV. These changes are a clear signature of molybdenum silicide formation. Literature about similar systems reports that out of the several possible molybdenum silicides, it is (at least predominantly) MoSi₂ that is formed [61, 62]. The observed binding energy shifts are in accordance with reported, experimentally determined values [76, 82].

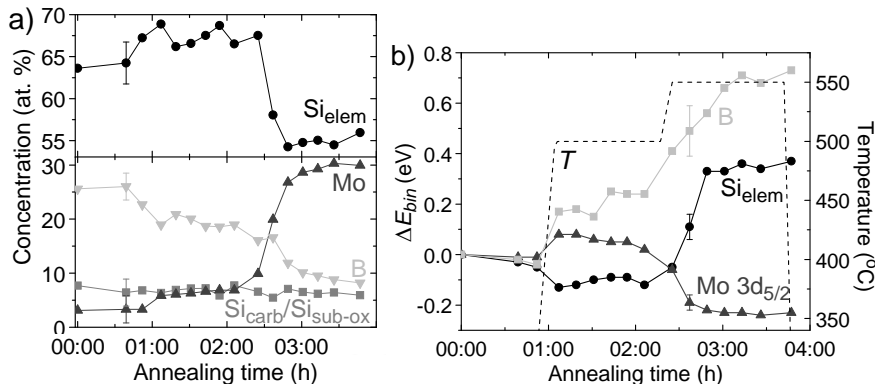


Figure 5.1. The HAXPES results of the 10.0 nm Mo / 2.0 nm B / 5.5 nm Si sample as a function of the annealing time. a) The Si, B and Mo concentrations, as derived from the relative peak intensities. b) The binding energy shifts of the B, Si_{elem} and Mo peaks. The shifts are calculated with respect to the binding energy at $t = 0$. The dashed line indicates the temperature profile.

The concentration profiles as determined with XPS sputter depth profiling before and after annealing are displayed in Figure 5.2. The concentration profile of the sample before annealing (Figure 5.2a) serves as a reference for the interpretation of the results after the annealing treatment. It shows the deposited structure: Si on B on Mo, on top of the Si substrate. The concentration profiles after annealing (Figure 5.2b) confirm the previous conclusions: both B and Si have diffused into the Mo layer. Moreover, it is

visible that the structure is not homogeneous, but that the MoSi_x layer has formed on top of the MoB_x layer.

The formation of MoSi_x and MoB_x (and not SiB_x) can be explained using the formation enthalpies listed in Table 5.2: it is energetically unfavorable to form SiB_x, because SiB_x has a comparatively small enthalpy of formation ΔH_{form} . Moreover, Si and B are available in smaller quantities than Mo, meaning that SiB_x formation would go at the cost of both MoSi_x and MoB_x formation. Furthermore, the segregation of the MoB_x and MoSi_x in two layers can be attributed to the low solubility of B in MoSi_x [83], and the large interfacial energy associated with a possible eutectic structure. As for the sequence of the two layers: for a MoSi_x on MoB_x structure, the travel distance for Si would be relatively small, because it does not have to travel through the MoB_x layer in order to reach the Mo underneath. In combination with the larger mobility of B with respect to Si[†], this would cause B rather than Si to diffuse deeper into the Mo layer while MoSi_x forms at the Si/MoB_x interface. This leads to a MoSi_x on MoB_x structure, which is fully in line with the observations.

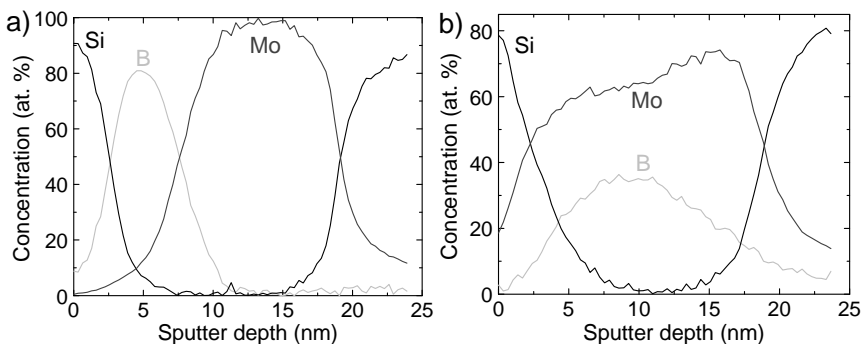


Figure 5.2. XPS sputter depth profiles of the 10.0 nm Mo / 2.0 nm B / 5.5 nm Si sample (a) before and (b) after the annealing treatment at the HAXPES facility. Note that the scale of the horizontal axis is indicative only: the erosion rate is calculated from the ion fluence assuming a constant sputter yield. The dependency of the sputter yield on the composition of the surface is not taken into account.

[†] The larger mobility of B with respect to Si is apparent from the fact that B diffuses at a lower T than Si.

Table 5.2. Literature values for the formation enthalpies ΔH_{form} of relevant compounds.

	ΔH_{form} at 298 °K (kJ/mole atoms)	Reference
B ₄ C	-11	[84]
Mo ₂ C	-16	[85]
SiB ₃	-23	[86]
Mo ₃ Si	-29	[87]
SiC	-36	[87]
Mo ₅ Si ₃	-39	[87]
MoSi ₂	-44	[87]
Mo ₂ B ₅	-54	[85]
MoB ₂	-57	[85]
MoB	-62	[85]

5.4.2. Mo/C/Si

Figure 5.3 displays the HAXPES results of annealing the sample with 10.0 nm Mo / 2.0 nm C / 5.5 nm Si. The graphs show that the interaction in this sample also occurs in two stages: the first stage lasts from approximately $t = 0:50 - 5:00$ and the second stage from $t = 5:00 - 7:00$. In the first stage, the concentration of C_{carbide} rises at the cost of C_{amorphous} (Figure 5.3a), while the Mo E_{bin} increases (Figure 5.3b). This indicates that C diffuses away from the surface, i.e. towards the Mo layer, and forms molybdenum carbide. The positive shift of the Mo E_{bin} is in agreement with the findings of Brainard *et al.* [76]. There are no indications for chemical processes involving Si, since neither its concentration (Si_{elem} nor Si_{carb}/Si_{sub-ox}), nor its binding energy changes significantly. Moreover, the Si_{carb}/Si_{sub-ox} concentration is the same as in the sample with B interlayer, indicating that it can be fully attributed to silicon suboxide, and does not point towards the presence or formation of silicon carbide.

The second stage sets in when the temperature is increased to 600 °C. Together with the E_{bin} shifts of Mo and Si_{elem}, the rise of the Mo concentration and the decrease of the Si_{elem} concentration indicate MoSi_x formation. Rather surprisingly, the concentrations of Si_{carbide} and C_{carbide}

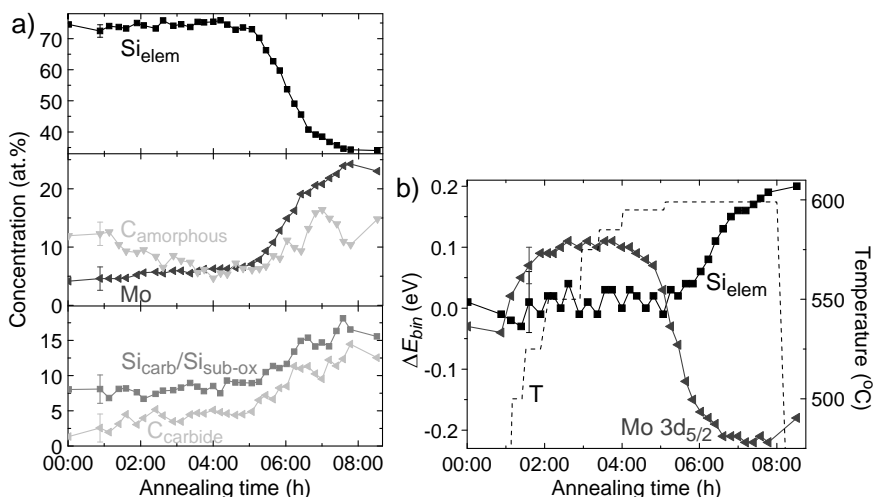


Figure 5.3. The HAXPES results of the 10.0 nm Mo / 2.0 nm C / 5.5 nm Si sample as a function of the annealing time. a) The Si, C and Mo concentrations, as derived from the relative peak intensities. b) The binding energy shifts of the Si_{elem} and Mo peaks. The shifts are calculated with respect to the same binding energies as in Figure 5.1b. The dashed line indicates the temperature profile.

increase at the same time, indicating that SiC_x forms, or that an already formed SiC_x comes closer to the surface, because elemental Si diffuses deeper in the structure.

The results of the sputter depth profiling analysis of the sample before and after the annealing treatment are shown in Figure 5.4. The concentration profile of the sample before annealing serves as a reference for the interpretation of the results after the annealing treatment. Before annealing (Figure 5.4a), the graph shows the deposited structure: Si on C on Mo, on top of the Si substrate. After annealing (Figure 5.4b), a SiC_x layer is visible on top of MoSi₂ on top of MoC_x. Combining this with the HAXPES results, we can conclude that, besides MoC_x, SiC_x formed at the interface, either during the deposition or in the course of the annealing. Apparently, this SiC_x is stable and, in stage 2, the elemental Si diffuses *through* this compound to form MoSi₂, leaving SiC_x near the surface of the sample.

The formation of SiC and MoSi₂ can be explained using the thermodynamic data listed in Table 5.2: for the available amounts of material, MoSi₂ and SiC formation are favorable over Mo₂C formation. However, we observed that the

majority of the C bonds to Mo rather than to Si. We can explain this by assuming that SiC is not permeable to C once it reaches a certain thickness. Therefore, only part of the C is able to form SiC. The remainder of the C would then react with Mo, the only other element available. In stage 2, Si diffuses through SiC, so that MoSi₂ can be formed and Mo₂C segregates towards the wafer. Note that the observed stability of SiC_x in contact with MoSi_x is in accordance with the results of Amrani *et al.* [88] and Boettinger *et al.* [89], who report that SiC in contact with MoSi₂ is stable at 1200 °C and 1600 °C, respectively.

Figure 5.4b further shows that the MoSi_x and MoC_x have segregated in separate layers. This segregation has also been observed in [90], and can be attributed to the same causes as the segregation of MoB_x in the previously discussed sample: a large interfacial energy associated with a possible eutectic structure, and, presumably, a low solubility of C in MoSi_x / Si in MoC_x. Finding MoSi_x on top of MoC_x and not vice versa is presumably caused by the fact that Si needs to travel a smaller distance. In combination with the higher mobility of C compared to Si, this causes C rather than Si to diffuse deeper into the Mo layer when MoSi_x forms at the Si/MoC_x interface.

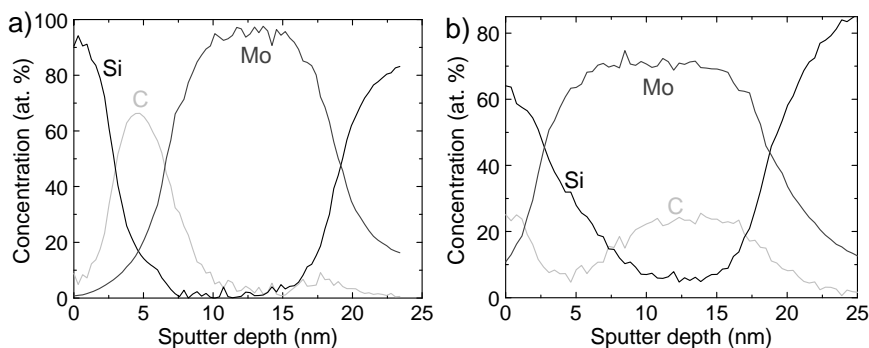


Figure 5.4. XPS sputter depth profiles of the 10.0 nm Mo / 2.0 nm C / 5.5 nm Si sample (a) before and (b) after the annealing treatment at the HAXPES facility. Note that the scale of the horizontal axis is indicative only: the erosion rate is calculated from the ion fluence assuming a constant sputter yield. The dependency of the sputter yield on the composition of the surface is not taken into account.

5.4.3. Mo/B₄C/Si

Figure 5.5 displays the HAXPES results of annealing the sample with 10.0 nm Mo / 2.0 nm B₄C / 5.5 nm Si. The graphs show that also in this structure the interaction occurs in two stages: the first stage lasts from approximately $t = 0:30 - 3:40$ and the second stage from $t = 3:40 - 5:00$. Note that because B is in a compound instead of in its elemental form, the B E_{bin} is high compared to the Mo/B/Si sample at $t = 0$.

The changes in the first stage are small. Nevertheless, the gradual decrease of the B concentration and the gradual increase of the Mo concentration (Figure 5.5a) are significant and suggest that B diffuses away from the surface, into the Mo layer, thus forming MoB_x. This is supported by the positive shift of the Mo E_{bin} (Figure 5.5b), although it may also be (partially) caused by MoC_x formation. The B E_{bin} does not change significantly, while the results from the Si/B/Mo sample indicate that MoB_x formation should reduce the shift to 0.2 eV. This is due to the fact that the majority of the B signal does not stem from the B that diffused into the Mo, but from B that remained at the interface. We will show below that this B is still bond to C, which explains why the B E_{bin} still corresponds to that of B in B₄C. Because no E_{bin} reference values are available, we cannot, at this point, conclude whether it concerns a pure B_xC compound or rather a SiB_xC_y compound.

Finally, the decrease of the Si E_{bin} in stage 1 is inconclusive as it suggests either SiB_x formation in a small quantity or decomposition (see Mo/B/Si section). Neither the Si_{carb}/Si_{sub-ox} nor the C_{carbide} concentration profile reveals signs of SiC_x formation. We remark that it is very well possible that ternary compounds like MoB_xC_y and SiB_xC_y formed besides these binary compounds. However, they cannot be identified through their binding energy shifts because no reference values are available.

The second stage sets in at $t = 3:40$, when the temperature is increased to 570 °C. The E_{bin} shifts of Mo and Si_{elem}, the rise of the Mo concentration and the decrease of the Si_{elem} concentration together indicate MoSi_x formation. Moreover, the concentrations of both C_{carbide} and B increase at the same time, indicating that boron carbide comes closer to the surface. Furthermore, it is apparent from the reduction of the B:C ratio by a factor of 2 between $t = 3:40$ and $t = 4:30$ that the boron carbide has become poorer in B. However, the B E_{bin} does not shift significantly, which suggests that the probed B is not

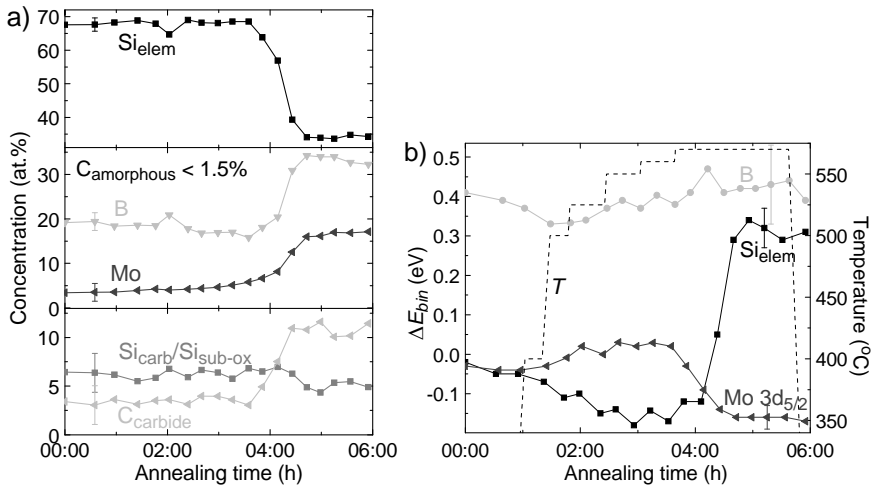


Figure 5.5. The HAXPES results of the 10.0 nm Mo / 2.0 nm B₄C / 5.5 nm Si sample as a function of the annealing time. a) The Si, B, C and Mo concentrations, as derived from the relative peak intensities. b) The binding energy shifts of the B, Si_{elem} and Mo peaks. The shifts are calculated with respect to the same binding energies as in Figure 5.1b. The dashed line indicates the temperature profile.

present in MoB_x or MoSi_xB_y, but in SiB_xC_y or perhaps still in a remaining part of boron carbide. This indicates that Si diffuses through the remainder of the boron carbide or SiB_xC_y layer at the interface to form MoSi_x, thus enhancing the B and C signal intensities by bringing the boron carbide or SiB_xC_y layer closer to the surface.

The results of the sputter depth profiling analysis of the sample before and after the annealing treatment are shown in Figure 5.6. Before annealing (Figure 5.6a), the graph shows the deposited structure: Si on B₄C on Mo, on top of the Si substrate. After annealing (Figure 5.6b), a SiB_xC_y layer is visible on top of MoSi_x (or possibly MoSi_xB_y) on MoB_xC_y. The latter becomes poorer in B and richer in C towards the substrate and may even consist of separate layers of MoB_x and MoC_x.

Since the HAXPES results in Figure 5.5 indicate a B_xC or SiB_xC_y layer close to the surface after annealing, it is plausible that the B has split into two parts. One part remained B_xC or formed SiB_xC_y, while the other part diffused into Mo during the first stage and segregated towards the substrate in the second stage. In order to verify the chemical state of B after annealing at different

depths, we split the B peak in the XPS depth profile into two components, each with fixed E_{bin} : B₊ at 188.7 eV and B₋ at 187.7 eV. The result is shown in Figure 5.7. Note that the extent to which the results are affected by the sputter-induced intermixing artefacts are unknown. Nevertheless, Figure 5.7 clearly supports the hypothesis of the split B distribution suggested by the HAXPES results: a B₊ distribution is found close to the surface, and can be associated with B_xC or SiB_xC_y. The B₋ distribution on the other hand is located deeper in the sample, below the MoSi_x layer, and is hence associated with MoB_x.

Combining the depth-profiling results with the HAXPES results, we can conclude that, besides MoB_xC_y (or MoB_x plus MoC_x), B_xC and/or SiB_xC_y formed at the interface. The latter compound is stable, and in the second stage the elemental Si diffuses *through* this compound to form MoSi₂, leaving B_xC and/or SiB_xC_y near the surface of the sample. Furthermore, the mobility of B and C is larger than that of Si, which causes segregation of MoB_xC_y (or MoB_x plus MoC_x) when MoSi_x forms at the interface.

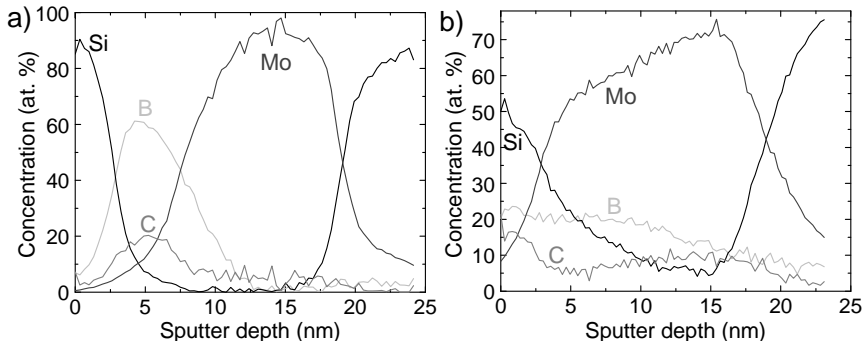


Figure 5.6. XPS sputter depth profiles of the 10.0 nm Mo / 2.0 nm B₄C / 5.5 nm Si sample (a) before and (b) after the annealing treatment at the HAXPES facility. Note that the scale of the horizontal axis is indicative only: the erosion rate is calculated from the ion fluence assuming a constant sputter yield. The dependency of the sputter yield on the composition of the surface is not taken into account.

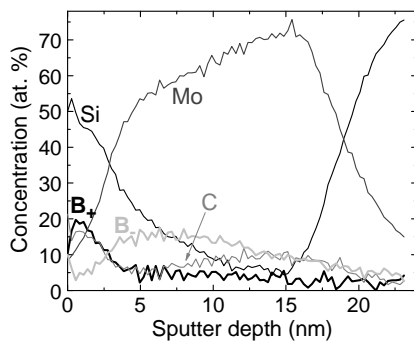


Figure 5.7. XPS sputter depth profiles of the 10.0 nm Mo / 2.0 nm B₄C / 5.5 nm Si sample after the annealing treatment at the HAXPES facility. Figure 5.7 is identical to Figure 5.6b, except that the B peak is now split into two components, where B₊ can be associated with B_xC/SiB_xC_y, and B₋ with MoB_x/MoB_xC_y.

5.5. Discussion

After the description and identification of the processes that occur in the investigated samples, this section focuses on the comparison between the interaction of B, C and B₄C interlayers with Mo and Si.

In all three systems, the first interaction to occur is that of the interlayer with Mo and, to a lesser extent, with Si. Another process the systems have in common is the formation of MoSi_x with *x* close to 2, and the segregation of MoB_x/MoC_x that it induces. A major difference between the samples with elemental C and B barriers is that only in the former case a stable compound (SiC_x) is formed, through which Si diffuses to form MoSi_x in the second stage. No indications were observed that C behaves differently in the presence of B: both in the C and in the B₄C sample, C partially diffuses into the Mo and partially into Si, where it forms a stable compound. The behavior of B, on the contrary, is obviously affected by the presence of C: in the Mo/B₄C/Si system, only part of the B (B₋ in Figure 5.7), behaves similar to B in the Mo/B/Si system and forms MoB_x. The other part though (B₊ in Figure 5.7) remains bonded to C and is encountered close to the surface after the annealing treatment. It answers the question posed in the introductory section, whether the interaction of B₄C is fundamentally different from that of B or C with Mo and Si: the compounds formed with involvement of C are significantly more stable. This difference is likely to make the barrier

functionality of B interlayers inferior to that of C or B₄C interlayers. Therefore, we suggest here that the diffusion barrier function of B₄C interlayers as reported in literature can be caused by the stability of the formed boron-poor B_xC/SiB_xC_y layer, rather than the stability of the B₄C layer itself. In fact, this layer most probably consists of SiB_xC_y rather than B_xC, as it is unlikely that off-stoichiometric B_xC is more stable than stoichiometric B₄C.

We performed simulations to investigate whether the SiB_xC_y compound may have formed due to the 80 eV krypton ion bombardment during the deposition of the Si layer onto the C / B₄C layer. The penetration depth of these ions was evaluated via molecular dynamics simulations of the effect of bombarding amorphous silicon with 400 Kr atoms. The Kr atoms had a kinetic energy of 80 eV and the sample consisted of a 8.1 x 8.1 nm² Si (001) crystal with an amorphous top layer of 3.0 nm thick. See Ref. [91] for extensive details about the sample structure and the Si and Si-Kr potentials. The temperature was 27 °C and the interval between two impacts was 7.1 ps. As during the real deposition, the polar angle of incidence was 45 degrees, with random azimuth. The main result of these simulations is that the penetration depth of the ions was 0.73 nm with a root-mean-square variation of 0.3 nm. This makes the ion bombardment unlikely as a cause of the SiB_xC_y compound formation, since the ion bombardment only started at a Si layer thickness of 1.0 nm. Hence, we can conclude that the SiB_xC_y formed spontaneously, either during deposition or during the first stage of the annealing treatment.

Lastly, we want to remark that the results of experiments with a reverse layer sequence (i.e. Si/interlayer/Mo instead of Mo/interlayer/Si) are consistent with the above mentioned conclusions: depth profiling of annealed Si/C/Mo and Si/B₄C/Mo structures showed split C/B profiles, while B was only observed in the Mo layer after annealing of a Si/B/Mo sample.

5.6. Conclusions

The chemical processes occurring in Mo/B/Si, Mo/C/Si, and Mo/B₄C/Si layered structures upon annealing up to 600 °C have been identified using XPS depth profiling and *in situ* HAXPES. The first process to take place is B (resp. C) diffusing into Mo to form predominantly MoB_x (resp. MoC_x and MoB_xC_y). In addition, possibly small amounts of SiB_x (resp. SiC_x and

SiB_xC_y) are formed. Subsequently, upon raising the annealing temperature, Si is able to diffuse towards Mo. The already formed MoB_x (resp. MoC_x and MoB_xC_y) decomposes in favor of MoSi_x formation. The released B (resp. C) diffuses further forming MoB_x (resp. MoC_x and MoB_xC_y) deeper into the Mo layer. Only when the barrier layer contains C, the barrier layer material forms a compound (SiC_x resp. SiB_xC_y) that is stable up to the maximum probed temperature and annealing time. We suggest that in view of the stability of the SiB_xC_y layer, the diffusion barrier function of B₄C interlayers as reported in literature can be caused by the stability of the formed SiB_xC_y layer, rather than the stability of the B₄C layer itself. In the second stage, Si diffuses through the compound layer to form MoSi_x. In this sense, the interaction of B₄C with Mo and Si is similar to C rather than to B.

5.7. Acknowledgments

This work is part of the FOM Industrial Partnership Programme I10 ('XMO') which is carried out under contract with Carl Zeiss SMT AG, Oberkochen and the 'Stichting voor Fundamenteel Onderzoek der Materie (FOM)', the latter being financially supported by the 'Nederlandse Organisatie voor Wetenschappelijk Onderzoek (NWO)'. The HAXPES research leading to these results have received funding from the European Community's Seventh Framework Programme (FP7/2007-2013) under grant agreement n° 226716.

6. Reduction of interlayer thickness by low-temperature deposition of Mo/Si multilayer mirrors for X-ray reflection

6.1. Abstract

Thin interlayers are essential for high-quality multilayer optics. We present the first investigation of using low temperature deposition to reduce the interlayer thickness of Mo/Si multilayer structures. Even after warming up to room temperature prior to analysis, the interlayers that formed upon cryogenic deposition were found to be approximately 60% thinner compared to room temperature deposition. The thickness reduction at low temperature and its preservation upon warming up are attributed to a lower mobility of adatoms, reduced surface segregation of Si during Mo-on-Si growth, and/or crystallization of Mo. When combined with ion bombardment, low temperature deposition of multilayer structures is expected to have a beneficial effect on the reflectivity of multilayer optics.

6.2. Introduction

Nanophysics and nanotechnology are more ubiquitous than ever. With continuously decreasing feature sizes and layer thicknesses, control of interface properties at the sub-nanometer scale has become of paramount importance. Multilayer reflective X-ray optics are a telling example. The functioning of these Bragg reflectors relies on smooth interfaces, because roughness reduces the specularly reflected intensity by causing diffuse scattering and layer thickness variations. Thin interfacial layers of mixed composition (interlayers) are essential too, as interlayers decrease the optical contrast between the layers, thus also reducing the reflectance. The interlayer formation and the associated reflectance loss can be reduced by inserting diffusion barrier layers, but the non-ideal optical constants of the barrier materials cause reflectance losses themselves [3, 92]. An alternative way, investigated in this paper, is to mitigate the interlayer formation itself by decreasing the chance of atoms to overcome the activation energy barrier for

diffusion and compound formation, which can be done by temperature reduction during the fabrication of the multilayer mirrors.

This paper focuses on Mo/Si multilayer Bragg reflectors, which are relevant for many optical applications in the 12.5-25 nm wavelength range, including extreme ultraviolet (EUV) lithography, EUV astronomy, and X-ray microscopy. It was chosen as the object of this study because, regardless of the deposition method, a silicide interlayer forms upon deposition [15, 16, 93, 94], driven by the negative enthalpy of interface formation $\Delta H_{Mo\ in\ Si}^{interface} = -126\text{ kJ/mole Mo}$ (at 25°C) [85].

Cryogenic deposition of Mo/Si multilayer structures have been performed by the authors of Refs. [38, 39], who investigated the temperature dependence of the roughness and reflectivity of Mo/Si multilayer mirrors in the -155 to 600 °C range. The mirrors were found to have a lower roughness and a higher reflectivity upon deposition at -155 °C compared to room temperature deposition. However, in those studies no information was obtained on the effect of the cryogenic deposition on the formation of interlayer compounds. This paper, therefore, is the first to focus on the effect on the interlayers of Mo/Si multilayer structures when the kinetics of interlayer formation during the deposition are influenced by cooling the substrate with liquid nitrogen. To minimize the influence of the energy of the deposition flux, electron beam evaporation was selected as the deposition method, as the evaporated particles have a very low energy of 0.1-0.2 eV.

6.3. Experimental details

The deposition setup was equipped with two 10 kV electron beam (e-beam) evaporators that faced upwards to the sample holder, located at a distance of 70 cm. The deposition rate of both Mo and Si was 0.02 nm/s. The layer thickness was monitored and controlled with a quartz crystal microbalance. The base pressure was lower than $3 \cdot 10^{-8}$ mbar. The key feature of the setup was the possibility to fill the hollow substrate holder with liquid nitrogen to cool the substrate. Good thermal contact between the substrate holder and the sample was ensured by the application of silver glue. A cylindrical shield extended from the sample holder (\varnothing 100 mm, length 100 mm). This shield was cooled along with the sample holder and acted as a Meissner trap in the vicinity of the sample, thus minimizing the condensation of background gasses onto the sample. Two batches of three samples were produced by

depositing Mo/Si multilayer structures onto 1" Si wafers. The structures consisted of ten 5.5 nm Si / 3.4 nm Mo bilayers and were Si-terminated. One batch was deposited while the substrate was cooled with liquid nitrogen (the LT sample), while a second one was deposited at room temperature (the RT sample).

X-ray Photoelectron Spectroscopy (XPS) depth profiling with 0.5 keV Ar⁺ at an angle of 45° was used to determine the in-depth concentration profiles of Mo and Si. The analysis was performed with a Thermo Theta Probe instrument. The period thickness of the multilayer mirror (the so-called *d*-spacing) and the crystallinity of the samples were analyzed with an X'Pert Cu K_α reflectometer ($\lambda = 0.154$ nm). Wide Angle X-ray Diffraction scans (WAXRD) were performed to acquire information about the crystallinity of the sample. The angle of incidence ω was fixed at 1.7° grazing in order to maximize the sample illumination area and keep it constant, while the detector scanned from 20 to 150°. The reflectivity of the multilayer structure as a function of the angle of incidence θ was measured during Grazing Incidence X-ray Reflection scans (GIXR, also known as θ -2 θ scans). GIXR spectra were used to determine the *d*-spacing.

The changes in the layered structures as a result of annealing of the samples were analyzed by measuring GIXR spectra upon progressive annealing of the samples. Each annealing step lasted 48 hours and was conducted in a vacuum oven to prevent diffusion of ambient gas into the samples. The samples were cooled down to room temperature before the analysis.

6.4. Results

6.4.1. GIXR and annealing data

GIXR measurements showed that in the as-deposited state, the LT sample exhibited a larger *d*-spacing than the RT sample (9.10 vs. 8.46 nm). Three mechanisms could contribute to this effect: (i) a higher porosity due to the reduced surface diffusion, (ii) deposition of more material due to a higher sticking coefficient, and/or (iii) less interlayer formation and thus less compaction, as 1.0 nm Si plus 0.4 nm Mo is consumed to form only 1.0 nm of MoSi₂. Progressive annealing of the two samples allowed us to quantify the

Table 6.1. The d -spacing and the difference in compaction of the multilayer structures upon progressive annealing.

T (°C)	d -spacing (nm)		difference in compaction (nm)
	LT	RT	
25	9.10	8.46	--
275	8.12	7.56	0.06 ± 0.02
300	7.99	7.40	
325	7.58	6.90	
350	6.97	6.78	0.43 ± 0.02
375	6.98	6.75	

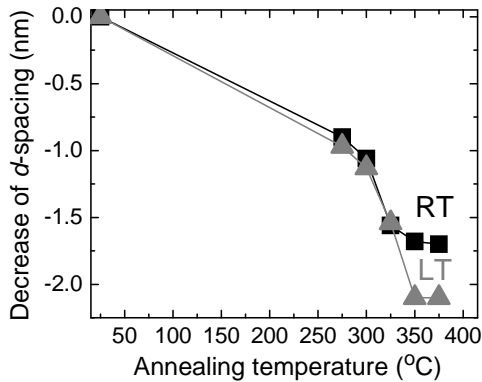


Figure 6.1. The decrease of the d -spacing of the samples as a function of the annealing temperature.

contribution of each of these mechanisms. Table 6.1 lists the d -spacing and the difference in compaction of the two multilayer structures as a function of the annealing temperature, with a graphical representation in Figure 6.1.

The compaction of the Mo/Si multilayered structures is the combined result of interlayer formation and free volume annihilation (porosity reduction). Both of these processes require that the atoms are mobile. Interlayer formation additionally requires overcoming the activation energy for compound formation. Therefore, the minimum temperature needed for

porosity reduction is lower than for interlayer formation. Consequently, the significant compaction of $(11 \pm 1) \%$ upon annealing at $275 \text{ }^\circ\text{C}$ (see Table 1) demonstrates that, at that temperature, the atoms are already sufficiently mobile for porosity reduction. Hence, we assume that all free volume has been annihilated after annealing at $325 \text{ }^\circ\text{C}$. Up to that temperature both samples showed almost the same compaction. Subsequently, the substantial increase of the difference in compaction from 0.06 nm at $275\text{-}325 \text{ }^\circ\text{C}$ to 0.43 nm at $350\text{-}375 \text{ }^\circ\text{C}$ (an increase of 0.37 nm) can be predominantly attributed to more silicide interlayer formation during annealing in the LT sample than in the RT sample.

The sharp decrease of the d-spacing from $300 \text{ }^\circ\text{C}$ to $350 \text{ }^\circ\text{C}$ is caused by a phase transformation to (hexagonal) MoSi_2 , as also observed in [19, 20]. Above $350 \text{ }^\circ\text{C}$, the d-spacing is practically constant because the maximum amount of MoSi_2 has formed already. From the WAXRD measurements (presented and discussed below) it is evident that, after the phase transformation, both samples contain equal amounts of MoSi_2 . Therefore, the fact that annealing at $350\text{-}375 \text{ }^\circ\text{C}$ caused more silicide formation in the LT sample than in the RT sample suggests that less silicide had formed in the LT sample in the as deposited state. Supposing that upon deposition the same type of silicide formed as upon annealing (MoSi_2), this indicates that, as deposited, the interlayers of the LT sample are $(0.9 \pm 0.2) \text{ nm}$ thinner. This result is based on the calculated compaction of the d-spacing due to the formation of MoSi_2 (0.4 nm compaction for every 1.0 nm of MoSi_2). Note that the 1 nm interlayer reduction comprises the total interlayer thickness per period, i.e. the Mo-on-Si plus the Si-on-Mo interlayer. With the typical values cited for the total interlayer width of e-beam deposited multilayered structures being 1.6 nm [93, 94], cryogenic deposition reduced the total interlayer width by approximately 60% .

Finally, Table 6.1 shows that, after the thermal treatment annihilated any differences in d-spacing caused by porosity or interlayer formation, a difference of 0.21 nm remains. This difference is attributed to a higher sticking coefficient of Mo^\dagger caused by the low substrate temperature. Note that the minor difference in deposited Mo amount cannot affect our conclusions.

[†] As discussed below (Section 6.4.3, WAXRD), equal amounts of Si were proven to be deposited in both types of samples.

Figure 6.2 displays measured GIXR curves of both samples in their as deposited state. The obtained reflectance was simulated using IMD software [43]. For the RT sample, the best fit of the first order Bragg peak was obtained using a layer roughness σ of 1.1 nm and MoSi₂ interfaces with a thickness of 1.2 nm (i.e. the total interface thickness per period was 2.4 nm). For the simulation of the LT sample we varied the interlayer thickness, and, therefore, also the amount of Mo and Si consumed by the interfaces. The total amount of Si was kept the same, while 0.21 nm of Mo was added because of the observed higher sticking coefficient at cryogenic temperature. It was found that the interface thickness had to be reduced to 0.8 nm per interface (i.e. 1.6 nm per period) in order to match the position of the first order Bragg peak (solid grey line). Moreover, σ had to be reduced from 1.1 nm to 0.9 nm in order to obtain a better match of reflectance (dashed light grey line). The in this way obtained interlayer reduction of 0.8 nm per period (0.4 nm per interlayer) corresponds very well with the (0.9 ± 0.2) nm interlayer reduction per period found from the compaction upon progressive annealing.

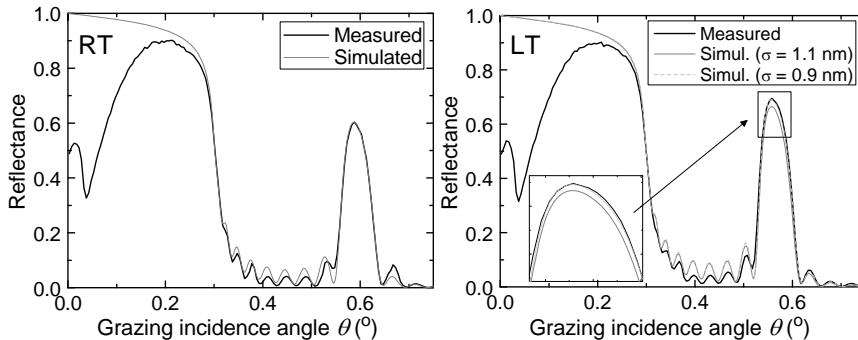


Figure 6.2. GIXR curves of the RT sample (left) and the LT sample (right), in their as deposited state. The results of the simulations are shown in grey.

6.4.2. XPS

The XPS peak intensities and binding energies of the Mo 3d and Si 2p peaks were measured during sputtering depth profiling of the RT and LT samples. The Mo:Si intensity ratio and the binding energy shift as a function of sputter time are shown in Figure 6.3. Figure 6.3a shows that the Mo:Si peak intensity ratio oscillations are larger for the LT sample than for the RT sample. Since practically the same amounts of Mo and Si were deposited, the observed

larger amplitude is a clear indication that the interlayers are thinner in the LT sample.

Figure 6.3b shows that at LT, the Mo $3d_{5/2}$ binding energy oscillates with an amplitude of 0.13 eV, indicating that Mo was present in two different chemical environments, viz. elemental Mo with a binding energy of 227.8 eV and Mo_xSi_y with a binding energy of 227.7 eV. At RT on the other hand, the Mo $3d_{5/2}$ binding energy is nearly constant at 227.7 eV, typical for Mo in a Mo_xSi_y matrix. Hence, we can conclude that less Mo was in a Mo_xSi_y matrix after LT deposition than after RT deposition, i.e., thinner interlayers were formed. Note that sputter depth profiling causes intermixing and, thus, additional silicide formation, which allows conclusions to be drawn on a relative basis only.

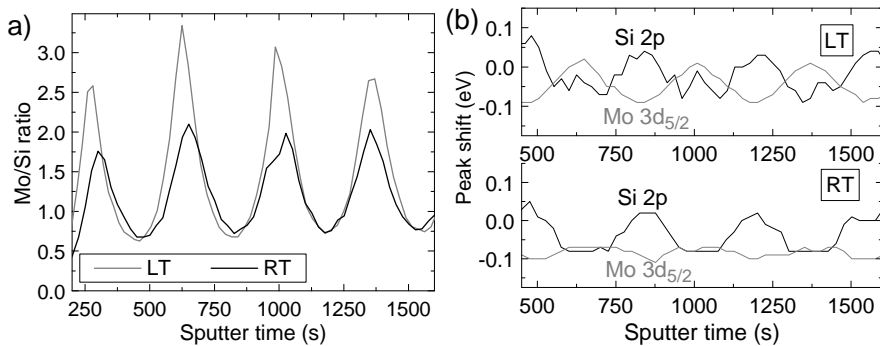


Figure 6.3. XPS depth profiles of the RT and LT samples before annealing. (a): The Si 2p and Mo $3d_{5/2}$ concentration profiles. (b): The shifts of the Si 2p and Mo $3d_{5/2}$ peaks, with respect to their values in elemental form of 99.3 and 227.8 eV, respectively.

6.4.3. WAXRD

Figure 6.4a shows the WAXRD spectra from the LT and RT samples *before* annealing, which exhibit different patterns. The spectrum of the LT sample corresponds to the spectrum of a bcc Mo structure with major peaks at $2\theta = 41, 74, 101$ and 133° and minor peaks at $2\theta = 59, 88$ and 116° [95]. No silicide-related peaks are observed. The RT sample on the contrary only exhibits a sharp peak at 41° and two or more wide, inseparable peaks in the $2\theta = 70\text{--}90^\circ$ range. This spectrum is encountered in our work for e-beam

deposited Mo/Si multilayer structures with thin Mo layers, which exhibit short-range order only [17].

Figure 6.4b displays the WAXRD spectra of both samples after annealing at 375 °C, which are identical, both in shape and intensity. The spectra show that the samples have undergone a phase transformation in which all available Si was consumed to form hexagonal MoSi₂, similar to observations in [17, 18]. The identical intensities imply that equal amounts of MoSi₂ have formed. MoSi₂ formation goes at the cost of the Si and Mo layer thicknesses in a 1:0.4 ratio, so the multilayer samples under investigation with a layer thickness ratio of 1:0.6 had a significant excess amount of Mo. Hence, Si was the limiting factor for MoSi₂ formation, and, therefore equal amounts of MoSi₂ after annealing at 375 °C means that equal amounts of Si were deposited in the RT and LT samples (i.e., the sticking coefficient of Si was equal at RT and LT).

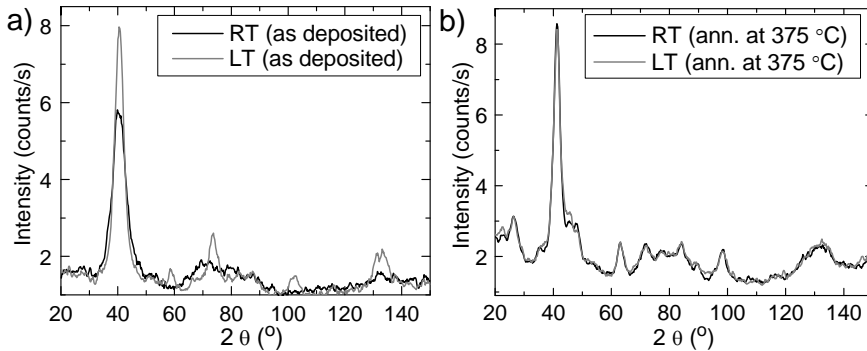


Figure 6.4. WAXRD spectra of both the RT and the LT multilayer samples, in their as deposited state (a) and after annealing at 375 °C (b).

6.5. Discussion

The LT deposition reduced the interlayer formation even after the structure was warmed up to room temperature. Below we will discuss that the interlayer formation during deposition differs from the interlayer formation after the deposition in several aspects.

Several factors make it thermodynamically favorable to form a silicide interlayer between Mo and Si. When in contact, Mo and Si tend to form a

number of energetically favorable silicides [17]. Additionally, the surface free energy for Si is significantly lower than that for Mo (10 eV/nm^2 versus 31 eV/nm^2 [85]). This provides a driving force for surface segregation of Si during Mo-on-Si growth, thus causing interlayer formation by incorporation of Si in the growing Mo layer. Lowering the temperature during the deposition reduces the chance of atoms to overcome the activation energy barrier for displacement needed to reach a more favorable state. Diffusion of both the (ad)atoms into the layer below and the atoms of the underlying layer into the growing film is reduced, mitigating the process of interlayer formation. Once the deposition of the multilayer structure is completed, the displacement energy of the atoms located at interfaces is increased to approximately the value for bulk atoms, which is typically twice the displacement energy for adatoms. Moreover, the driving force for surface segregation has disappeared, since the interface is now located in the bulk of the structure and not at the surface anymore. Therefore, warming up to room temperature is not anymore sufficient to initiate the interdiffusion process like it occurs during film growth at room temperature.

The WAXRD spectra in Figure 6.4 showed that the deposition temperature affected the morphology of the Mo layer. In e.g. Ref. [34, 96, 97], it was observed that the crystalline state of Mo stabilizes the interfaces of Mo/Si multilayer structures. In those studies, the Mo-on-Si interlayer was found to be thicker than the Si-on-Mo interlayer, provided that the Mo layer was crystalline. This is the case when the layer thickness exceeds the critical thickness for crystallization of approximately 2-3 nm [15, 21]. The asymmetry of the interlayers was attributed to the difference between an (initially) amorphous Mo-on-Si interface and a Si-on-crystalline Mo interface. Hence, it is conceivable that in our experiment the crystalline structure of the LT sample stabilized the interfaces *after* the deposition. At the same time, the interdiffusion *during* the (initially amorphous) growth of the Mo layers was reduced by the low temperature. Interdiffusion in the RT sample, on the other hand, could occur during the deposition, while the Mo was still amorphous. In fact, the interlayer formation in the RT sample consumed significantly more Mo, compared to the LT sample, so the remaining Mo layer in the RT sample did not exceed the critical thickness for crystallization at all and exhibited short-range order only.

On a more applied note: the performance of a multilayer mirror primarily depends on interlayer thickness as well as (interfacial) roughness. Whereas the former has been discussed in detail, the roughness has not yet been

addressed. Roughness develops due to the stochastic nature of the growth process, and can be mitigated by adding energy to the structure in the form of an enhanced substrate temperature or energetic particles (ions). Obviously, increasing the substrate temperature in order to reduce the roughness is in conflict with cooling the substrate in order to reduce the interlayer thickness. Combining low temperature deposition with ion bombardment, on the other hand, is worth investigating as it has a high potential to result in both smooth interfaces and thin interlayers. This approach is expected to have a beneficial effect on the reflectivity of multilayer optics and can be applied to multilayer structures of any material combination. According to IMD simulations, the observed interlayer reduction of 0.9 nm per period would increase the EUV reflectance of a typical state-of-the-art 50-period multilayer mirror from 69% to 71%.

6.6. Conclusion

The effect of cooling the substrate with liquid nitrogen during the deposition of Mo/Si multilayer structures on the interlayer thickness has been investigated. Using XPS depth profiling, WAXRD, and GIXR upon progressive annealing it was determined that the total interlayer thickness at both interfaces was reduced by (0.9 ± 0.2) nm (~60 %) compared to deposition at room temperature, even after the sample was warmed up to room temperature. With this we demonstrated that the substrate temperature during deposition affects the kinetics of the interlayer formation in Mo/Si multilayered structures. We suggest that this effect can be attributed to a lower adatom mobility, reduced surface segregation of Si during Mo-on-Si growth, and/or crystallization of Mo. When combined with ion bombardment, low temperature deposition of multilayer structures is expected to have a beneficial effect on the reflectivity of multilayer optics.

6.7. Acknowledgments

Hans Zeijlemaker and Johan Derks are gratefully acknowledged for their skillful technical assistance. This work is part of the FOM Industrial Partnership Programme I10 ('XMO') which is carried out under contract with Carl Zeiss SMT AG, Oberkochen and the 'Stichting voor Fundamenteel Onderzoek der Materie (FOM)', the latter being financially supported by the 'Nederlandse Organisatie voor Wetenschappelijk Onderzoek (NWO)'.

7. Roughness evolution of Si surfaces upon Ar ion erosion

7.1. Abstract

We studied the roughness evolution of Si surfaces upon Ar ion erosion in real-time. Following the theory of surface kinetic roughening, a model proposed by Majaniemi was used to obtain the value of the dynamic scaling exponent β from our data. The model was found to explain both the observed roughening and the smoothing of the surfaces. The values of the scaling exponents α and β , important for establishing a universal model for ion erosion of (Si) surfaces, have been determined. The value of β proved to increase with decreasing ion energy, while the static scaling exponent α was found to be ion energy independent.

7.2. Introduction

The analysis of Si surface roughness evolution under ion treatment and the determination of technological parameters necessary to preserve or to improve the surface smoothness are becoming increasingly important for advanced, reflective X-ray/Extreme Ultraviolet (EUV) optics. This notably concerns the next generation of optics [98], where ion etching is used to figure a macroscopic Si substrate with sub-nanometer accuracy while the microscopic roughness is maintained at an atomic level [99]. It is furthermore of major importance for the fabrication of multilayer reflective coatings for EUV optics. The Mo/Si multilayer mirrors with the best reflectivity are obtained when an ion polishing step of the Si layers is included in the manufacturing process [26, 29, 100].

In general, a variety of surface patterns can be observed upon ion treatment (smoothing, roughening, formation of ripples, nanodots, etc.), see e.g. Ref. [101]. These topographies depend on the etch time, the surface material, the ion energy, and the ion angle of incidence. The final surface topography is determined by competing roughening and smoothing mechanisms with different spatial-frequency and time dependencies. A surface that is growing

or eroding under non-equilibrium conditions often develops as a fractal-like structure. This effect has been observed and formalized within the theoretical framework of surface dynamic scaling or kinetic roughening [102, 103]. In this concept, several parameters, known as scaling exponents, can be used as the signatures in space and time of the growth or etch processes. By comparing the experimental scaling exponent values with the theoretical predictions, one can establish, in principle, a differential equation describing the film growth or erosion at a mesoscopic level. As an example, it was demonstrated in Ref. [104] that the evolution of the roughness of a tungsten film during Ar^+ ion erosion is consistent with the prediction of the Kardar – Parisi – Zhang (KPZ) equation [102]. Being a universal description of the ion erosion of Si surfaces, such an equation would contribute tremendously to the understanding of the interplay between the mechanisms leading to different morphologies and dynamics for ion-eroded surfaces [105], and also provide the ultimate tool for the selection of etch settings that lead to the best smoothening results.

The classical formulation of the scaling model assumes that the initial substrate is perfectly smooth. A number of questions arise in this framework. For instance, does the scaling behaviour depend on the initial substrate roughness? Is it possible to divide the eroded surface roughness into contributions from the initial substrate roughness and from the erosion induced roughness, the latter following the scaling law? Answers to these questions are important for the further development of the ion etching technology.

In the present paper we describe experimental results on a study of the surface evolution of Si substrates with a different initial roughness upon Ar ion treatment. The goals of the study are (a) verification of the scaling model at the initial stage of ion etching, when the initial substrate roughness gives an essential contribution to that of an eroded surface, (b) analysis of the dependency of the surface dynamics on the initial substrate roughness and the ion energy, and (c) analysis of the possibility to distinguish between the two factors that contribute to the roughness of an eroding surface, viz. the initial surface roughness and the erosion induced roughness.

7.3. Experimental details

Among different techniques used for determination of the scaling parameters, the X-ray Scattering (XRS) method has a number of advantages, like allowing studying the evolution of the surface roughness in-situ and in real time. This is essential, because oxidation or contamination by a vacuum background may result in an uncontrolled development of the surface roughness.

The experiments have been conducted at the grazing incidence x-ray reflectometry setup at the BM5 beamline of the ESRF synchrotron facility. The setup has been described in detail in e.g. Ref. [105]. B-doped (100) silicon wafers with a thickness of 725 μm were used as substrates and mounted in a vacuum chamber. The X-ray beam enters and exits the chamber via 150 μm thick Kapton foil windows. A microwave electron cyclotron resonance plasma source (\varnothing 25 mm, described in detail in Ref. [106]) provided Ar ions for sample erosion. It was mounted at a distance of 8 cm from the sample and the grazing angle of incidence was set to 55° with respect to the sample surface.

In order to characterize the ion erosion process, a set of diffuse scatter patterns (scattering diagrams) has been recorded with a CCD camera (1024×256 pixels, pixel size $19 \times 19 \mu\text{m}^2$, and integration time 5 s) that was placed at a distance of 1 m from the sample. The camera was cooled with liquid nitrogen to reduce the thermal noise. A beamstop was installed in front of the CCD camera to block the specular reflected beam and prevent detector overexposure. The X-ray energy was set to 17.5 keV ($\lambda = 0.071$ nm), and the grazing angle of the probe beam was 0.09° , which is just below the critical angle for total external reflection. The vertical X-ray beam size was set to 0.2 mm, while the horizontal beam size was set to 4.6 mm to favor a high intensity at the detector. As the scattering diagram is very narrow in the azimuthal (horizontal) plane, the scattered intensity was integrated in this direction through pixel binning.

The scattering diagram $\Pi(\theta)$ from an isotropic surface is, according to first order perturbation theory, proportional to the one-dimensional power spectral density (PSD_{1D}) function of the surface roughness (see, e.g., Ref. [107]). Therefore, the PSD-function can be deduced from the experimental data directly via:

$$\begin{aligned} \Pi(\theta) &= \frac{1}{W_i} \frac{dW_{scat}}{d\theta} \\ &= \frac{k^3 |1 - \varepsilon|^2 |T(\theta_0)T(\theta)|^2}{16\pi \sin \theta_0 \sqrt{\cos(\theta_0)\cos(\theta)}} \cdot PSD_{1D}(\nu), \end{aligned} \quad (7.1)$$

with

$$\begin{aligned} PSD_{1D}(\nu) &= 4 \int \langle z(\bar{\rho}), z(0) \rangle \cos(2\pi\nu\rho) d\rho; \\ \nu &= \frac{1}{\lambda} |\cos \theta - \cos \theta_0|; \quad T(\theta) = \frac{2 \sin \theta}{\sin \theta + \sqrt{\varepsilon - \cos^2 \theta}}, \end{aligned} \quad (7.2)$$

where W_i and dW_{scat} are the radiation powers of the incoming beam impinging under an angle θ_0 and of the outgoing beam scattered in the θ direction within an angular interval $d\theta$, respectively. The spatial frequency is denoted by ν ; the dielectric constant of the sample by ε ; the wavenumber by $k = 2\pi / \lambda$, and the amplitude transmittance of a perfectly smooth surface by $T(\theta)$. The function $z(\bar{\rho})$ describes the surface relief, and angular brackets denote an ensemble averaging. The procedure for normalization of the scattering data is described, e.g., in Ref. [108].

In addition to the scattering measurements, experiments were performed on etching of 60 nm thick Si films deposited onto Si substrates in order to establish the etch rate as a function of the ion energy. The film thickness before and after a short etching step was determined from a θ - 2θ scan that was measured with a scintillator detector. The thus obtained etch rate was 0.12 nm/s at an ion energy of 300 eV and 3.5 nm/s at 1000 eV (argon pressure $1 \cdot 10^{-3}$ mbar).

In two of the three experiments presented below, the sample surface was roughened beforehand with a 10 minute, 1000 eV Ar^+ treatment at a grazing angle of $\theta = 10^\circ$ and an Ar pressure of $1 \cdot 10^{-3}$ mbar. Table 7.1 gives an overview of the samples used for the investigation reported in this Chapter.

Table 7.1. Overview of the sample coding and properties.

Sample code	Ion energy (eV)	Preliminary roughening	Etch rate (nm/s)
NR_{1000}	1000	No	3.5
R_{1000}	1000	Yes	3.5
R_{300}	300	Yes	0.12

7.4. Results and discussion

Figure 7.1 and Figure 7.2 show the evolution of the PSD-function and the rms roughness of the three samples studied. Sample NR_{1000} is initially very smooth with a rms roughness of only 0.15 nm in the $[2 \cdot 10^{-4}, 2 \cdot 10^{-2} \text{ nm}^{-1}]$ spatial frequency range. Nevertheless, no significant increase in roughness is observed during etching with 1000 eV Ar^+ ions despite the large removed thickness of 1.2 μm . In contrary, when the sample is roughened prior to the experiment (sample R_{1000}), very fast smoothing of the surface occurs during the first 20 s of the ion treatment. The roughness reduction is especially pronounced in the mid and high spatial frequency range, while the low frequency part of the roughness spectrum is much less affected. The rms roughness of both samples (NR_{1000} and R_{1000}) becomes almost the same after about 20 s of etching, which demonstrates that the memory of the initial roughness is only lost after removal of 70 nm Si, despite the very small initial roughness of the samples (0.15 and 0.28 nm).

The PSD-function and the rms roughness of a beforehand roughened sample evolve more gradually when the etching energy is reduced to 300 eV (sample R_{300}), as can be expected from the 30-fold reduction of the etching rate. The high frequency roughness is reduced in the first 30 s of the etching treatment, after which it remains almost constant. At lower spatial frequencies, on the other hand, the initial smoothing is followed by a slower, but pronounced roughening.

In general, and compatible with recent results for flat Si targets at normal incidence and in a similar energy range [109], we obtain no pattern formation

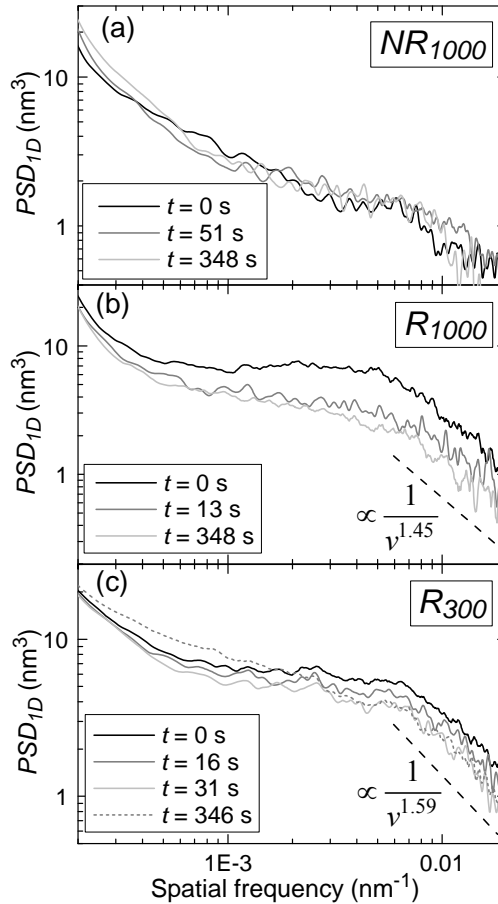


Figure 7.1. Evolution of the PSD-function of the samples studied upon etching. The dashed lines indicate the asymptotic behavior for the PSD_{1D} at high spatial frequencies.

in our etching experiments. However, while for the non-roughened sample the ensuing surface morphology remains basically featureless as in Ref. [109], both samples R_{1000} and R_{300} develop non-trivial correlations at small length-scales / high spatial frequencies with increasing irradiation time (see Figure 7.1), that can be described within the framework of surface kinetic roughening. This requires that the 1D PSD-function of the film roughness behaves as an inverse power law $PSD_{1D}(\nu) \sim 1/\nu^{1+2\alpha}$ at high spatial frequencies ν . Hence, through analysis of the asymptotic behaviour of the PSD-function at large ν , one can determine the so-called static scaling exponent α . This exponent characterizes the saturated roughness and is found

to equal $\alpha = 0.23 \pm 0.08$ for sample R_{1000} and $\alpha = 0.30 \pm 0.05$ for sample R_{300} . Therefore, within the experimental error we can conclude that the value of α is independent of the ion energy. For sample NR_{1000} the exponent α is not clearly defined in the spatial frequency range measured in the XRS experiment.

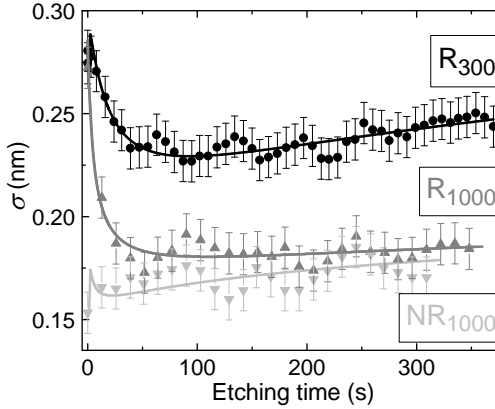


Figure 7.2. The evolution of the root-mean-square roughness σ upon etching, for each of the three samples. The thick, solid lines represent the best fits in the framework of the Majaniemi model (Eqs. (7.3), (7.5)). The curves R_{1000} and NR_{1000} have been fitted simultaneously with the same values for the fitting parameters. The, initially dominant, contribution of σ_E gives rise to a sharp increase of σ , and is followed by smoothening due to the decreasing value of σ_S .

The dynamic exponent β can be found from analysis of the rms roughness evolution with the erosion time $\sigma^2(t) = \int \text{PSD}_{ID}(\nu) d\nu \sim t^{2\beta}$. However, this equation implies a perfectly smooth initial surface. In reality, the surface roughness upon etching is determined by two factors: the initial roughness of the initial substrate σ_S disappearing with the erosion time, and the etching induced roughness σ_E following the scaling law $\sigma_E(t) \sim t^\beta$.

The question how to distinguish between the contributions of σ_S and σ_E was considered in detail by Majaniemi *et al.* in Ref. [110], where the analysis was based on the linear theory of film growth or erosion. The authors of Ref. [110] demonstrated that it is necessary to discriminate two cases, depending on whether the correlation length of the treatment-induced roughening

process $\zeta(t) \sim t^{\beta/\alpha}$ is smaller or larger than that associated with the initial roughness ζ_s . In the early stage of growth/erosion, the initial substrate roughness σ_s was found to give a constant contribution to the treated surface roughness $\sigma(t)$, regardless of the growth/erosion time:

$$\sigma^2(t) = \sigma_s^2 + \sigma_E^2(t); \quad \sigma_E = A \cdot t^\beta; \quad \zeta(t) \ll \zeta_s, \quad (7.3)$$

with A a proportionality constant. However, when the correlation length of the treatment induced roughness becomes larger than that of the initial substrate roughness, the contribution of the initial substrate to the surface evolution depends on the treatment time, i.e. $\sigma_s \rightarrow \sigma_s(t)$ in Eq. (7.4), and decays universally with the deposition/erosion time as

$$\sigma_s(t) = \sigma_s(0) \cdot \zeta_s / \zeta(t); \quad \zeta(t) \gg \zeta_s. \quad (7.4)$$

To obtain a smooth transition between the two limiting cases (7.3) and (7.4), the authors of [12] suggest the following formula

$$\sigma_s(t) = \frac{\sigma_s(0)}{(1+t/t_s)^{\beta/\alpha}}, \quad (7.5)$$

where t_s is a fitting parameter.

The solid curves in Figure 7.2 are the result of fitting $\sigma^2(t)$ according to Eqs. (7.3) and (7.5), using α as obtained from the asymptote in Figure 7.1, and taking the 5 s recording time of the CCD detector into account. Note that evolution of the rms roughness of samples NR_{1000} and R_{1000} is described properly with the use of the same set of fitting parameters, namely, $\beta = 0.07 \pm 0.01$ and $t_s = 2.6 \pm 0.4$ s. As seen in Figure 7.2, the Majaniemi model (Eqs. (7.3), (7.5)) simultaneously explains smoothing as well as roughening of a surface upon ion erosion, depending on the rms roughness of the initial substrate. Note that the very small value of β could also be compatible with very slow logarithmic growth of the roughness. Similarly, the evolution of the rms roughness of the sample R_{300} is well described by Eqs. (7.3), (7.5), although the fitting parameters are different: $\beta = 0.14 \pm 0.02$ and $t_s = 16 \pm 2$ s, demonstrating that the value of the dynamic scaling exponent β depends on the ion energy.

The derived sets of scaling exponents α and β correspond to none of the growth/erosion equations reported in the literature. Such a disagreement has already been pointed out in literature (see, e.g., Ref. [111] and references therein) and may be due to the high degree of complexity of the eroded surface dynamics.

7.5. Conclusions and outlook

We analyzed the roughness evolution of Si substrates upon Ar ion etching. The evolution was demonstrated to depend on the initial substrate roughness σ_S : a small increase of the rms roughness was observed for the smoothest sample upon etching at an ion energy of 1000 eV, while very fast smoothing was observed during the first 30 s of etching of a rougher sample. After 30 s of ion erosion, the surface dynamics were the same for both samples, regardless of the initial surface roughness. Smoothing was also observed for an initially rough sample that was eroded at a lower ion energy (300 eV).

The static scaling exponent was demonstrated to be independent of the ion energy (within experimental uncertainty): $\alpha = 0.23 \pm 0.08$ for etching at 1000 eV, and $\alpha = 0.30 \pm 0.05$ for etching at 300 eV. The Majaniemi model, which divides the eroded surface roughness into contributions of the initial substrate roughness and the erosion induced roughness, was demonstrated to properly describe our experimental data. This model, based on the analysis of linear equations describing growth/erosion processes, was used to fit our data and obtain the dynamic scaling exponent β . Using the same set of parameters, the model explains both the observed roughening of the smoothest sample and the smoothing of the roughened sample upon erosion with 1000 eV Ar⁺. While no ion energy dependency was found for the static scaling exponent, the dynamic scaling exponent proved to increase with decreasing ion energy: $\beta = 0.07 \pm 0.01$ at $E = 1000$ eV and $\beta = 0.14 \pm 0.02$ at $E = 300$ eV. The scaling exponents α and β are important parameters for the determination of a comprehensive theory of ion erosion of (Si) surfaces. However, in order to accomplish the greater goal of a full theory of ion erosion of Si surfaces, it is necessary to investigate a larger part of the parameter space. More experiments have to be conducted in which the ion energy, angle of incidence, ion mass, and initial surface roughness are varied. The comprehensive theory resulting from such experiments would be a leap

forward in the understanding of ion-solid interactions, and be of great interest for miscellaneous thin film applications.

7.6. Acknowledgments

I.V. Kozhevnikov acknowledges the support of the ISTC (project #3124). V.I.T.A. de Rooij-Lohmann, F. Bijkerk, and A.E. Yakshin acknowledge the FOM Industrial Partnership Programme I10 ('XMO') which is carried out under contract with Carl Zeiss SMT AG, Oberkochen, and the 'Stichting voor Fundamenteel Onderzoek der Materie (FOM)', Utrecht, the latter being financially supported by the 'Nederlandse Organisatie voor Wetenschappelijk Onderzoek (NWO)'. R. Cuerno acknowledges partial support by grants FIS2006-12253-C06-01 (MEC, Spain), FIS2009-12964-C05-01, (MICINN, Spain), and CCG08-CSIC/MAT-3457 (CAM, Spain). The authors further acknowledge the European Synchrotron Radiation Facility, Grenoble, for providing the measurement facilities (beamline BM05).

8. Valorisation and Outlook

8.1. Progress in Lithography, Progress for Society

Our modern society relies heavily on information technology and integrated circuits: within two or three decades, a world without computers, internet, cable television and mobile phones has become unthinkable. Consumers expect the progress in this field to continue at the fast pace they have become so used to. Such progress requires advances and innovations in lithography, the mass production process for computer chips. Naturally, extensive research is needed to realize these innovations.

The research at the nanolayer- Surface and Interface Physics (nSI) department at the FOM Institute for Plasma Physics Rijnhuizen focuses on achieving the knowledge to create multilayer mirrors that are thermally stable, have a high reflectance, and withstand contamination and/or cleaning procedures. As such, it has caught the interest of the EUV lithography community, and developed a long-standing, intensive collaboration with ASML and Carl-Zeiss, manufacturers of lithography tools and optical systems, respectively. The research reported in this thesis has been conducted under the Zeiss-FOM co-funded Industrial Partnership Programme I10, entitled *eXtreme UV Multilayer Optics* (XMO). The output of this programme bears witness to the large scientific as well as industrial value of XMO: besides 8 patents, the research so far led to two more doctoral theses [112, 113] and 19 publications in peer-reviewed journals. Besides the work presented in this thesis, the studied topics include the characteristics of Mo/Si interfaces and their changes upon thermal load, the dependence of the roughness on ion etching parameters, and oxidation/reduction behavior of various capping layer materials. The goal of the project, developing multilayer optics for EUV lithography, was achieved to the satisfaction of all parties. The results of the diffusion studies in this thesis have contributed to the design of these mirrors. Therefore, the fruitful collaboration is now continued with CP3E, a vast program in which ASML, Carl-Zeiss, and nSI join forces to achieve understanding of and control over the collective plasma-physical, photochemical and multilayer thin film processes, so that the know-how can be developed to achieve the required lifetime of the optics. The project comprises investment of several million euro and twenty-two employees,

amongst whom eight Ph.D. students. These numbers by themselves are yet another illustration of the economical value of the research conducted in the nSI department. The remainder of this section will focus on both the scientific and the applied merit of the research presented in this thesis.

8.2. LEIS

Until very recently, the analysis of LEIS spectra was largely restricted to the so-called elastic scatter peaks that stem from scattering of the ion at the outermost atomic layer. With this unrivalled surface sensitivity, LEIS has a long tradition in catalysis, where the outer surface is all that matters and where poisoning of the catalyst is a major concern. Furthermore, LEIS is acknowledged as a very useful technique for studying the growth and contamination of thin films (see, e.g., Refs. [44, 114-116]. Chapters 3 and 4 have opened an additional application area, by demonstrating that careful analysis of the contribution of inelastically scattered ions can lead to valuable information about the subsurface of and diffusion processes in nanometer-scale thin films. As such, LEIS has become an attractive option for the study of interfaces and nanoscopic diffusion. Thanks to the ongoing miniaturization of electronical components and integrated circuits, this has become a vast research field. The commercial worth of our work is comprehended by ION-TOF GmbH, a company that started the sales of a commercial LEIS instrument in 2008. ION-TOF has a natural, economic interest to enlarge the market segment via expanding the usability of LEIS. In this framework, our work is advertized in their promotional material and a number of conference presentations by representative Hidde Brongersma.

Nanoscale diffusion studies of Mo/Si systems are of high relevance to users and manufacturers of multilayer optics, since interdiffusion is the main lifetime-reducing process in multilayer mirrors. The diffusion rates are negligible at room temperature, but during operation and cleaning the temperature of the mirrors may climb significantly due to the large heatload. Still, the mirrors must have a guaranteed lifetime of several years. The fast and accurate way to monitor interdiffusion in thin films that was demonstrated in Chapter 3 enables accelerated lifetime studies and can be helpful for further research on (the reduction of) interdiffusion. The unparalleled sensitivity can be utilized to obtain measurements of the mirror degradation due to e.g. interdiffusion or surface contamination, on the relatively short time-scale of a week. The extrapolation of such measurements

can be used for lifetime predictions. Furthermore, unlike X-ray reflection methods (like described in Section 2.2.1), LEIS can be used to study diffusion in few-layer systems. This allows investigation of a single interface rather than an average over many. This property makes LEIS especially suitable for studying interface asymmetry, i.e., possible differences between Mo-on-Si and Si-on-Mo interfaces in growth or diffusion behavior of diffusion barrier layers.

The work on thin film growth and interlayer formation can be taken to a new level by elimination of the necessity to transport samples through the ambient, since LEIS measurements are highly sensitive to oxidation and contamination. For this reason, the CP3E grant mentioned above provides for the acquisition of a LEIS instrument allowing for in situ analysis at a deposition setup. Apart from the interdiffusion and contamination studies mentioned above, an in situ LEIS instrument would make it possible to analyze growing layers quasi real-time. Such analyses would allow determination of the growth modes of the various materials, and how the growth is affected by deposition parameters like pressure, deposition rate, substrate material or temperature.

8.3. Mo, Si and B₄C – Physics and Chemistry

In 2001, Bajt, Stearns and Kearney [15] showed that insertion of a B₄C layer at each Mo/Si interface enhances both the reflectivity and the thermal stability of the multilayer mirrors. Understanding of this practical solution to improve the throughput of the lithography tool and the lifetime of the mirror was lacking though. While Chapters 4 and 5 answered questions regarding the interaction of B₄C with Si and Mo, Chapter 4 has shown that crystallization of the interlayer accelerates the diffusion in Mo/B₄C/Si systems. It implies that, even at a nanoscale, the morphology is of utmost importance for diffusion processes, and thus for the lifetime of many products in which nanotechnology is utilized. As a practical consequence, the possibility of crystallization of the compounds that form upon interdiffusion has to be taken into account when designing any nanoscopic structure, like multilayer optics, integrated circuits and Micro-Electro-Mechanical Systems (MEMS). After all, the determination of the lifetime of such devices by extrapolation of relatively brief diffusion experiments may lead to a serious overestimation of the lifetime: if the interface has not crystallized during the lifetime test, it may crystallize later on, causing an unanticipated increase in the diffusion rate.

The results in Chapter 4 not only posed the problem of crystallization, it also pointed to the solution: addition of a crystallization-retarding agent (B for Mo/Si systems) can postpone or even prevent crystallization, and thus increase the device's lifetime.

Furthermore, the results reported in Chapter 5 indicate that B_4C and C, in contrast to B, form a stable silicide upon annealing when in contact with Mo and Si. Si has to diffuse through this layer in order to form $MoSi_2$, which makes it plausible that the SiC_x/SiB_xC_y layer functions as a diffusion barrier. In fact, the diffusion barrier properties of B_4C as reported in literature may even be caused by the stability of the formed SiB_xC_y layer rather than by the B_4C layer itself. The presence of C was essential for the formation of the $Si(B_x)C_y$ layer, while a significant amount of B still diffused into the Mo layer. This suggests that maybe for lack of C, only part of the available B could be used to form SiB_xC_y . Therefore, the same barrier functionality may be realized with a thinner boroncarbide layer when the B:C ratio is reduced, thus allowing a higher reflectivity of the multilayer mirror. In view of the necessity of a high reflectivity as well as excellent thermal stability, the effect of the stoichiometry of the boroncarbide on both is an interesting topic for further research that can lead to higher quality EUV optics.

8.4. Cryogenic deposition

Chapter 6 shows that deposition at cryogenic substrate temperatures is a successful way to create sharper interfaces. The principle was demonstrated for Mo/Si multilayer structures, but has potential for other nanotechnological applications where sharp interfaces are desirable, e.g., for gate structures in fast transistors. It is especially valid for multilayer structures for optical applications, due to the many interfaces and the high demands on the reflectance. As an example, at the 2009 International Symposium on Extreme Ultraviolet Lithography in Prague, Carl Zeiss presented an optical design that could increase the resolution of EUVL from 22 nm to 11 nm. This was attained by increasing the numerical aperture from 0.32 to 0.5 at the cost of two additional mirrors. The associated loss of throughput of 50 % could be reduced to 30 % when the reflectance of each mirror is increased by 2 %, which could, according to calculations, be achieved by cryogenic deposition of the multilayer mirrors.

While Chapter 6 answered the question whether cryogenic deposition leads to thinner interfaces, it also gave rise to many new questions, like does cryogenic deposition substantiate the calculated reflection gain of 2%? How does ion erosion at cryogenic temperature compare to ion erosion at room temperature? Is cryogenic deposition also effective if deposition is done by magnetron sputtering instead of electron beam evaporation, despite the more energetic particles created with that method? How does cryogenic deposition affect the growth of (B₄C) diffusion barrier layers? It has, for instance, been reported that B₄C growth at the Si-on-Mo interface is stoichiometric, while it is overstoichiometric (B:C ratio > 4:1) in thin films (<1.5 nm) at the Mo-on-Si interface [92]. The overstoichiometry at the Mo-on-Si interface can perhaps be mediated by increasing the sticking coefficient to near-unity by cooling the substrate.

The large substrate thickness (typically 5 cm) of real mirrors and the required precision of the mounting in the deposition facility make it technically very challenging to cool down to cryogenic temperatures. Nevertheless, a relatively small temperature decrease may already have a significant effect. It is, therefore, worthwhile to investigate to what extent the surface of a substrate can be cooled down, and if that temperature is sufficiently low to decrease the interface thickness.

The above suggested research themes require a facility that is capable of depositing multilayer structures with a large number of periods accurately and reproducibly. To facilitate this research a new sample holder that can be cooled with liquid nitrogen has been designed, manufactured and installed on one of the deposition facilities (coater C) in 2009. Contrary to the cryogenic deposition facility (coater B) used for the work in this thesis, coater C is largely automated, which increases the number of periods of a multilayer that can be coated in one day. Furthermore, the new substrate holder has the important advantage that it rotates at a frequency of 1 Hz to allow uniform deposition and ion beam smoothing, and is equipped with several thermocouples to monitor and control the temperature of the samples and the holder.

8.5. Roughness evolution

The Si ion erosion study by hard x-ray scattering, presented in Chapter 7, led to interesting results, but was unfortunately limited to a few parameter sets. In

order to accomplish the greater goal of a comprehensive theory of ion erosion of Si surfaces, it is necessary to investigate a much larger part of the parameter space. In other words, many more experiments have to be conducted in which the ion energy, angle of incidence, ion mass, and initial surface roughness are varied. The comprehensive theory resulting from such experiments would be a leap forward in the physics of ion-solid interactions, and be of great interest for (industrial) thin film applications as well.

The x-ray scattering method was demonstrated for Si, despite the poor optical contrast with vacuum in the hard x-ray regime. Consequently, the method works even better for other materials. It could, for instance, be a very useful way to optimize La ion polishing for La/B₄C multilayer optics for 6.7 nm lithography.

In general, Chapters 4-7 offer insight in interdiffusion, the chemical reactivity of diffusion barrier materials with Mo and Si, the effect of cryogenic deposition, and ion beam smoothening of Si layers. This knowledge contributes to the development of better optics for the soft X-ray / extreme ultraviolet regime. The improved optics will have an increased reflectance and thermal stability, and make new wavelength ranges accessible. Astronomy, synchrotron-based research and research on semiconductor electronics and magnetic recording devices will benefit from new possibilities (e.g., EUV photoelectron microscopy) and the higher radiation intensity.

Summary

This thesis addresses the physical and chemical phenomena in Mo/Si multilayer structures with and without B₄C diffusion barrier layers at the interfaces. Acting as Bragg reflectors, such multilayer structures are applied in extreme ultraviolet (EUV) / soft X-ray optics in e.g., space telescopes and next-generation photolithography equipment. Since interdiffusion and interlayer formation limit both the performance and the lifetime of the optics, understanding of processes at the interfaces is essential for improving the quality, and thus the commercial viability of EUV optics. Therefore, the interlayers and their evolution in time have been investigated in detail. In combination with the difficulty to measure at the sub-nanometer length-scale at which these processes take place, the occurrence of a variety of physical and chemical processes required that a multitude of analysis techniques was used for the research presented in this thesis. For the interpretation of one of those techniques (Low Energy Ion Scattering spectroscopy, LEIS), an analysis procedure has been developed. This procedure utilizes the depth-resolved information that is contained in a LEIS spectrum, thus allowing for non-destructive studies of interdiffusion in ultrathin films with sub-nanometer resolution. When the diffusion in Mo/B₄C/Si layered structures was studied with LEIS, it was found that the diffusion initially obeys Fick's second law. However, after a certain time that scales with the thickness of the B₄C diffusion barrier layer, the diffusion rate instantaneously increased by up to one order of magnitude. The cause of this acceleration of the diffusion was found to be the amorphous-to-nanocrystalline transition of the MoSi₂ interface.

Besides diffusion and crystallization, the chemical processes upon annealing of Mo/B₄C/Si layered structures have been investigated and identified. In addition, Mo/B/Si and Mo/C/Si samples were studied as reference systems. For all structures, the chemical changes occurred in two distinct stages. In the first stage, predominantly MoB_xC_y (resp. MoB_x and MoC_x) was formed, plus small amounts of SiB_xC_y (resp. SiB_x and SiC_x). MoSi₂ formed in the second stage, while the already formed MoB_xC_y (resp. MoB_x and MoC_x) diffused further into the Mo layer. The interaction of B interlayers with Mo and Si differs from that of both C and B₄C because only the latter two formed stable silicides, through which Si diffused to form MoSi₂ in the second stage.

In addition to the characterization of the interlayer and the interfacial processes, it was investigated whether the interlayer thickness can be reduced by depositing the multilayer mirror at a low temperature. To this end, the kinetics involved in interlayer formation were affected by cooling the substrate with liquid nitrogen during the deposition. Even after warming up to room temperature, the interlayers that formed upon cryogenic deposition were found to be nearly 60 % thinner than after room temperature deposition. This effect is attributed to a lower adatom mobility that prevents adatoms to diffuse into the layer underneath, reduced surface segregation of Si during Mo-on-Si growth, and/or crystallization of Mo before an interlayer could form.

Finally, since rough interfaces between the layers of a multilayer mirror are equivalent to thick interlayers, it is important to control the roughness during the deposition. The development of roughness is usually mitigated by means of ion bombardment of the Si layers. To gain understanding of the roughness evolution upon ion erosion, which may lead to the ability to create smoother interfaces, the roughness evolution of Si surfaces upon Ar ion erosion was studied in real-time. It was demonstrated that ion treatment can cause roughening as well as smoothening, depending on the initial roughness of the substrate. The results were explained using a literature model, and the values of the scaling exponents, which are important for establishing a universal model for ion erosion, have been determined.

Samenvatting

Dit proefschrift behandelt de fysische en chemische verschijnselen die plaatsvinden in Mo/Si multilaag structuren, zowel met als zonder B₄C diffusiebarrièrelagen op de grensvlakken. Deze multilaag structuren gedragen zich als Bragg reflectoren en worden toegepast als optieken voor straling in het extreem ultraviolet (EUV) / zachte röntgen gebied, bijv. in ruimtetelescopen en de komende generatie fotolithografie apparatuur. Aangezien interdiffusie en de vorming van grenslagen van gemengde samenstelling zowel de prestatie als de levensduur van de optieken verminderen, is kennis over de processen in de grenslagen van essentieel belang om de kwaliteit en daarmee de commerciële haalbaarheid van EUV optieken te verbeteren. Derhalve zijn de grenslagen en hun tijdsevolutie in detail onderzocht. De uitdaging om metingen te verrichten op nanometerschaal, de schaal waarop deze processen plaatsvinden, heeft er in combinatie met de verscheidenheid aan fysische en chemische processen toe geleid dat er een breed scala aan analysetechnieken is gebruikt. Voor de interpretatie van de resultaten van één van deze technieken (Lage Energie Ionen Verstrooiing, LEIS) is een analyseprocedure ontwikkeld. Gebruik makend van de diepte-informatie in een LEIS-spectrum maakt deze procedure het mogelijk om non-destructief de interdiffusie in ultradunne lagen met subnanometer resolutie te bestuderen. Uit toepassing van deze methode bij onderzoek naar de diffusie in gelaagde Mo/B₄C/Si structuren kwam naar voren dat de diffusie aanvankelijk verloopt volgens de tweede wet van Fick. Echter, na een zekere tijd die schaalt met de dikte van de B₄C diffusiebarrièrelaag, versnelde de diffusie instantaan met tot één orde van grootte. De oorzaak van deze versnelling bleek de amorf-nanokristallijne faseovergang van de MoSi₂ grenslaag te zijn.

Naast diffusie en kristallisatie zijn ook de chemische processen tijdens thermische behandeling van gelaagde Mo/B₄C/Si structuren onderzocht en geïdentificeerd. Ter referentie zijn tevens Mo/B/Si en Mo/C/Si monsters onderzocht. Voor alle monsters geldt dat de chemische veranderingen zich in twee stadia voltrokken. In het eerste stadium vormde zich voornamelijk MoB_xC_y c.q. MoB_x en MoC_x, plus kleine hoeveelheden SiB_xC_y c.q. SiB_x en SiC_x. MoSi₂ werd gevormd in het tweede stadium, terwijl het al gevormde MoB_xC_y c.q. MoB_x en MoC_x verder de Mo laag in diffundeerde. De interactie van B tussenlagen met Mo en Si onderscheidde zich van dat van C en B₄C,

doordat enkel bij de laatste twee stabiele silicides ontstonden, waar Si in het tweede stadium doorheen diffundeerde teneinde in MoSi_2 te vormen.

Naast de karakterisatie van de processen in de grenslagen en op de grensvlakken, is onderzocht of de dikte van de grenslaag kan worden verkleind door de multilaag spiegel bij lage temperatuur te deponeren. Daarom zijn de kinetische processen die betrokken zijn bij de vorming van de grenslaag beïnvloed door het substraat tijdens de depositie te koelen met vloeibare stikstof. Zelfs nadat de structuur was opgewarmd tot kamertemperatuur, bleken de grenslagen die vormden na kryogene depositie bijna 60 % dunner te zijn dan na depositie bij kamertemperatuur. Dit effect wordt toegeschreven aan een afgenomen oppervlakte-segregatie van Si tijdens de groei van Mo-op-Si, de kristallisatie van Mo vóórdat een grenslaag heeft kunnen vormen, en/of een lagere mobiliteit van adatomen, wat voorkomt dat adatomen naar de onderliggende laag diffunderen.

Tenslotte is het van belang om de ruwheid van de lagen tijdens de depositie te beheersen, omdat ruwe grensvlakken tussen de lagen van de multilaag spiegel equivalent zijn aan dikke grenslagen. De opbouw van ruwheid wordt in de regel tegengegaan door middel van ionen bombardement van de Si lagen. Om inzicht te verkrijgen in dit proces, hetgeen kan leiden tot het vermogen scherpere grensvlakken te realiseren, is de ruwheidsevolutie van Si oppervlakken tijdens Ar^+ ionenerosie in real-time bestudeerd. Het is aangetoond dat een behandeling met ionen zowel tot vervlakking als tot verruwing kan leiden, afhankelijk van de aanvankelijke ruwheid van het substraat. De resultaten zijn verklaard aan de hand van een literatuurmodel. Tevens zijn de waarden bepaald van de zogenaamde schalingsexponenten, die van belang zijn voor de constructie van een universeel model voor ionenerosie.

Acknowledgments

None of the work presented in this thesis would have been possible without the help of the many kind and knowledgeable people that I met during the four years of my Ph.D. research. First of all, I am thankful to Fred for giving me the opportunity to conduct this research in such a nice group and allowing me a large degree of freedom. You were the one who would point out how nice my results were when I was lost in worries about all the small details. To Andrey I am very grateful for the great supervision and for always making time for me. Thanks for always taking the effort to explain to me why things would be better when done differently, and never ending the open-minded discussions before we were both happy with the outcome. Your sharp mind often discovered hidden information in graphs, which was at times frustrating when I tried to wrap up a paper. But it also taught me the important lesson to stay critical and it stimulated me to keep looking for indications. Robbert, Erwin and Jan, I wish to thank you for the innumerable discussions and pieces of advice. As regular discussion partners, you have contributed enormously to shaping this thesis and my scientific education.

The many fruitful discussions with Aart, Rico, Eddie, Hidde, Igor, Luca, Eric Ziegler, Rodolfo Cuerno and Barend Thijsse have also been very important for all the work in this thesis, thank you very much. Of course, none of this work would have been possible without the assistance of our skillful technicians. Kees deserves special thanks for his extended work on Cocoon, while the ADC's cryogenic substrate holder would have been a fiasco without Machiel's and Frenk's dedication or the great support from the workshop and the design department. I wish to thank Hans and Johan for their hospitality and enthusiastic support at Amolf. Pim, it was a pleasure to work with you and I thank you for your valuable contributions and your help with the acquisition, processing and interpretation of the huge amount of data that led to Chapter 5.

I want to thank Saskia for measuring virtually all the Cu K_{α} spectra for me, but most of all for being such a good friend. It was great to have somebody else in the group who refers to a car by its color and size and not by its brand and type. Jeroen, too, is a true friend, with whom I could share all the good and bad times, lengthy discussions about physics, and tips about good food.

Raoul has always been a big support for me in everything, and my Ph.D. work was no exception. He did not complain one single time that I was absent for yet another week when I had synchrotron beam-time or a nice conference abroad, nor when I was at home, but with my attention devoted to the completion of this thesis. My parents deserve a very special ‘thank you’ as well. You have encouraged my ambitions, first to enroll in university and later to take on a Ph.D. position, even though you knew that this would only increase the chances of emigration.

Last but not least, I am grateful to all the nSI members for the gezellige lunch- and coffeebreaks and for making the past four years such a memorable time. I really enjoyed doing my Ph.D. research at Rijnhuizen.

Curriculum Vitae

Véronique de Rooij-Lohmann was born on the 28th of July, 1982 in Beuningen, The Netherlands. She started the secondary school *Dominicus College* in Nijmegen in September 1994. In June 2000, she graduated with an average mark of 8.5 and four extra subjects. She started studying Applied Physics at the Eindhoven University of Technology in September 2000. As an undergraduate student, she investigated chiral liquid crystals and their use in displays that use selective reflection of ambient light rather than backlighting. Véronique obtained her B.Sc. degree cum laude in December 2003. As a graduate student, she spent three months at the National University of Singapore, studying the possibilities to use lithography and proton beam writing to make micrometer-sized lenses with a gradually changing focal distance along one of the optical axes. The Master's thesis project was carried out at the Equilibrium and Transport in Plasmas group of the Eindhoven University of Technology, under supervision of dr. Mariadriana Creatore and prof. dr. ir. Richard van de Sanden. The topic of the project was interphase formation between polymer substrates and SiO₂-like films deposited by means of an expanding thermal plasma. It included a two-month stay at the Interfacial Technology and Material Science group of the Fraunhofer Institute for Interfacial Engineering and Biotechnology in Stuttgart, and led to her Master of Science degree in April 2006. From June 2006 to 2010, she worked as a PhD student at the FOM Institute for Plasma Physics Rijnhuizen, The Netherlands, on the topic of interface analysis and control in Mo/Si multilayer systems. The results of this research are presented in this thesis.

Bibliography

- [1] E. Spiller, *Soft X-Ray Optics* (SPIE, Bellingham, 1994).
- [2] D. G. Stearns, R. S. Rosen, and S. P. Vernon, *Journal of Vacuum Science & Technology A: Vacuum, Surfaces, and Films* **9**, 2662 (1991).
- [3] S. Bajt, J. B. Alameda, T. W. Barbee, W. M. Clift, J. A. Folta, B. Kaufmann, and E. A. Spiller, *Optical Engineering* **41**, 1797 (2002).
- [4] T. Feigl, S. Yulin, N. Kaiser, and R. Thielsch, *Emerging Lithographic Technologies IV* (SPIE, Santa Clara, 2000), **3997**, pp. 420.
- [5] F. Schäfers, *Physica B: Condensed Matter* **283**, 119 (2000).
- [6] E. A. Spiller, *Optical Engineering* **29**, 609 (1990).
- [7] D. Attwood, *Soft X-Rays and Extreme Ultraviolet Radiation. Principles and Applications* (Cambridge University Press, Cambridge, 1999).
- [8] S. Yulin, in *Optical Interference Coatings*, edited by N. Kaiser and H. K. Pulker (Springer, Berlin Heidelberg, 2003), pp. 281.
- [9] N. Kaiser, *Photonik* **6**, 50 (2006).
- [10] J. Kirz, C. Jacobsen, and M. Howells, *Quarterly Reviews of Biophysics* **28**, 33 (1995).
- [11] J. F. Seely, *X-Ray Optics, Instruments, and Missions IV* (SPIE, San Diego, 2000), **4138**, pp. 174.
- [12] R. F. Pease, *Emerging Lithographic Technologies IX* (SPIE, San Jose, CA, USA, 2005), **5751**, pp. 15.
- [13] P. J. Silverman, *Journal of Microlithography, Microfabrication, and Microsystems* **4**, 011006 (2005).
- [14] I. Ugarte-Urra, <http://msslxr.mssl.ucl.ac.uk:8080/SolarB/eisgallery.jsp>, (2009).
- [15] S. Bajt, D. G. Stearns, and P. A. Kearney, *Journal of Applied Physics* **90**, 1017 (2001).
- [16] J. M. Slaughter, A. Shapiro, P. A. Kearney, and C. M. Falco, *Physical Review B* **44**, 3854 (1991).
- [17] I. Nedelcu, R. W. E. van de Kruijs, A. E. Yakshin, and F. Bijkerk, *Physical Review B* **76** (2007).
- [18] P. Reinig, F. Fenske, W. Fuhs, A. Schöpke, and B. Selle, *Applied Surface Science* **210**, 301 (2003).
- [19] R. S. Rosen, D. G. Stearns, M. A. Viliardos, M. E. Kassner, S. P. Vernon, and Y. D. Cheng, *Applied Optics* **32**, 6975 (1993).
- [20] S. Yulin, T. Feigl, T. Kuhlmann, N. Kaiser, A. I. Fedorenko, V. V. Kondratenko, O. V. Poltseva, V. A. Sevryukova, A. Y. Zolotaryov, and E. N. Zubarev, *Journal of Applied Physics* **92**, 1216 (2002).
- [21] E. Schubert, S. Mändl, H. Neumann, and B. Rauschenbach, *Applied Physics A: Materials Science & Processing* **80**, 47 (2005).

- [22] S. Bruijn, R. W. E. van de Kruijs, A. E. Yakshin, and F. Bijkerk, Defect and Diffusion Forum **Diffusion in Solids and Liquids IV**, 283 (2009).
- [23] T. Böttger, D. C. Meyer, P. Paufler, S. Braun, M. Moss, H. Mai, and E. Beyer, Thin Solid Films **444**, 165 (2003).
- [24] A. E. Yakshin, R. W. E. van de Kruijs, E. Zoethout, I. Nedelcu, E. Louis, F. Bijkerk, H. Enkisch, and S. Muellender, Sematech International EUVL Symposium (Barcelona, 2006).
- [25] E. Spiller, Applied Physics Letters **54**, 2293 (1989).
- [26] E. Louis, H. J. Voorma, N. B. Koster, L. Shmaenok, F. Bijkerk, R. Schlatmann, J. Verhoeven, Y. Y. Platonov, G. E. van Dorssen, and H. A. Padmore, Microelectronic Engineering **23**, 215 (1994).
- [27] E. J. Puik, M. J. Van Der Wiel, J. Verhoeven, and H. Zeijlemaker, Thin Solid Films **193-194**, 782 (1990).
- [28] E. J. Puik, M. J. van der Wiel, H. Zeijlemaker, and J. Verhoeven, Applied Surface Science **47**, 251 (1991).
- [29] R. Schlatmann, C. Lu, J. Verhoeven, E. J. Puik, and M. J. van der Wiel, Applied Surface Science **78**, 147 (1994).
- [30] H. J. Voorma, E. Louis, N. B. Koster, F. Bijkerk, and E. Spiller, Journal of Applied Physics **81**, 6112 (1997).
- [31] S. P. Vernon, D. G. Stearns, and R. S. Rosen, Applied Optics **32**, 6969 (1993).
- [32] H. J. Voorma, E. Louis, F. Bijkerk, and S. Abdali, Journal of Applied Physics **82**, 1876 (1997).
- [33] J. M. Slaughter, D. W. Schulze, C. R. Hills, A. Mirone, R. Stalio, R. N. Watts, C. Tarrío, T. B. Lucatorto, M. Krumrey, P. Mueller, and C. M. Falco, Journal of Applied Physics **76**, 2144 (1994).
- [34] M. B. Stearns, C.-H. Chang, and D. G. Stearns, Journal of Applied Physics **71**, 187 (1992).
- [35] H. J. Voorma, E. Louis, N. B. Koster, and F. Bijkerk, Journal of Applied Physics **83**, 4700 (1998).
- [36] H. J. Voorma, G. E. van Dorssen, E. Louis, N. B. Koster, A. D. Smith, M. D. Roper, and F. Bijkerk, Applied Surface Science **93**, 221 (1996).
- [37] A. Klöidt, K. Nolting, U. Kleineberg, B. Schmiedeskamp, U. Heinzmann, P. Müller, and M. Kühne, Applied Physics Letters **58**, 2601 (1991).
- [38] M. Niibe, M. Hayashida, T. Iizuka, A. Miyake, Y. Watanabe, R. Takahashi, and Y. Fukuda, X-Ray/EUV Optics for Astronomy, Microscopy, Polarimetry, and Projection Lithography (SPIE, San Diego, CA, USA, 1991), **1343**, pp. 2.
- [39] S. Ogura, M. Niibe, Y. Watanabe, M. Hayashida, and T. Iizuka, X-Ray Multilayers for Diffractometers, Monochromators, and Spectrometers, edited by F. E. Christensen (SPIE, San Diego, CA, USA, 1988), **984**, pp. 140.
- [40] G. Sauerbrey, Zeitschrift für Physik A Hadrons and Nuclei **155**, 206 (1959).

- [41] E. Kretschmann, *Optics Communications* **5**, 331 (1972).
- [42] E. Kröger and E. Kretschmann, *Zeitschrift für Physik A Hadrons and Nuclei* **237**, 1 (1970).
- [43] D. L. Windt, *IMD version 4.1* (1998).
- [44] H. H. Brongersma, M. Draxler, M. de Ridder, and P. Bauer, *Surface Science Reports* **62**, 63 (2007).
- [45] H. Niehus, W. Heiland, and E. Taglauer, *Surface Science Reports* **17**, 213 (1993).
- [46] H. H. Brongersma and P. M. Mul, *Chemical Physics Letters* **14**, 380 (1972).
- [47] R. Cortenraad, S. N. Ermolov, B. Moest, A. W. Denier van der Gon, V. G. Glebovsky, and H. H. Brongersma, *Nuclear Instruments and Methods in Physics Research Section B: Beam Interactions with Materials and Atoms* **174**, 173 (2001).
- [48] D. P. Smith, *Surface Science* **25**, 171 (1971).
- [49] M. P. de Jong, D. P. L. Simons, M. A. Reijme, L. J. van IJzendoorn, A. W. Denier van der Gon, M. J. A. de Voigt, H. H. Brongersma, and R. W. Gymer, *Synthetic Metals* **110**, 1 (2000).
- [50] F. J. J. Janssen, A. W. Denier van der Gon, L. J. van IJzendoorn, R. Thoelen, M. J. A. de Voigt, and H. H. Brongersma, *Applied Surface Science* **241**, 335 (2005).
- [51] K. Kawamoto, T. Mori, S. Kujime, and K. Oura, *Surface Science* **363**, 156 (1996).
- [52] W. C. A. N. Ceelen, J.-P. Jacobs, H. H. Brongersma, E. G. F. Sengers, and F. J. J. G. Janssen, *Surface and Interface Analysis* **23**, 712 (1995).
- [53] G. C. Van Leerdam, P. A. J. Ackermans, P. A. C. Groenen, H. H. Brongersma, and J. E. J. Schmitz, *Nuclear Instruments and Methods in Physics Research Section B: Beam Interactions with Materials and Atoms* **35**, 500 (1988).
- [54] G. C. Van Leerdam, K. M. H. Lenssen, and H. H. Brongersma, *Nuclear Instruments and Methods in Physics Research Section B: Beam Interactions with Materials and Atoms* **45**, 390 (1990).
- [55] R. Souda, K. Yamamoto, W. Hayami, T. Aizawa, and Y. Ishizawa, *Surface Science* **363**, 139 (1996).
- [56] U. Gerlach-Meyer, J. W. Coburn, and E. Kay, *Surface Science* **103**, 177 (1981).
- [57] ICRU, Report No. 49, *Stopping powers and ranges for protons and alpha particles*, 1993.
- [58] J. Sillanpää, E. Vainonen-Ahlgren, P. Haussalo, and J. Keinonen, *Nuclear Instruments and Methods in Physics Research Section B: Beam Interactions with Materials and Atoms* **142**, 1 (1998).
- [59] M. E. Glicksman, *Diffusion in solids: field theory, solid-state principles, and applications* (John Wiley & Sons, New York, 2000).

- [60] M. Salamon and H. Mehrer, *Zeitschrift Für Metallkunde* **96**, 833 (2005).
- [61] J. Y. Cheng, H. C. Cheng, and L. J. Chen, *Journal of Applied Physics* **61**, 2218 (1987).
- [62] A. Guivarc'h, P. Auvray, L. Berthou, M. L. Cun, J. P. Boulet, P. Henoc, G. Pelous, and A. Martinez, *Journal of Applied Physics* **49**, 233 (1978).
- [63] K. Holloway, K. B. Do, and R. Sinclair, *Journal of Applied Physics* **65**, 474 (1989).
- [64] A. Dan'ko, I. Z. Indutnyi, V. S. Lysenko, I. Y. Maidanchuk, V. I. Min'ko, A. N. Nazarov, A. S. Tkachenko, and P. E. Shepelyavyi, *Semiconductors* **39**, 1197 (2005).
- [65] Y.-K. Sun, D. J. Bonser, and T. Engel, *Journal of Vacuum Science & Technology A* **10**, 2314 (1991).
- [66] S. Mirabella, D. De Salvador, E. Bruno, E. Napolitani, E. F. Pecora, S. Boninelli, and F. Priolo, *Physical Review Letters* **100**, 155901 (2008).
- [67] R. Winter and P. Heitjans, *Journal of Physical Chemistry B* **105**, 6108 (2001).
- [68] A. Lakatos, A. Csik, G. A. Langer, G. Erdelyi, G. L. Katona, L. Daroczi, K. Vad, J. Toth, and D. L. Beke, *Vacuum* **84**, 130 (2009).
- [69] S. P. Hau-Riege, H. N. Chapman, J. Krzywinski, R. Sobierajski, S. Bajt, R. A. London, M. Bergh, C. Caleman, R. Nietubyc, L. Juha, J. Kuba, E. Spiller, S. Baker, R. Bionta, K. S. Tinten, N. Stojanovic, B. Kjornrattanawanich, E. Gullikson, E. Plonjes, S. Toleikis, and T. Tschentscher, *Physical Review Letters* **98**, 145502 (2007).
- [70] V. I. T. A. de Rooij-Lohmann, A. W. Kleyn, F. Bijkerk, H. H. Brongersma, and A. E. Yakshin, *Applied Physics Letters* **94**, 063107 (2009).
- [71] C. M. Doland and R. J. Nemanich, *Journal of Materials Research* **5**, 2854 (1990).
- [72] G. J. A. Hellings, H. Ottevanger, S. W. Boelens, C. L. C. M. Knibbeler, and H. H. Brongersma, *Surface Science* **162**, 913 (1985).
- [73] T. Tsarfati, E. Zoethout, R. W. E. van de Kruijs, and F. Bijkerk, *Journal of Applied Physics* **105**, 104305 (2009).
- [74] M. Gorgoi, S. Svensson, F. Schäfers, G. Öhrwall, M. Mertin, P. Bressler, O. Karis, H. Siegbahn, A. Sandell, H. Rensmo, W. Doherty, C. Jung, W. Braun, and W. Eberhardt, *Nuclear Instruments and Methods in Physics Research Section A: Accelerators, Spectrometers, Detectors and Associated Equipment* **601**, 48 (2009).
- [75] F. Schaefer, M. Mertin, and M. Gorgoi, *Review of Scientific Instruments* **78**, 14 (2007).
- [76] W. A. Brainard and D. R. Wheeler, *Journal of Vacuum Science & Technology* **15** (1978).
- [77] W. Lisowski, E. G. Keim, and M. Smithers, *Applied Surface Science* **189**, 148 (2002).

- [78] I. Kaur, Y. Mishin, and M. Gust, *Fundamentals of Grain and Interphase Boundary Diffusion* (Wiley, Chichester, 1995), p. 528.
- [79] A. Patelli, J. Ravagnan, V. Rigato, G. Salmaso, D. Silvestrini, E. Bontempi, and L. E. Depero, *Applied Surface Science* **238**, 262 (2004).
- [80] I. Nedelcu, R. W. E. van de Kruijs, A. E. Yakshin, and F. Bijkerk, *Journal of Applied Physics* **103**, 083549 (2008).
- [81] P. J. Cumpson and M. P. Seah, *Surface and Interface Analysis* **25**, 430 (1997).
- [82] K. Hirose, I. Ohdomari, and M. Uda, *Physical Review B* **37**, 6929 (1988).
- [83] H. Nowotny, E. Dimakopoulou, and H. Kudielka, *Monatshefte für Chemie / Chemical Monthly* **88**, 180 (1957).
- [84] J. E. Saal, S. Shang, and Z.-K. Liu, *Applied Physics Letters* **91**, 231915 (2007).
- [85] F. R. de Boer, R. Boom, W. C. M. Mattens, A. R. Miedema, and A. K. Niessen, *Cohesion in metals. Transition metal alloys* (North-Holland, 1988).
- [86] H. M. Chen, H. Y. Qi, F. Zheng, L. B. Liu, and Z. P. Jin, *Journal of Alloys and Compounds* **481**, 182 (2009).
- [87] A. Costa e Silva and M. Kaufman, *Metallurgical and Materials Transactions A* **25**, 5 (1994).
- [88] H. Amrani, R. Hillel, F. Sibieude, R. Berjoan, and R. Verges, *Journal of Materials Science Letters* **13**, 1472 (1994).
- [89] W. J. Boettinger, J. H. Perepezko, and P. S. Frankwicz, *Materials Science and Engineering: A* **155**, 33 (1992).
- [90] P. Steinmetz, B. Roques, and R. Pichoir, *Journal of the Less-Common Metals* **48**, 225 (1976).
- [91] M. Timonova, B.-J. Lee, and B. J. Thijsse, *Nuclear Instruments and Methods in Physics Research Section B: Beam Interactions with Materials and Atoms* **255**, 195 (2007).
- [92] I. Nedelcu, R. W. E. van de Kruijs, A. E. Yakshin, and F. Bijkerk, *Applied Optics* **48**, 155 (2009).
- [93] I. Nedelcu, R. W. E. van de Kruijs, A. E. Yakshin, F. Tichelaar, E. Zoethout, E. Louis, H. Enkisch, S. Muellender, and F. Bijkerk, *Thin Solid Films* **515**, 434 (2006).
- [94] A. E. Yakshin, E. Louis, P. C. Görts, E. L. G. Maas, and F. Bijkerk, *Physica B: Condensed Matter* **283**, 143 (2000).
- [95] B. D. Cullity and S. R. Stock, *Elements of X-Ray Diffraction* (Prentice Hall, Upper Saddle River, NJ, 2001), p. 664.
- [96] A. K. Petford-Long, M. B. Stearns, C. H. Chang, S. R. Nutt, D. G. Stearns, N. M. Ceglio, and A. M. Hawryluk, *Journal of Applied Physics* **61**, 1422 (1987).
- [97] A. Ulyanekov, R. Matsuo, K. Omote, K. Inaba, J. Harada, M. Ishino, M. Nishii, and O. Yoda, *Journal of Applied Physics* **87**, 7255 (2000).

- [98] A. Schindler, T. Haensel, A. Nickel, H.-J. Thomas, H. Lammert, and F. Siewert, *Optical Manufacturing and Testing V* (SPIE, San Diego, CA, USA, 2004), **5180**, pp. 64.
- [99] F. Frost, R. Fechner, B. Ziberi, D. Flamm, and A. Schindler, *Thin Solid Films* **459**, 100 (2004).
- [100] J. Verhoeven, L. Chunguang, E. J. Puik, M. J. van der Wiel, and T. P. Huijgen, *Applied Surface Science* **55**, 97 (1992).
- [101] R. Cuerno, L. Vázquez, R. Gago, and M. Castro, *Journal of Physics: Condensed Matter* **21** (2009).
- [102] A.-L. Barabási and H. E. Stanley, *Fractal Concepts in Surface Growth* (Cambridge University Press, Cambridge, 1995), p. 388.
- [103] F. Family and T. Vicsek, *Journal of Physics A: Mathematical and General* **18**, L75 (1985).
- [104] L. Peverini, E. Ziegler, and I. Kozhevnikov, *Applied Physics Letters* **91**, 053121 (2007).
- [105] R. Cuerno and A.-L. Barabási, *Physical Review Letters* **74**, 4746 (1995).
- [106] R. Anton, T. Wiegner, W. Naumann, M. Liebmann, C. Klein, and C. Bradley, *The 8th international conference on ion sources* (AIP, Kyoto (Japan), 2000), **71**, pp. 1177.
- [107] V. E. Asadchikov, I. V. Kozhevnikov, Y. S. Krivonosov, R. Mercier, T. H. Metzger, C. Morawe, and E. Ziegler, *Nuclear Instruments and Methods in Physics Research Section A: Accelerators, Spectrometers, Detectors and Associated Equipment* **530**, 575 (2004).
- [108] L. Peverini, I. Kozhevnikov, and E. Ziegler, *Physica Status Solidi (a)* **204**, 2785 (2007).
- [109] C. S. Madi, B. Davidovitch, H. B. George, S. A. Norris, M. P. Brenner, and M. J. Aziz, *Physical Review Letters* **101**, 246102 (2008).
- [110] S. Majaniemi, T. Ala-Nissila, and J. Krug, *Physical Review B* **53**, 8071 (1996).
- [111] L. Peverini, E. Ziegler, T. Bigault, and I. Kozhevnikov, *Physical Review B (Condensed Matter and Materials Physics)* **76**, 045411 (2007).
- [112] I. Nedelcu, *Interface structure and interdiffusion in Mo/Si multilayers* (University of Twente, Ph.D. thesis (2007).
- [113] T. Tsarfati, *Surface and Interface Dynamics in Multilayered Structures* (University of Twente, Ph.D. thesis (2009).
- [114] T. Tsarfati, E. Zoethout, R. W. E. van de Kruijs, and F. Bijkerk, *Surface Science* **603**, 2594 (2009).
- [115] A. Delabie, R. L. Puurunen, B. Brijs, M. Caymax, T. Conard, B. Onsia, O. Richard, W. Vandervorst, C. Zhao, M. M. Heyns, M. Meuris, M. M. Viitanen, H. H. Brongersma, M. de Ridder, L. V. Goncharova, E. Garfunkel, T. Gustafsson, and W. Tsai, *Journal of Applied Physics* **97**, 064104 (2005).
- [116] M. Stokhof, H. Sprey, W.-M. Li, S. Haukka, M. de Ridder, and H. Brongersma, *ECS Transactions* **1**, 71 (2006).